CORA Cork Open Research Archive
Cartlann Taighde Oscailte Chorcaí

Title	Ab initio calculations of group 4 metallocene reaction mechanisms: atomic layer deposition and bond activation catalysis
Authors	Zydor, Aleksandra
Publication date	2013
Original Citation	Zydor, A. 2013. Ab initio calculations of group 4 metallocene reaction mechanisms: atomic layer deposition and bond activation catalysis. PhD Thesis, University College Cork.
Type of publication	Doctoral thesis
Rights	© 2013, Aleksandra Zydor. - http://creativecommons.org/licenses/by-nc-nd/3.0/
Download date	2026-10-30 18:19:18
Item downloaded from	https://hdl.handle.net/10468/1235



UCC
University College Cork, Ireland
Coláiste na hOllscoile Corcaigh

Ollscoil na hÉireann
NATIONAL UNIVERSITY OF IRELAND

Ab initio calculations of group 4 metallocene reaction mechanisms: atomic layer deposition and bond activation catalysis

By

Aleksandra Zydor, M.Sc.

A thesis submitted for degree of Doctor of Philosophy in Chemistry at
Tyndall National Institute, University College Cork, Ireland

Department Head: Prof. Michael Morris
Supervisor: Dr. Simon Elliott

January 2013





Table of Contents

Declaration		I
Acknowledgements		III
Dedication		V
Abstract		VII
Chapter 1. Introduction		**1**
1.1	Thin film Group 4 oxides for high-*k* dielectric materials	1
1.2	Atomic Layer Deposition	3
1.3	ALD Precursors	6
	1.3.1 Halides	7
	1.3.2 Alkyls	8
	1.3.3 Alkoxides	9
	1.3.4 β-Diketonates	10
	1.3.5 Alkylamides and Silylamides	11
	1.3.6 Amidinates	12
	1.3.7 Group 4 metallocenes	12
1.4	Group 4 Metallocene Complexes in Catalysis	14
1.5	Outline of the work	16
Chapter 2.	**Theoretical background**	**27**
2.1	Computational Chemistry: Density Functional Theory	27
	2.1.1 General electronic structure theory	27
	2.1.2 Hartree-Fock Theory	28
	2.1.3 Density Functional Theory	30
2.2	Tools used in this work	33
Chapter 3.	**An *ab initio* evaluation of cyclopentadienyl precursors for the atomic layer deposition of hafnia and zirconia**	**35**
3.1	Introduction	37
3.2	Method	38
3.3	Results	40
	3.3.1 Reactivity and ALD growth rate	41
	3.3.2 Dipole moment and volatility	45
3.4	Discussion	46
3.5	Conclusion	48
Chapter 4.	**Mechanism for zirconium oxide atomic layer deposition using Bis(methylcyclopentadienyl)methoxymethyl zirconium**	**51**
Chapter 5.	**First principles simulation of reaction steps in the atomic layer deposition of titania: dependence of growth on Lewis acidity of titanocene precursor**	**61**
5.1	Introduction	63
	5.1.1 Thin film deposition of titania	63
	5.1.2 ALD mechanism	65
5.2	Mass spectrometric experiment	67
	5.2.1 Method for mass spectrometry	67
	5.2.2 Experimental results from mass spectroscopy	68

5.3	First principles study of mechanism	69
	5.3.1 Computational method	69
	5.3.2 Results for ligand basicity and 'ligand exchange'	70
	5.3.3 Surface models of bare and hydrated titanium oxide	71
	5.3.4 Results for precursor adsorption onto hydrated surfaces	72
	5.3.5 Results for elimination of ligands and densification	77
5.4	Discussion	79
5.5	Conclusion	84
Chapter 6.	**The thermal stability of precursors for atomic layer deposition of TiO_2, ZrO_2 and HfO_2: an *ab initio* study of α-hydrogen abstraction in biscyclopentadienyl dimethyl complexes**	**89**
6.1	Introduction	91
6.2	Theoretical methods	94
6.3	Results	95
	6.3.1 Decomposition pathway	95
	6.3.2 Effect of the metal cation	98
	6.3.3 Effect of the spectator ligands	100
	6.3.4 Possible reaction of 'spectator' ligands	104
6.4	Discussion	105
6.5	Conclusion	109
Chapter 7.	**C-H bond activation by rotational electron pair exchange in metallocene complexes.**	**113**
7.1	Introduction	115
7.2	Computational Section	116
7.3	Results and Discussions	117
7.4	Conclusion	124
Chapter 8.	**Understanding NN cleavage and NCO formation catalyzed by group 4 metallocene complexes.**	**127**
8.1	Introduction	129
8.2	Computational Section	131
8.3	Results and Discussion	133
	8.3.1 Hafnium dimer complex prior to reaction with CO	133
	8.3.2 Approach of CO along N-N axis	136
	8.3.3 Reaction pathway for CO via metal cation	137
	8.3.4 Effect of spectator ligands	140
	8.3.5 Effect of the metal cation	141
8.4	Conclusions	142
Chapter 9.	**Overall discussion and conclusions**	**145**
9.1	ALD Reaction Mechanism	145
	9.1.1 Ligand elimination model	145
	9.1.2 Surface model	146
	9.1.3 α-hydrogen Abstraction	148
9.2	Conclusions	153

Declaration

I hereby declare that the work presented in this thesis is my own, original work and it has not been presented for any other degree, neither at University College Cork nor to any other institution.



Aleksandra Zydor

Acknowledgements

I would like to thirst thank Dr. Simon Elliott for being the best research supervisor I could ever wish for. Foremost, I would like to express my sincere gratitude for his continuous support of my Ph.D study, for his immense patience, motivation, great knowledge and professionalism. I thank him for always giving me great examples of how to be a good researcher, for all his teaching, careful discussion and valuable suggestions which helped me through all the time of research and writing of this thesis. Without his guidance and persistent help this dissertation would not have been possible. It was a great honor to be his Ph.D student.

I would also like to thank the rest of my thesis committee: Dr. Paul Galvin and Dr. David Otway for their valuable comments and discussions.

Many thanks to my collaborators: Dr. Suvi Haukka (ASM), Dr. Tom Blomberg (ASM), Dr. Simon Rushworth (formerly SAFC Hitech), Dr. Stephen Potts (TU Eindhoven), Dr. Erwin Kessels (TU Eindhoven), Dr. Jeffrey Elam (Argonne), Prof. Anthony Jones (University of Liverpool) and Dr. Katarzyna Przybylak (University of Liverpool) for stimulating discussions and valuable questions that motivated different parts of this work.

I would like to thank all the members of the Electronic Theory Group for their help and support of my work and for the good times we have had during my stay at Tyndall. Special thanks to Dr. Jakub Baran and Dr. Michael Nolan for help with the Turbomole and Vasp programs.

I would like to thank the Irish Centre for High-End Computing (ICHEC) and Tyndall National Institute for providing access to High-Performance Computing (HPC) resources.

Chciałabym podziekować całej mojej rodzinie, a w szczególności moim rodzicom, Joli i Jasiowi, za to, że to właśnie dzięki ich wsparciu i miłości mogłam osiągnąć tak wiele i że zawsze mogę na nich liczyć.

Last but not the least I would like to thank my husband, Dr. Brice Jamieson for immense help, support and motivation in writing this thesis, whose patience in listening my scientific reasoning initiated the best ideas of my work.

The work has been financially supported by the Sixth Framework Programme of the European Union under the REALISE project (NMP4-CT-2006-016172) and by Enterprise Ireland under Innovation Partnership 'Hi-kCaps' (IP/2009/0035), part of the Medea+ project 'MAXCAPS' (2T210).

This work is dedicated to my family

Abstract

Thin film dielectrics based on titanium, zirconium or hafnium oxides are being introduced to increase the permittivity of insulating layers in transistors for micro/nanoelectronics and memory devices. Atomic layer deposition (ALD) is the process of choice for fabricating these films, as it allows for high control of composition and thickness in thin, conformal films which can be deposited on substrates with high aspect-ratio features. These characteristic properties of the ALD method are due to the self-limiting growth mode which comes from alternating pulses of surface-saturating precursors separated by inert gas purging. The success of this method depends crucially on the chemical properties of the precursor molecules. A successful ALD precursor should be volatile, stable in the gas-phase, but reactive on the substrate and growing surface, leading to inert by-products.

In recent years, many different ALD precursors for metal oxides have been developed, but many of them suffer from low thermal stability. Much promise is shown by group 4 metal precursors that contain cyclopentadienyl (Cp = $C_5H_{5-x}R_x$) ligands. One of the main advantages of Cp precursors is their thermal stability.

In this work *ab initio* calculations were carried out at the level of density functional theory (DFT) on a range of heteroleptic metallocenes [$M(Cp)_{4-n}(L)_n$], M = Hf/Zr/Ti, L = Me and OMe, in order to find mechanistic reasons for their observed behaviour during ALD.

Based on optimized monomer structures, reactivity is analyzed with respect to ligand elimination. The order in which different ligands are eliminated during ALD follows their energetics which was in agreement with experimental measurements.

Titanocene-derived precursors, $TiCp^*(OMe)_3$, do not yield TiO_2 films in atomic layer deposition (ALD) with water, while $Ti(OMe)_4$ does. DFT was used to model the ALD reaction sequence and find the reason for the difference in growth behaviour. Both precursors adsorb initially via hydrogen-bonding. The simulations reveal that the Cp* ligand of $TiCp^*(OMe)_3$ lowers the Lewis acidity of the Ti centre and prevents its coordination to surface O (densification) during both of the ALD pulses. Blocking this step hindered further ALD reactions and for that reason no ALD growth is observed from $TiCp^*(OMe)_3$ and water.

The thermal stability in the gas phase of Ti, Zr and Hf precursors that contain cyclopentadienyl ligands was also considered. The reaction that was found using DFT is an intramolecular α-H transfer that produces an alkylidene complex. The analysis shows that thermal stabilities of complexes of the type $MCp_2(CH_3)_2$ increase down group 4 (M = Ti, Zr and Hf) due to an increase in the HOMO-LUMO band gap of the reactants, which itself increases with the electrophilicity of the metal.

The reverse reaction of α-hydrogen abstraction in $ZrCp_2Me_2$ is 1,2-addition reaction of a C-H bond to a Zr=C bond. The same mechanism is investigated to determine if it operates for 1,2 addition of the ^{t}Bu C-H across Hf=N in a corresponding Hf dimer complex. The aim of this work is to understand orbital interactions, how bonds break and how new bonds form, and in what state hydrogen is transferred during the reaction. Calculations reveal two synchronous and concerted electron transfers within a four-membered cyclic transition state in the plane between the cyclopentadienyl rings, one π(M=X)-to-σ(M-C) involving metal *d* orbitals and the other σ(C-H)-to-σ(X-H) mediating the transfer of neutral H, where X = C or N.

The reaction of the hafnium dimer complex with CO that was studied for the purpose of understanding C-H bond activation has another interesting application, namely the cleavage of an N-N bond and resulting N-C bond formation. Analysis of the orbital plots reveals repulsion between the occupied orbitals on CO and the N-N unit where CO approaches along the N-N axis. The repulsions along the N-N axis are minimized by instead forming an asymmetrical intermediate in which CO first coordinates to one Hf and then to N. This breaks the symmetry of the N-N unit and the resultant mixing of MOs allows σ(NN) to be polarized, localizing electrons on the more distant N. This allowed σ(CO) and π(CO) donation to N and back-donation of $\pi^*(Hf_2N_2)$ to CO.

Improved understanding of the chemistry of metal complexes can be gained from atomic-scale modelling and this provides valuable information for the design of new ALD precursors. The information gained from the model decomposition pathway can be additionally used to understand the chemistry of molecules in the ALD process as well as in catalytic systems.

Chapter 1. Introduction

1.1 Thin film Group 4 oxides for high-*k* dielectric materials

High-dielectric constant (high-*k*) materials are valuable for a wide range of applications such as Dynamic Random Access Memory (DRAM) capacitors, decoupling filter capacitors for integrated micro-power, and power capacitors for switched-capacitor power conversion. Their most vital application, however, could be in advanced logic devices where they are used as insulation between the transistor gate and channel. Moore's Law, which predicts that transistor density will double every two years, is used as a guideline for development in the semiconductor industry. To keep up with this rate, the length of transistor gates has had to decrease substantially. The ITRS roadmap for semiconductors 2011 [1] predicts that by 2020 transistor gate lengths will approach 10 nm, a full order of magnitude smaller than gate lengths 17 years ago and less than half the gate length of the present date. Such a reduction in sizes has been in a large part possible through the use of novel materials, including high-*k* dielectrics. If the trend is to continue, however, higher-*k* insulators will be required and they will need to be deposited not on flat substrates, but uniformly on highly-complex structures such as deep trenches, rough pedestals, and around three-dimensional objects such as the recently-commercialized FINFET transistor architecture, shown below in Figure 1.

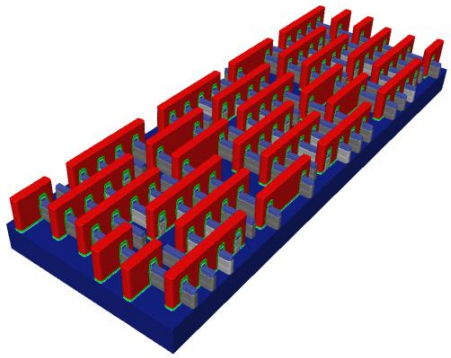


Figure 1 – Computer model of a FINFET-type structure, showing the Si substrate in blue, the source/drain running diagonally top-left to bottom-right in grey, the gate running diagonally top-right to bottom-left in red (on top of the source/drain), and the gate dielectric (the high-k material) shown in green, isolating the gate from the remainder [2].

As well as the requirements surrounding where and on what structures high-*k* dielectrics must be deposited, the continuing reduction in transistor current (also in the ITRS roadmap) additionally means that high-*k* dielectrics must have low leakage currents and remain stable during both processing and use. These materials must also be produced in a reliable, cost-effective process suitable for the 300 mm wafers used in modern semiconductor fabrication, into which any deposition method must be integrated.

Although silicon dioxide (SiO_2) has been almost universally used as gate dielectric, its dielectric constant ($k \approx 4$) is too small to give sufficient capacitance without excessive thinness. It has already been replaced by aluminum oxide ($k \approx 8$) in DRAM and tantalum oxide ($k \approx 20$) in decoupling capacitors. In 2007, SiO_2 was replaced as a gate dielectric in Intel's 45 nm process using hafnium-based high-*k* materials [3]. Furthermore, research is ongoing into future high-*k* dielectric materials such as hafnium aluminates, silicates, oxynitrides, nitrogen-containing silicates, and other classes of metal oxides based on zirconium ($k \approx 14$-25) [4], praseodymium, and lanthanum. ZrO_2, in particular, is of interest due to its large band gap (5-7.8 eV), [5, 6], thermodynamic stability on Si [7], and high permittivity [8, 9]. Titanium-based dielectrics such as TiO_2 are also under consideration due to their high dielectric constant, but suffer from a narrow band gap of 3.3 eV [10] leading to higher leakage currents (e.g. 10^{-5} A/cm² at 0.8 V [11]). Alkaline earth titanates such as $SrTiO_3$, however, are still considered promising candidate dielectrics, in particular for DRAM applications [4].

As mentioned earlier and regardless of the material used, any material deposition process must yield films that are uniform over large areas, contamination-free, thermally stable, and able to be deposited over complex nanostructures [12-15]. Above all, they must be cost-effective. As described in the next section, atomic layer deposition (ALD) is a processing technique that satisfies these criteria. Its ability to deposit very conformal films of uniform thickness has driven its use for depositing Al_2O_3 for trench capacitors in current DRAM production [16]. It is also used for highly-conformal dielectrics in magnetic read/write heads [17]. For the deposition of high-*k* gate dielectrics on MOSFETS, the suitability of ALD has led to its inclusion as a process in the ITRS roadmap and an important research topic [3, 18, 19].

1.2 Atomic Layer Deposition

Originally proposed in 1952 in the Ph.D. thesis of V. B. Aleksovskii and developed in the 1970s and 1980s [20, 21], Atomic Layer Deposition (ALD) is the leading technique for depositing thin, conformal films. ALD is used to deposit films of a variety of types, such as oxides, nitrides, metals, and sulfides. In particular and as mentioned in the previous section, ALD is a useful process for depositing high-k films [20]. ALD is a surface-controlled variant of Chemical Vapour Deposition (CVD) that separates the CVD reaction into two individual surface reactions, each due to the action of a separate precursor. Additionally, unlike a standard CVD reaction, the ALD reaction is self-limiting [13, 18, 22, 23]. An ALD reaction is carried out by exposing the surface to alternating pulses of different vapour-phase precursors, one at a time. Between each pulse, an inert gas is used to purge the deposition chamber, removing any volatile by-products produced in the precursor pulse and any unreacted precursors. The purge is for separating the precursors and keeping the ALD reaction from becoming a CVD reaction, thus minimising unwanted CVD deposition.

A typical ALD process involves two types of precursors. For example, in the case of ALD of a metal oxide like ZrO_2, one type of precursor contains the metal to be deposited, for example $ZrCp_2(OMe)Me$. The second precursor is a source of oxygen – H_2O as an example. During each pulse the precursor is chemisorbed onto the surface of the substrate until the surface is saturated with a monolayer of precursor fragments. After this, no further chemisorption takes place. This is possible because the reaction of the precursor with the surface is self-limiting and the amount of precursor adsorbed is limited by the active sites of the surface and by steric hidrance of the chemisorbed precursor molecules (ligands).

The growth of metal oxide layers by ALD consists then of repeating steps 2-5 of the following:

1. Initial surface before any ALD processing
2. First precursor pulse containing metal-precursor, continuing until the surface is saturated with with this precursor;
3. Purge of the reaction chamber with an inert gas to remove non-reacted precursor and any reaction by-products;

4. Second pulse containing oxygen-precursor, continuing until the surface is saturated (often with hydroxide);
5. Second purge of reaction chamber with inert gas to remove non-reacted precursor and by-products.

The full process is shown in the diagram in Figure 2 below, with the following stages proceeding from the top-left and in a clockwise direction:

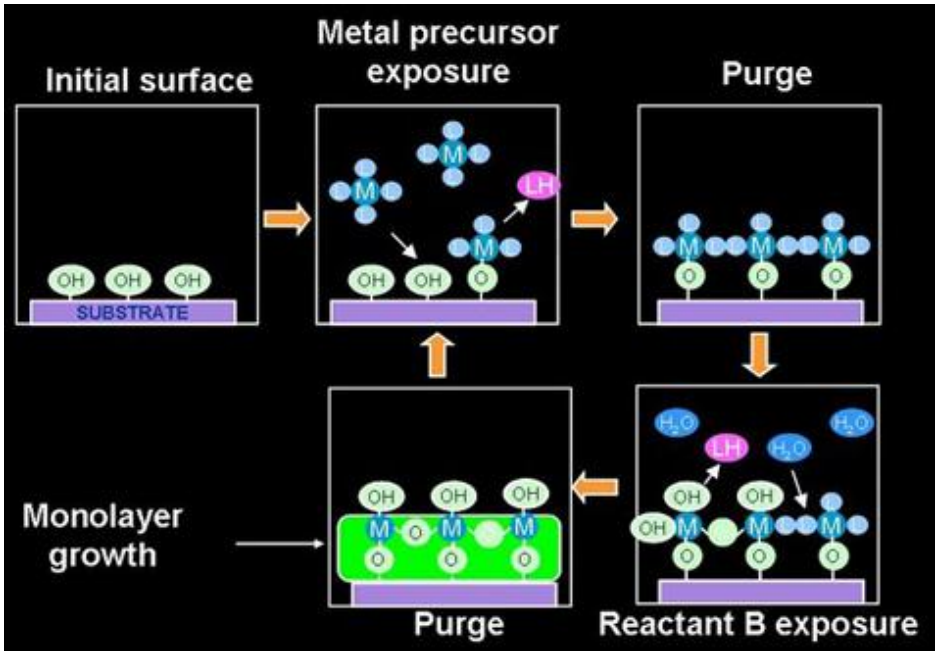


Figure 2 – The ALD process described in the series of major process steps [24]

Steps 2–5 describe a *reaction cycle*. Each reaction cycle adds a given amount of material to the surface, defined as the Growth Per Cycle (GPC). By repeating the reaction cycle a number of times the desired material thickness can be deposited by building up the structure layer by layer. The characteristics of the deposited film can additionally be controlled by adjusting the deposition conditions (temperature, pressure).

In contrast to the similar CVD process, films deposited using the ALD process are highly conformal and, because of the steady, predictable GPC which comes from depositing one layer at a time, the thickness and composition can be controlled down to the atomic level. Because of the self-limiting nature of the reaction, ALD can be used to deposit films on extremely complex surfaces, such as micropores and deep trenches, since the opening of the trench will not close before the full trench can be coated, as in the device in Figure 3 or Figure 1 in section 1.1. The main downside to ALD over a standard CVD process, however, is

that the predictable, layer-by-layer, self-limiting deposition is much slower than CVD: in ALD, GPC of 100 – 300 nm/hr are typical [25], while CVD GPC of up to 30 µm/hr [26] have been reported.

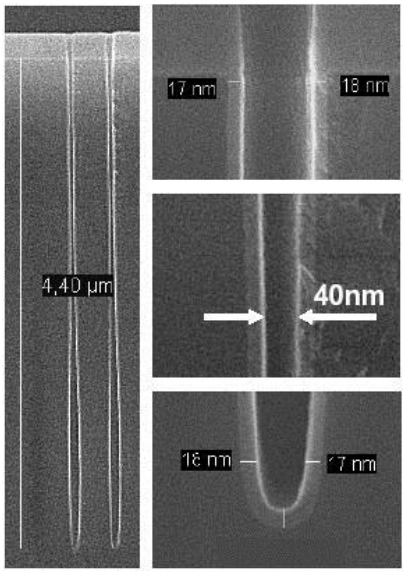


Figure 3 – A trench of aspect ratio AR~100 (4.40 µm deep, 40 nm wide) as required for the 90 nm ground rule in trench DRAM; the trench is evenly coated with 17-18 nm thick Al_2O_3 deposited by ALD. (image: Infineon Technologies)

In the case of depositing a high-*k* metal oxide using ALD, ligand exchange is one of many important reaction mechanisms in the ALD process [27]. In the common case where H_2O is used as an oxygen source, this ligand exchange occurs when the surface O-H bonds are broken in the presence of the metal-ligand (M-L) bonds of the precursor and the result is the formation of M-O and L-H bonds. In such a reaction, the thermodynamics are determined during the ALD reactions by the strengths of the bonds that dissociate and form. Additionally, to a lesser degree, these bond strengths will affect the reaction rates. As an example of this, a precursor having strong L-H and weak M-L bonds will react in a exothermic way. The product of such a reaction will be a pure, thin film that can be deposited at low temperatures, leading to smoother films than can be achieved with high deposition temperatures. Lower temperature additionally means fewer side reactions, which are typically undesirable in the ALD process as they may lead to impurities. On the other hand, a successful process does require the M-L bond to be sufficiently strong so that the precursor remains stable in the gas phase. As well, the selected precursors should be

chemically complementary, so that the reaction of one precursor with the previously-deposited fragment of the other precursor is exothermic. In this case, the ligands of the previous precursor are completely removed and the deposited film should be of high purity.

1.3 ALD Precursors

At the end of Section 1.2, the stability of the ALD precursor in the gas phase was identified as a key factor to the success of the reaction. This is, however, not the only factor that is important in a precursor and therefore it is valuable to fully define the properties which make up an ideal ALD precursor [13, 28, 29]. Stability in the gas phase, as previously mentioned, is necessary so that the precursor does not react with itself before it can be deposited on the surface and so that it does not produce unwanted gas-phase by-products. The precursor should, however, be volatile and vaporize readily at a known rate which can be easily reproduced. These two criteria are typically easily obtained for liquid precursors. It is more difficult to develop a solid precursor that fulfils the volatility and vaporization requirements. As well as being non-reactive in the gas-phase, an ideal precursor should be reactive on the substrate and growing surface so that a film can be deposited at a reasonable rate. The more reactive the precursor is on the surface, the faster the process may be carried out, as well as occurring at a lower temperature. Finally, an ideal precursor should produce inert by-products which can be easily removed from the deposition chamber in the gas purge phase. These by-products should especially be non-corrosive, as corrosive products will etch or corrode the film, leading to holes and other non-uniformities and, ultimately, a thin-film where the thickness can not be controlled to the high degree required of the ALD process. Finally, as mentioned in section 1.2, the precursors selected should be complementary and react with each other exothermically and at as low a temperature as possible, as this will result in pure, smooth, amorphous films that can not be produced if the temperature is higher and the reactions are less exothermic.

Of these properties, however, there are three properties which can be considered the most critical requirements of a good precursor and can be summarized as:

1. A precursor must be volatile either at room temperature or at elevated temperature
2. At the desired ALD processing temperature, a precursor must not undergo thermal decomposition
3. The gas-solid reactions of the reactants must fulfil the self-termination criterion.

Based on the properties outlined above, the most common Group 4 precursors for ALD may be identified based on how well they meet the listed ALD precursor requirements. We can identify two main precursor groups: metalinorganic (metal with inorganic ligands) and metal organic (metal with organic ligands). Metalinorganic precursors are those such as halides. Of the metal organic precursors there are further sub-groups which may be defined based on the presence of a metal-carbon bond. Precursors containing this bond include alkyls and cyclopentadienyls. Precursors without this bond include alkoxides, β-diketonates, amides, and amidinates.

There are several alkoxide, β-diketonate, alkylamide and other metal organic and metalinorganic precursors for ALD of titania, zirconia or hafnia. However some limitations for an optimal ALD process still need to be overcome. For example, low thermal stability of the precursor or increased impurity contents in the films may limit the applicability of certain processes. In the following sections we consider the precursors most typically used for ALD.

1.3.1 Halides

Metal halides, MCl_4, are the oldest class of ALD reactants, known since early experiments in the 1960s [30, 31]. They have been studied for the deposition of high-*k* dielectric oxides [6, 32] and they are available for many metals. A good example is $TiCl_4$, which is liquid at room temperature and is used as a precursor for TiO_2. The important advantage for ALD is that halides are typically highly reactive with the growth material and are thermally stable in the gas phase, which leads to good self-limiting ALD [33-37]. As an example, the $HfCl_4/H_2O$ ALD process has been used even at and above 800 °C [38].

However, the ALD process suffers from many other characteristics of metal halides. The Growth Per Cycle (GPC) obtained from halides is typically small. For the $HfCl_4/H_2O$ process at 300 °C, the GPC is about 0.05 nm, corresponding to only 15% of a monolayer [35, 39-41]. One other downside of halides is that many of them are solids. This requires increased ALD temperatures and can lead to the risk of particulate contamination of the substrate such as in the case of chlorine contamination of HfO_2. Such contamination will have adverse effects on the deposited film, it can etch the film constituents or the reactor material. As an example of the type of contamination observed, HfO_2 films grown at 300 °C from $HfCl_4/H_2O$ have been reported with approximately 0.3 at% Cl, 0.2 at% C, and 1.6 at% H [42]. $TiCl_4$ has also been shown to react unsuitably for ALD in a so-called agglomeration process [43-45],

which occurs above a certain threshold temperature. The exact nature and details of this process, however, remain unclear [45].

The high required temperature may additionally reduce the GPC due to the reduction of active OH surface sites. In the 300 °C $HfCl_4/H_2O$ process given as an example in the previous paragraph, the GPC is only approximately 0.05 nm – 15% of a monolayer [35, 39-41]. Finally, the gaseous reaction by-product of M-Cl halides with H_2O is HCl [46] which, among other unwanted side effects, is a corrosive gas that can etch the reactor material or film constituents [47, 48][49]. In addition, the gaseous reaction products re-absorb on the surface after their formation [50]. This, in combination with film etching, can lead to non-uniform film thicknesses [51].

Fluorides of Zr and Hf are not suitable for ALD because of their low volatilities and because the produced by-product HF is highly corrosive and dangerous. No significant advantages over chlorides are found with transition metal bromides and iodides.

1.3.2 Alkyls

Alkyls, $M(C_xH_y)_n$, were introduced as reactants in the mid-1980s [52-54] and have come to be well-known in ALD from such processes as the deposition of Al_2O_3 from the $Al(CH_3)_3$ precursor. These are highly-reactive, true organometallic compounds with small ligands, reducing the effects of steric hindrance, and a high GPC [41]. In the $AlMe_3/H_2O$ process, for example, the GPC is 0.9 Å at 300 °C [55-58] – 30 % of an Al_2O_3 monolayer. The gaseous reaction by-products of alkyls with hydrogen-containing non-metal reactants – H_2O – are typically inert, saturated hydrocarbons and as a result there is little re-adsorption or corrosion.

A major downside of alkyls, however, is their tendency to decompose at moderate temperature to metal hydrides and metal alkenes, as in the case of $AlMe_3$ which decomposes above 300 °C. [59] This may lead to carbon and hydrogen residues in the grown films, as in the example of Al_2O_3 which has been reported to contain approximately 0.2 at% carbon and 0.7 at% hydrogen when grown from $AlMe_3$ and H_2O at 300 °C [25]. This makes many alkyls unsuitable for ALD processes.

The thermal stability of alkyl precursors can be improved by introducing other ligands to form heteroleptic precursors such as $ZrCp_2Me_2$ [60], $HfCp_2Me_2$ [61], $Zr(MeCp)_2Me_2$ or $Hf(MeCp)_2Me(OMe)$ [62].

1.3.3 Alkoxides

The alkoxide group of metal organic precursors may be described as a metal precursor with alkoxo ligands bonded to the metal atom through one O atom, (M-(O-R)$_n$), such as hafnium tert-butoxide, Hf(O^{t}Bu)$_4$, or titanium tert-butoxide Ti(O^{t}Bu)$_4$. This group has been used as ALD reactants since the early 1990s [63-65] for relatively few element groups and almost exclusively for deposition of oxides. Although the popularity of alkoxides has decreased for the growth of binary oxides, they are used in combination with metal halide reactants for growing ternary oxides in a reaction demonstrated by Brei et al. [66] and popularized by Ritala et al. [67]. Since alkoxides already possess M-O bonds, they are relatively unaffected by ligand exchange reactions and high temperatures are required to break the M-alkoxide bond and form an M-O-surface bond. Possibly because of the difficulty in cleaving the M-O bond, there have been no reports of nitrides grown from alkoxides as in these precursors the M-O bond is stronger than the M-N bond. Alkoxo ligands must also be relatively bulky to achieve sufficient volatilities and low melting points because the M-O-R structure of the alkoxide does not screen the metal center from interacting with the oxygen atoms of precursors nearby. Many alkoxides are prone to thermal decomposition, leading to inhomogeneous thicknesses, reduced film density, and increased impurity content [68]. High concentrations of carbon and hydrogen impurities may be present, such as in the example of ZrO_2 films grown at 250°C through the Zr(O^{t}Bu)$_4$/H_2O process where 8 at% hydrogen and 2 at% carbon have been reported [69]. In addition, the gas-solid reactions of alkoxides will generate alcohols as by-products, which are reactive and may readsorb on the surface. This readsorption process reduces film growth [70, 71].

Also, precursors from the group of titanium alkoxides, e.g., Ti(O^{i}Pr)$_4$, are widely applied but again, thermal stability is limited and temperatures approaching 300 °C result in precursor decomposition [71, 72]. On the other hand, Ti(OMe)$_4$ has somewhat higher thermal stability than Ti(O^{i}Pr)$_4$ [72] and has been reported to give very promising results when applied together with Sr(^{t}Bu$_3$Cp)$_2$ and water to form high-*k* $SrTiO_3$ films on TiN at 250-300 °C [12]. However, solid Ti(OMe)$_4$ can increase the risk of particle incorporation, and thus liquid precursors are usually preferred.

1.3.4 β-Diketonates

β-diketonates are a class of metal precursors where the ligand chelates the metal center via two O atoms bonded to the metal, $M=(O_2C_3R_3)_n$, such as in $Zr(thd)_4$, (thd = 3,3,5,5-tetramethylheptane-3,5-dionate). These are common precursors for CVD and have been used since the late 1980s as ALD reactants for metal oxides. Their secondary use is for ALD of sulfides, fluorides, and metals. As with alkoxides, nitrides are not formed by β-diketonates, possibly due to the difficulty in replacing the M-O bond in the β–diketonate with an M-N bond. β-diketonates are typically solids and have low volatilities and slow vaporization kinetics.

To grow metal oxide from β-diketonates, rather than H_2O, a strong oxidizer is often used, such as O_3 [73, 74] or, at high temperatures with plasma, indicating a rather low reactivity of β-diketonates. Calculations also suggest that the low Brønsted basicity of the ligands means that surface-bound protons do not react with them [75]. Nevertheless, carbon contamination will be present which leads to increased leakage currents in deposited metal oxides. Carbonate films can also form due to the generation of CO_2 during the oxidation of the ligands rather than the desired oxides [76, 77]. Contamination from hydrogen is also present, as in the case of Y_2O_3 deposited from $Y(thd)_3/O_3$ at 300 °C where about 2 at% of both carbon and hydrogen was reported [78]. The bulky ligands in β-diketonates are an additional source of problems, causing steric hindrances [41, 79] and a GPC typically below 10% of a monolayer [80].

A recent report from Päiväsaari et al. [73] discussed the reactivity of lanthanide (Ln)-diketonates to grow lanthanide oxides, specifically in the $Ln(thd)_3/O_3$ reaction at a temperature of 300 °C. In this study, the thickness increment per ALD cycle was seen to increase systematically with increasing ionic radius of the lanthanides.

Group 4 diketonate precursors, although previously used in CVD processes [81], have not been widely adopted for ALD. Limited work has been done on this topic, such as in the case of zirconium oxide thin films deposited using $Zr(thd)_4$ as zirconium precursor and ozone as the oxygen source. [82] In this work, there was a low indicated GPC of 0.24 Å/cycle when processed at 370-400 °C.

1.3.5 Alkylamides and Silylamides

Another group of precursors includes alkylamides, nitrogen bonded to a metal ($M(NR_2)_n$) [83, 84], and silylamides, ($M(NSi_2R_6)_n$). These have been investigated as ALD reactants since the late 1990s [83-86] and represent a versatile group of reactants: they are available for a number of elements and can be used to form a wide range of materials including oxides, nitrides, and selenides.

Alkylamides have M-N bonds which are strong enough to keep them stable at their normal temperatures of use, but which are weak enough so that, combined with strong ligand elimination product N-H bonds, they may be used at a reduced ALD temperature. They are reactive with both water and ammonia, enabling oxide films to be grown with deliberate nitrogen incorporation and, further, metal nitrides to be grown without a plasma. The GPC using alkylamides, particularly of titanium, is greater than a monolayer [86, 87] – significantly higher than that of β-diketonates, halides, and alkoxides. The exact nature of this high GPC has been theorized to arise from re-adsorption [86, 88] however the effects of decomposition are also assumed to be a factor.

$Hf(NEtMe)_4$ and $Zr(NEtMe)_4$ (Et = ethyl, Me = methyl), known as TEMAH and TEMAZ, are commonly used as ALD as well as CVD precursors [84, 89-91]. An important advantage of these precursors is that they are liquid at the evaporation temperature and they have high vapor pressure [89, 91]. However, these metallorganic precursors have limited thermal stability and the final quality of the films they produce depends critically on such process parameters as the length and pressure of the pulses and the deposition temperature used [90, 92]. Such decomposition can increase the amount of C impurities in the deposited layer, which in turn affects the leakage throughout the gate stack [93].

In the case of $Ti(NMe_2)_4$ the decomposition temperature can be as low as 150 °C [94]. Because of this limited thermal stability the applicable deposition temperature of these precursors must be kept low. Even so, films deposited using alkylamides and silylamides frequently feature impurities. In the case of alkylamides, carbon and hydrogen impurities can be found, e.g. in TiN films grown through the $Ti(NEt_2)_4/NH_3$ process at 200 °C, carbon is found at approximately 4 at% and hydrogen is found at approximately 6 at%. In the case of silylamides, PrO_x films from the $Pr(N(SiMe_3)_2)_3/H_2O$ process at 250 °C contained about 3 at% carbon, 20 at% hydrogen, and 6 at% silicon [95]. The gaseous reaction by-products of the

ALD process with alkylamides and silylamides are not well characterized, with few investigations carried out on this topic.

1.3.6 Amidinates

One of the more recent classes of ALD reactants, amidinates were introduced in 2003 [96] and represent chemicals such as tetrakis(N,N'-dimethylacetamidinate)zirconium (Zr-AMD) [97], where each amidinate ligand chelates the metal center through two M-N bonds. They are available for most metals. Amidinate ligands are effective at preventing neighboring precursors from bonding to the metal center and oligomerising. As a result, amidinates have low melting points (liquid at room temperature) and high volatilities. They are thermally fairly stable realitive to amines, since the amidinato ligand chelates the metal center. Amidinate reactions seem to be self-terminating [96] up to decomposition temperatures around 300 °C [98]. Films deposited from amidinates may, however, contain residues of carbon, nitrogen, and hydrogen.

1.3.7 Group 4 metallocenes

The final group of ALD reactants considered, metallocenes are a particular type of organometallic reactants with a direct metal-carbon bond to a cyclopentadienyl ligand (Cp). This group was introduced to ALD in the early 1990s [99] but it was not until the 2000s that the group gained significant popularity, in part because they can be synthesized also for alkaline-earth metals. Like alkyls, the metal-carbon bond of cyclopentadienyls makes them reactive. As an example, reactions with H_2O can be used to grow oxides and using other co-reagents allows sulfides and elements to be grown as well.

Cyclopentadienyl precursors are especially popular in ALD of the group 4 oxides: TiO_2, ZrO_2 and HfO_2 [62, 100-102]. Increased thermal stability can be considered as a clear advantage for the Cp precursors. In the case of titanium Cp precursors, the thermal stability enhancement seems to be clear when compared to the pure alkylamides and alkoxides; e.g., changing one of these ligands to a Cp type ligand increases the thermal stability [101-103]. ALD with the heteroleptic alkylamido-cyclopentadienyl precursor $Ti(CpMe)(NMe_2)_3$ and ozone as oxygen source provides self-limiting ALD-type growth characteristics up to around 300 °C. A mixed alkoxide-cyclopentadienyl titanium compound has even higher thermal stability. The liquid precursor, $TiCp^*(OMe)_3$ (Cp^* = pentamethylcyclopentadienyl, $C_5(Me)_5$),

introduced by Blasco et al., [104] showed a very wide ALD process window with deposition temperatures up to 375-400 °C [104, 105]. This is in contrast with reactive titanium alkylamides such as $Ti(NMe)_4$ that suffers from self-decomposition at relatively low temperatures, which destroys the ALD-type growth mode [94].

ALD of high-quality ZrO_2 and HfO_2 films has been achieved from methyl metallocenes [62, 82, 106, 107]. These are heteroleptic complexes including methyl (Me = CH_3) and cyclopentadienyl (Cp = $C_5H_{5-n}R_n$) ligands [107]. When used in combination with H_2O or O_3, the Cp ligands give self-limiting growth [106] since fewer Cp ligands are eliminated during the $ZrCp_2Me_2$ pulse than Me ligands, resulting in a surface terminated with mostly Cp ligands [14]. These properties enable higher-density oxide films with fewer impurities and defects, [108] as well as improved step coverage of high aspect-ratio topologies. $ZrCp_2Me_2$ sublimed at < 150°C at 2-3 mbar, leaving residue on the order of a few percent, and when used in ALD with ozone it produced films at a GPC of 0.6 Å/cycle at 310-365°C [106, 109]. In the case of $HfCp_2Me_2$ and O_3 at 350°C, a slightly lower GPC was observed at 0.4 Å/cycle [61]. The main downside to these precursors, however, is that there are solids that can potentially generate particles on the surface of the growing films. Additionally, a higher GPC and wider range of deposition temperatures would be desirable.

Minor changes within the Cp ligand can increase thermal stability of the precursor. For example, by substituting cyclopentadienyl ligand with one methyl group can result with higher depostition temperature. Precursors such as $Hf(CpMe)_2(Me)_2$ and $Hf(CpMe)_2(Me)(OMe)$ have been used with O_3 and H_2O at 350-500 °C to give ALD at GPC of 0.5 and 0.4 Å/cycle respectively [62]. Additionally, an advantage of these precursors is that they are liquid under conditions suitable for the introduction of vapors to ALD systems (2-3 mbar, 60-65 °C). Modified forms of $ZrCp_2Me_2$ such as $Zr(MeCp)_2Me_2$ and $Zr(MeCp)_2(OMe)Me$ are liquid at evaporation temperature which helped reduce particle incorporation in the deposited films [62]. While minor changes in the Cp ligands thus give such thermal stability improvements, the exact reason for this is not yet clear.

The improvement on stabilty in $M(MeCp)_2Me_2$ or $M(MeCp)_2Me(OR)$ complexes (M = Zr, Hf) can be aslo achieved when replacing two unbridged cyclopentadienyl ligands with a bridged cyclopentadienyl ligand $(C_5H_4)_2CMe_2$ [110]. These complexes deposit oxide films at higher temperatures than unbridged metallocene complexes, enabling a reduction in impurities for higher-density oxide films.

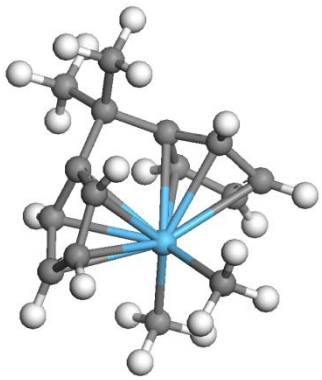


Figure 4 Ball and stick representations of computed structure of hf precursor that contains bridged cyclopentadienyl ligand $(C_5H_4)_2CMe_2$ and two methyl groups, white = hydrogen, grey = carbon, blue = Hf.

From the conclusions obtained in the literature it is clear that modifying the ligand configuration of ALD precursors allows significant effects such as enhanced thermal stability to be introduced into the ALD process for ZrO_2 and HfO_2 films [62]. The exact reason for the improvements, however, is still not entirely certain. For instance, it is unclear as to why certain types of precursors show growth in ALD while other precursors will not result in ALD growth, despite having the same metal centre and small variations in ligands. Additionally, the effect of different metal centres and ligands on the gas-phase stability is not well understood, [109, 111] even though it would be highly valuable to possess detailed knowledge of exactly what makes a Group 4 organometallic precursors more stable in the gas phase. Finally, despite some apparent similarities between the fields of ALD and catalysis, there is little knowledge of if and how the well-studied behaviours of catalytic reactions may apply to the ALD process. Very few links between these fields currently exist, even though it would be valuable to be able to apply knowledge from catalysis to ALD and vice versa. These listed points are some of the motivation for the work done in this thesis, which will be outlined in more detail in the following sections.

1.4 Group 4 Metallocene Complexes in Catalysis

Transition metal complexes are not restricted only to their applications for ALD. Transition metal complexes are also widely used across inorganic chemistry, organic synthesis, and catalysis. Transition metal complexes are used industrially in hydrogenation and hydroformylation, as well as in synthetic transformations including various metathesis processes, polymerization, and Wittig-type reactions [112-116].

Organometallics in Group 4 have been a subject of interest in the catalysis of polymerisation since the discovery of ferrocene, $Fe(C_5H_5)_2$, in the 1950s [117] with complexes of the type $TiCp_2Cl_2$ additionally prepared in the same decade. The stability of these cyclopentadienyls is one factor that made them attractive as catalysts. These compounds assisted in developing an understanding of the mechanism of how Ziegler-Natta catalysts operate, and titanium compounds mixed with alkylaluminum derivatives were discovered to accelerate the polymerisation of olefins [118, 119]. Cyclopentadienyl titanium and zirconium halides were additionally synthesized early on by Wilkinson et al. [120] and are currently one of the dominant ligand types. Importantly, the design of group 4 metallocenes as precursors for ALD processes is similar to the design of catalysts, in that the reactivity of the precursor can be tuned by the selection of the ligands and metal. In olefin polymerisation, by choosing the appropriate ligands, molecular weight, activity, co-monomer incorporation, and stereospecifity may all be manipulated [121]. The understanding of these ligand effects has been crucial to developing metallocene technology, as rational ligand design is possible at the transition metal centre. Features of catalytic behaviour, stability, and reactivity of metallocene complexes can be introduced even by the change or addition of one substituent [121]. Thus, the proper design of metallocene complexes can be crucial in producing polymers in a directed manner, containing the desired physical properties, by directing the catalytic reaction.

The instability of transition metal alkyl and aryl derivatives is due to facile decomposition by low activation energy pathways such as α and β-hydrogen elimination or abstraction, homolysis, or coupling of ligands at the transition metal atom. There are many examples of these reactions in the chemistry of titanium, zirconium and hafnium [122]. At the same time the reverse reaction of α-hydrogen abstraction is C-H bond activation.

The activation and functionalization of C‑H bonds is an active field of current chemical research, motivated by the desire to make more effective use of cheap and abundant simple hydrocarbons when converting them into valuable functionalized organic compounds such as alcohols, aldehydes, or carboxylic acids, as well as other compounds. Developing efficient strategies for the conversion of, for example, methane to methanol could significantly improve the utilization of this natural gas as its exploitation is limited by the high cost of gas transportation and current methods for converting the gas into a transportable liquid [123, 124]. Furthermore, the need for the methanol itself is highly driven by its global demand: approximately 45.6 million metric tons in 2010 [125].

Homogenous catalysis mediated by transition metal complexes is one of the most efficient ways to break the C-H bond. The σ(C–H) bond activation reaction involving group 4 transition metals is also an important topic in understanding the nature of metal coordination in the context of the alkene metathesis [126]. Similarly to the advent of the use of computational analysis for ALD, Andrews, Cho, et al. [127-129] have performed a combined DFT and experimental study of the reaction between an early transition metal and methane. By using the knowledge in the understanding of this reaction in catalysis, it may lead to better understanding of the same reaction in gas-phase decomposition.

One recent advance also shows the possibility of cleavage of the strong N-N bond within the coordination sphere of transition metal complexes of group 4 containing Cp type ligands with the addition of CO. The reaction leads not only to the breaking of the N-N bond but also to the formation of an N-C bond. The bond breaking reaction is desirable by industry as a potential replacement to the traditional but energy intensive Haber-Bosch process [130]. This process provides the world every year with 500 million tons of nitrogen fertilizer, a product responsible for sustaining one-third of the Earth's population, however with adverse effects to the environment [131].

1.5 Outline of the work

The work presented in this thesis looks at the role of group 4 metallocene molecules as precursors for ALD and, using computational modelling methods, attempts to better describe the mechanisms observed in their use as well as to better understand the underlying reaction dynamics. It seeks to improve understanding of why precursors of this type behave in the way they do, and to identify the reasons why precursors based on Ti, Hf, and Zr may behave very differently for the same reaction.

In Chapter Two, the methods and tools used in the work are identified and outlined in order to lay a clear framework for the work performed in the following chapters. Density Functional Theory (DFT) is described and its use in *ab initio* calculations of ALD precursor reaction mechanism is discussed. The computational tools that have been used are presented.

In Chapter Three, computational *ab initio* methods are used to analyze the reactivity of Hf and Zr precursors containing cyclopentadienyl ligands, with respect to ligand elimination. The reactions of precursors with water are computed as a model of ligand elimination along with their energetics. The energetics of this reaction are described as is their possible

influence on the ligand elimination process during ALD. The reactivity of these Cp-based precursors is then compared to that of amines and halides. The utility of computed dipole moments in predicting precursor volatility is discussed.

In Chapter Four, the model of ligand elimination developed in Chapter Three is applied to a real ALD system: the deposition of ZrO_2 from bis(methylcyclopentadienyl)methoxymethyl zirconium [$Zr(MeCp)_2(Me)(OMe)$] and H_2O. The *ab initio* calculations are used to predict the order in which ligands were lost. As a validation of the calculations, they are compared to mass spectroscopy measurements performed on films deposited experimentally. The reactivity predicted by the calculations is discussed with respect to the experimental results.

Experiments show that the titanocene-derived precursor TiCp*(OMe) does not yield TiO_2 films in atomic layer deposition (ALD) with water, while in the case of Ti-complexes such as $Ti(OMe)_4$ there is ALD growth. Models and calculations developed in the previous chapters predict that a titanocene-derived precursor should be more reactive in the ALD process than a monomeric alkoxide complex. In Chapter Five, a more realistic model describing the ALD reaction sequence is used to explain the different behaviours of titanium complexes, yielding new insights into the requirements for successful ALD.

In Chapter Six, the *ab initio* methods are used to analyze a different aspect of ALD deposition: the gas-phase thermal stability of precursors. DFT calculations are used to understand why, during experiments performed by partners in the project, violent decomposition was observed for $Zr(MeCp)_2Me_2$ precursors while no such decomposition was observed for $Hf(MeCp)_2Me_2$ and $Hf(MeCp)_2(OMe)$. To understand this, possible decomposition reactions are studied for Ti, Zr, and Hf precursors containing Cp ligands. DFT is used to identify the non-ALD reaction pathway and explain the surprising difference in chemistry of Zr and Hf complexes.

Chapter Seven deviates from the direct analysis of ALD and instead takes the calculations of the reaction pathway from Chapter Six and applies them to the study of C-H bond activation in a catalytic system. This is done because the previously-computed reaction is the reverse of a well-known type of C-H bond activation reaction used in catalysis. By applying the *ab initio* calculations of ALD to the analysis of this catalytic reaction, it is hoped that the knowledge gained from previous work will help to understand better the catalytic system of C-H bond activation reaction. Vice versa, the studies of catalysis in Chapter Seven may be applied to better understand the role of Group 4 metallocene precursors in ALD. Thus, in Chapter Seven, orbital interactions are analysed to understand electron transfer in the C-H

bond activation reaction, particularly how bonds break and form and how hydrogen is transferred in the reaction.

Having established this link between the chemistry of metal complexes in ALD and in catalysis, we continue the study of Group 4 metallocenes in catalysis. Chapter Eight looks at the N-N bond activation reaction and functionalization to N-C as a result of the reaction of a hafnium dimer metallocene complex with CO. From the previous theoretical study we know that the reaction happens via the coordination of CO to the metal centre. Chapter 8 addresses the question of why CO coordinates to the metal centre and why it cannot react directly with N along the N-N axis to immediately form NCO. Both reaction pathways are computed and the effect of orbital interactions is considered to reveal the various energetic barriers along different reaction pathways which give an understanding of the reaction mechanisms of N-N bond cleavage and NCO bond formation. We suggest that studies of catalytic systems, as in Chapter Seven and Chapter Eight, not only give a better understanding of the reaction mechanisms but also can provide valuable information and ideas on the subject of the precursor reactions in ALD, which may lead to the understanding and development of possible catalysts for ALD.

Chapter Nine finally summarizes the conclusions presented in the course of this thesis. The effect of Group 4 metallocenes on the ALD process is considered, and the results of the studies carried out are discussed in terms of their application to future ALD studies, both experimental and computational [130].

Figures, tables and references are numbered separately in each chapter.

1. ITRS. *Executive Summary: ITRS Roadmap 2011*. ITRS Roadmap 2011; Available from: http://www.itrs.net/Links/2011ITRS/2011Chapters/2011ExecSum.pdf.
2. Coventor. *Intel Announces Production-Ready 22 nm 3D Tri-gate Transistor*. Available from: http://info.coventor.com/semulator3d-news/bid/63583/Intel-Announces-Production-Ready-22nm-3-D-Tri-Gate-Transistor.
3. Bohr, M.T., et al., *The High-k Solution.* Spectrum, IEEE, 2007. **44**(10): p. 29-35.
4. Rose, M., et al., *Atomic Layer Deposition of Titanium Dioxide Thin Films from Cp*Ti(OMe)$_3$ and Ozone.* The Journal of Physical Chemistry C, 2009. **113**(52): p. 21825-21830.
5. Houssa, M., ed. *In High-k Gate Dielectrics*. Series in Materials Science and Engineering 2004, Institute of Physics Publishing: Bristol and Philadelphia.
6. Wilk, G.D., R.M. Wallace, and J.M. Anthony, *High-kappa gate dielectrics: Current status and materials properties considerations.* Journal of Applied Physics, 2001. **89**(10): p. 5243-5275.
7. Hubbard, K.J. and D.G. Schloma, *Thermodynamic Stability of Binary Oxides in Contact with Silicon.* MRS Online Proceedings Library, 1995. **401**: p. 33.
8. Thompson, D.P., A.M. Dickins, and J.S. Thorp, *The dielectric properties of zirconia.* Journal of Materials Science, 1992. **27**(8): p. 2267-2271.
9. Maiti, C.K., et al., *Electrical properties of high permittivity ZrO_2 gate dielectrics on strained-Si.* Solid-State Electronics, 2004. **48**(12): p. 2235-2241.
10. Kim, S.K., et al., *High dielectric constant TiO_2 thin films on a Ru electrode grown at 250 °C by atomic-layer deposition.* Applied Physics Letters, 2004. **85**(18): p. 4112-4114.
11. Kim, S.K., et al., *Al-Doped TiO_2 Films with Ultralow Leakage Currents for Next Generation DRAM Capacitors.* Advanced Materials, 2008. **20**(8): p. 1429-1435.
12. Jones, A.C. and L. Hitchman, *Chemical vapour deposition: precursors, processes and applications*. 2009: Royal Society of chemistry
13. Leskelä, M. and M. Ritala, *Atomic Layer Deposition Chemistry: Recent Developments and Future Challenges.* Angewandte Chemie International Edition, 2003. **42**(45): p. 5548-5554.
14. Ritala, M. and M. Leskela¨, in Handbook of Thin Film Materials, ed. H. S. Nalwa, Academic Press, San Diego, 2002, vol. 1, pp. 103-159.
15. Niinistö, L., M. Ritala, and M. Leskelä, *Synthesis of oxide thin films and overlayers by atomic layer epitaxy for advanced applications.* Materials Science and Engineering: B, 1996. **41**(1): p. 23-29.
16. Sneh, O., et al., *Thin film atomic layer deposition equipment for semiconductor processing.* Thin Solid Films, 2002. **402**(1): p. 248-261.
17. Paranjpe, A., et al., *Atomic Layer Deposition of AlOx for Thin Film Head Gap Applications.* Journal of The Electrochemical Society, 2001. **148**(9): p. G465-G471.
18. George, S.M., *Atomic Layer Deposition: An Overview.* Chemical Reviews, 2009. **110**(1): p. 111-131.
19. Fourmun, L., et al. *Atomic Layer Deposition: An Enabling Technology for Microelectronic Device Manufacturing*. in *Advanced Semiconductor Manufacturing Conference, 2007. ASMC 2007. IEEE/SEMI* 2007. p. 359-365.
20. Suntola, T., *Atomic layer epitaxy.* Materials Science Reports, 1989. **4**(5): p. 261-312.
21. Aleskovskii, V.B., *Chemistry and technology of solids.* Journal of Applied Chemistry of the Ussr, 1974. **47**(10): p. 2207-2217.
22. Leskelä, M. and M. Ritala, *Atomic layer deposition (ALD): from precursors to thin film structures.* Thin Solid Films, 2002. **409**(1): p. 138-146.
23. George, S.M., A.W. Ott, and J.W. Klaus, *Surface Chemistry for Atomic Layer Growth.* The Journal of Physical Chemistry, 1996. **100**(31): p. 13121-13131.

24. Henn-Lecordier, L. *University of Maryland*. Available from: http://web.archive.org/web/20100608050455/http://www.isr.umd.edu/~hennlec/research.html.
25. Matero, R., *Ph.D. Thesis: Atomic Layer Deposition of Oxide Films – Growth, Characterisation and Reaction Mechanism Studies* in *Department of Chemistry*. 2004, University of Helsinki: Helsinki.
26. Eid, J. and I.G. Galben. *3C-SiC growth on Si substrates via CVD: An introduction* Physics of Advanced Materials Winter School 2008; Available from: http://www.mansic.eu/documents/PAM1/Saddow.pdf
27. Cross, J.B. and H.B. Schlegel, *Molecular Orbital Studies of Titanium Nitride Chemical Vapor Deposition: Gas Phase Complex Formation, Ligand Exchange, and Elimination Reactions.* Chemistry of Materials, 2000. **12**(8): p. 2466-2474.
28. Ritala, M. and J. Niinisto¨, Chemical Vapour Deposition: Precursors and Processes; Royal Society of Chemistry: Cambridge, U.K., 2009: p. 158-206.
29. Musgrave, C.B. and R.G. Gordon. *Precursors For Atomic Layer Deposition Of High-k Dielectrics*. Process gases, chemicals and materials; Available from: http://www-chem.harvard.edu/groups/gordon/papers/Precursors_for_ALD.pdf.
30. Shevjakov, A.M., G.N. Kuznetsova, and V.B. Aleskovskii, *in Chemistry of High-Temperature Materials, Proceedings of the Second USSR Conference on High-Temperature Chemistry of Oxides, Leningrad, USSR, 26–29 November 1965 Nauka, Leningrad, USSR, 1967, pp. 149–155, in Russian.*
31. Suntola, T.S., A.J. Pakkala, and S.G. Lindfors, *U.S. Patent No.4,413,022, 1 November 1983.*
32. Robertson, J., *High dielectric constant oxides.* The European Physical Journal - Applied Physics, 2004. **28**(03): p. 265-291.
33. Ritala, M., et al., *Development of crystallinity and morphology in hafnium dioxide thin films grown by atomic layer epitaxy.* Thin Solid Films, 1994. **250**(1–2): p. 72-80.
34. Aarik, J., et al., *Influence of substrate temperature on atomic layer growth and properties of HfO_2 thin films.* Thin Solid Films, 1999. **340**(1–2): p. 110-116.
35. Cho, M., et al., *Chemical interaction between atomic-layer-deposited HfO_2 thin films and the Si substrate.* Applied Physics Letters, 2002. **81**(2): p. 334-336.
36. Forsgren, K., et al., *Deposition of HfO_2 Thin Films in HfI_4-Based Processes.* Journal of The Electrochemical Society, 2002. **149**(10): p. F139-F144.
37. Rahtu, A., M. Ritala, and M. Leskelä, *Atomic Layer Deposition of Zirconium Titanium Oxide from Titanium Isopropoxide and Zirconium Chloride.* Chemistry of Materials, 2001. **13**(5): p. 1528-1532.
38. Aarik, J., et al., *Titanium isopropoxide as a precursor for atomic layer deposition: characterization of titanium dioxide growth process.* Applied Surface Science, 2000. **161**(3-4): p. 385-395.
39. Green, M.L., et al., *Nucleation and growth of atomic layer deposited HfO_2 gate dielectric layers on chemical oxide (Si-O-H) and thermal oxide (SiO_2 or Si-O-N) underlayers.* Journal of Applied Physics, 2002. **92**(12): p. 7168-7174.
40. Puurunen, R.L., *Analysis of hydroxyl group controlled atomic layer deposition of hafnium dioxide from hafnium tetrachloride and water.* Journal of Applied Physics, 2004. **95**(9): p. 4777-4786.
41. Ylilammi, M., *Monolayer thickness in atomic layer deposition.* Thin Solid Films, 1996. **279**: p. 124-130.
42. Kukli, K., et al., *Effect of selected atomic layer deposition parameters on the structure and dielectric properties of hafnium oxide films.* Journal of Applied Physics, 2004. **96**(9): p. 5298-5307.

43. Haukka, S., E.L. Lakomaa, and A. Root, *An IR and NMR study of the chemisorption of titanium tetrachloride on silica.* The Journal of Physical Chemistry, 1993. **97**(19): p. 5085-5094.
44. Haukka, S., et al., *Dispersion and distribution of titanium species bound to silica from titanium tetrachloride.* Langmuir, 1993. **9**(12): p. 3497-3506.
45. Puurunen, R.L., *Formation of Metal Oxide Particles in Atomic Layer Deposition During the Chemisorption of Metal Chlorides: A Review.* Chemical Vapor Deposition, 2005. **11**(2): p. 79-90.
46. Lysaght, P.S., et al., *Physicochemical properties of HfO_2 in response to rapid thermal anneal.* Applied Physics Letters, 2003. **82**(8): p. 1266-1268.
47. Elers, K.-E., et al., *$NbCl_5$ as a precursor in atomic layer epitaxy.* Applied Surface Science, 1994. **82–83**(0): p. 468-474.
48. Aarik, J. and H. Siimon, *Characterization of adsorption in flow type atomic layer epitaxy reactor.* Applied Surface Science, 1994. **81**: p. 281-287.
49. Kukli, K., et al., *Atomic Layer Deposition of Tantalum Oxide Thin Films from Iodide Precursor.* Chemistry of Materials, 2000. **13**(1): p. 122-128.
50. Pakkanen, T., *Atomic Layer Epitaxy*, ed. T. Suntola and M. Simpson. 1990, London: Blackie and Son.
51. Siimon, H. and J. Aarik, *Thickness profiles of thin films caused by secondary reactions in flow-type atomic layer deposition reactors.* Journal of Physics D: Applied Physics, 1997. **30**(12): p. 1725.
52. Nishizawa, J.i., H. Abe, and T. Kurabayashi, *Molecular Layer Epitaxy.* Journal of The Electrochemical Society, 1985. **132**(5): p. 1197-1200.
53. Bedair, S.M., et al., *Atomic layer epitaxy of III-V binary compounds.* Applied Physics Letters, 1985. **47**(1): p. 51-53.
54. Tischler, M.A. and S.M. Bedair, *Growth and characterization of compound semiconductors by atomic layer epitaxy.* Journal of Crystal Growth, 1986. **77**(1–3): p. 89-94.
55. Putkonen, M., M. Nieminen, and L. Niinistö, *Magnesium aluminate thin films by atomic layer deposition from organometallic precursors and water.* Thin Solid Films, 2004. **466**(1–2): p. 103-107.
56. Ott, A.W., et al., *Al_3O_3 thin film growth on Si(100) using binary reaction sequence chemistry.* Thin Solid Films, 1997. **292**(1–2): p. 135-144.
57. Groner, M.D., et al., *Electrical characterization of thin Al_2O_3 films grown by atomic layer deposition on silicon and various metal substrates.* Thin Solid Films, 2002. **413**(1–2): p. 186-197.
58. Puurunen, R.L., et al., *Island growth in the atomic layer deposition of zirconium oxide and aluminum oxide on hydrogen-terminated silicon: Growth mode modeling and transmission electron microscopy.* Journal of Applied Physics, 2004. **96**(9): p. 4878-4889.
59. Puurunen, R.L., et al., *Successive reactions of gaseous trimethylaluminium and ammonia on porous alumina.* Physical Chemistry Chemical Physics, 2001. **3**(6): p. 1093-1102.
60. Putkonen, M., et al., *ZrO_2 Thin Films Grown on Silicon Substrates by Atomic Layer Deposition with $Cp_2Zr(CH_3)_2$ and Water as Precursors.* Chemical Vapor Deposition, 2003. **9**(4): p. 207-212.
61. Niinisto, J., et al., *Controlled growth of HfO_2 thin films by atomic layer deposition from cyclopentadienyl-type precursor and water.* Journal of Materials Chemistry, 2005. **15**(23): p. 2271-2275.
62. Niinistö, J., et al., *Atomic Layer Deposition of HfO_2 Thin Films Exploiting Novel Cyclopentadienyl Precursors at High Temperatures.* Chemistry of Materials, 2007. **19**(13): p. 3319-3324.

63. Hiltunen, L., et al., *Growth and characterization of aluminium oxide thin films deposited from various source materials by atomic layer epitaxy and chemical vapor deposition processes.* Materials Chemistry and Physics, 1991. **28**(4): p. 379-388.
64. Kukli, K., M. Ritala, and M. Leskelä, *Atomic Layer Epitaxy Growth of Tantalum Oxide Thin Films from $Ta(OC_2H_5)_5$ and H_2O* Journal of The Electrochemical Society, 1995. **142**(5): p. 1670-1675.
65. Nykanen, E., et al., *Growth of PbS thin films from novel precursors by atomic layer epitaxy.* Journal of Materials Chemistry, 1994. **4**(9): p. 1409-1412.
66. Brei, V.V., V.A. Kaspersky, and N.U. Gulyanitskaya, *Synthesis and study of boron phosphate and titanium silicate compounds on silica surface.* Reaction Kinetics and Catalysis Letters, 1993. **50**(1-2): p. 415-421.
67. Ritala, M., et al., *Atomic Layer Deposition of Oxide Thin Films with Metal Alkoxides as Oxygen Sources.* Science, 2000. **288**(5464): p. 319-321.
68. Matero, R., et al., *Atomic layer deposition of ZrO_2 thin films using a new alkoxide precursor.* J. Non-Cryst. Solids, 2002. **303**: p. 24.
69. Kukli, K., M. Ritala, and M. Leskelä, Chem. Vap. Deposition, 2000. **6**: p. 297.
70. Rahtu, A., K. Kukli, and M. Ritala, *In Situ Mass Spectrometry Study on Atomic Layer Deposition from Metal (Ti, Ta, and Nb) Ethoxides and Water.* Chemistry of Materials, 2001. **13**(3): p. 817-823.
71. Rahtu, A. and M. Ritala, *Reaction Mechanism Studies on Titanium Isopropoxide–Water Atomic Layer Deposition Process.* Chemical Vapor Deposition, 2002. **8**(1): p. 21-28.
72. Pore, V., et al., *Atomic Layer Deposition of Photocatalytic TiO_2 Thin Films from Titanium Tetramethoxide and Water.* Chemical Vapor Deposition, 2004. **10**(3): p. 143-148.
73. Päiväsaari, J., M. Putkonen, and L. Niinistö, *A comparative study on lanthanide oxide thin films grown by atomic layer deposition.* Thin Solid Films, 2005. **472**(1–2): p. 275-281.
74. Nieminen, M., M. Putkonen, and L. Niinistö, *Formation and stability of lanthanum oxide thin films deposited from β-diketonate precursor.* Applied Surface Science, 2001. **174**(2): p. 155-166.
75. Elliott, S.D., *Improving ALD growth rate via ligand basicity: Quantum chemical calculations on lanthanum precursors.* Surface and Coatings Technology, 2007. **201**(22–23): p. 9076-9081.
76. Nilsen, O., H. Fjellvåg, and A. Kjekshus, *Growth of calcium carbonate by the atomic layer chemical vapour deposition technique.* Thin Solid Films, 2004. **450**(2): p. 240-247.
77. Kosola, A., et al., *Effect of annealing in processing of strontium titanate thin films by ALD.* Applied Surface Science, 2003. **211**(1–4): p. 102-112.
78. Putkonen, M., et al., *Low-Temperature ALE Deposition of Y_2O_3 Thin Films from β-Diketonate Precursors.* Chemical Vapor Deposition, 2001. **7**(1): p. 44-50.
79. Puurunen, R.L., *Growth Per Cycle in Atomic Layer Deposition: A Theoretical Model.* Chemical Vapor Deposition, 2003. **9**(5): p. 249-257.
80. Puurunen, R.L., *Growth Per Cycle in Atomic Layer Deposition: Real Application Examplesof a Theoretical Model.* Chemical Vapor Deposition, 2003. **9**(6): p. 327-332.
81. Jones, A.C., et al., *MOCVD of Zirconia Thin Films by Direct Liquid Injection Using a New Class of Zirconium Precursor.* Chemical Vapor Deposition, 1998. **4**(2): p. 46-49.
82. Putkonen, M. and L. Niinisto, *Zirconia thin films by atomic layer epitaxy. A comparative study on the use of novel precursors with ozone.* Journal of Materials Chemistry, 2001. **11**(12): p. 3141-3147.
83. Gordon, R.G., et al., *Vapor Deposition of Metal Oxides and Silicates: Possible Gate Insulators for Future Microelectronics.* Chemistry of Materials, 2001. **13**(8): p. 2463-2464.

84. Hausmann, D.M., et al., *Atomic Layer Deposition of Hafnium and Zirconium Oxides Using Metal Amide Precursors.* Chemistry of Materials, 2002. **14**(10): p. 4350-4358.
85. Min, J.-S., H.-S. Park, and S.-W. Kang, *Metal--organic atomic-layer deposition of titanium--silicon--nitride films.* Applied Physics Letters, 1999. **75**(11): p. 1521-1523.
86. Lim, J.-W., J.-S. Park, and S.-W. Kang, *Kinetic modeling of film growth rates of TiN films in atomic layer deposition.* Journal of Applied Physics, 2000. **87**(9): p. 4632-4634.
87. Kim, D.-J., et al., *Applicability of ALE TiN films as Cu/Si diffusion barriers.* Thin Solid Films, 2000. **372**(1–2): p. 276-283.
88. Kim, J.Y., et al., *Characteristics and Compositional Variation of TiN Films Deposited by Remote PEALD on Contact Holes.* Journal of The Electrochemical Society, 2005. **152**(1): p. G29-G34.
89. Becker, J.S., E. Kim, and R.G. Gordon, Chem. Mater, 2004. **16**: p. 3497-3501.
90. Zaera, F., *The surface chemistry of thin film atomic layer deposition (ALD) processes for electronic device manufacturing.* Journal of Materials Chemistry, 2008. **18**: p. 3521-3526.
91. Wada, S., et al., ECS Transactions, 2009. **25**(4): p. 209-216.
92. Kukli, K., et al., *Atomic Layer Deposition of Hafnium Dioxide Films from Hafnium Tetrakis(etheylmethylamide) and Water.* Chemical Vapor Deposition, 2002. **8**: p. 199.
93. Kamiyama, S., T. Miura, and Y. Nara, *Electrical properties of ultrathin HfO_2 films for replacement metal gate transistors, fabricated by atomic layer deposition using $Hf(N(CH_3)(C_2H_5))_4$ and O_3.* Applied Physics Letters, 2005. **87**(13): p. 132904-3.
94. Elam, J.W., et al., *Surface chemistry and film growth during TiN atomic layer deposition using TDMAT and NH3.* Thin Solid Films, 2003. **436**(2): p. 145-156.
95. Kukli, K., et al., *Evaluation of a Praseodymium Precursor for Atomic Layer Deposition of Oxide Dielectric Films.* Chemistry of Materials, 2004. **16**(24): p. 5162-5168.
96. Lim, B.S., A. Rahtu, and R.G. Gordon, *Atomic layer deposition of transition metals.* Nat Mater, 2003. **2**(11): p. 749-754.
97. Lee, B., et al., *A novel thermally-stable zirconium amidinate ALD precursor for ZrO_2 thin films.* Microelectronic Engineering, 2009. **86**(3): p. 272-276.
98. Lim, B.S., et al., *Atomic layer deposition of lanthanum aluminum oxide nano-laminates for electrical applications.* Applied Physics Letters, 2004. **84**(20): p. 3957-3959.
99. Huang, R. and A.H. Kitai, *Temperature-dependence of the growth orientation of atomic layer growth MgO.* Applied Physics Letters, 1992. **61**(12): p. 1450-1452.
100. Niinistö, J., et al., *Atomic Layer Deposition of High- k Oxides of the Group 4 Metals for Memory Applications.* Advanced Engineering Materials, 2009. **11**: p. 223-234.
101. Williams, P., et al., AVS 8th International Conference on Atomic Layer Deposition,Bruges, Belgium, 2008; AVS: New York; Presentation available on DVD.
102. Potts, S.E., et al., *Low Temperature Plasma-Enhanced Atomic Layer Deposition of Metal Oxide Thin Films.* J. Electrochem. Soc. , 2010. **157**: p. 66.
103. Langereis, E., et al., *Remote Plasma ALD of $SrTiO_3$ Using Cyclopentadienlyl-Based Ti and Sr Precursors.* Journal of The Electrochemical Society, 2011. **158**(2): p. G34-G38.
104. Blasco, N., et al., AVS 8th International Conference on Atomic Layer Deposition,Bruges, Belgium, 2008; AVS: New York; Presentation available on DVD.
105. Katamreddy, R., et al., *16.* ECS Trans. , 2008: p. 113.
106. Niinistö, J., et al., *In Situ Quadrupole Mass Spectrometry Study of Atomic-Layer Deposition of ZrO_2 Using $Cp_2Zr(CH_3)_2$ and Water.* Langmuir, 2005. **21**(16): p. 7321-7325.
107. Putkonen, M. and L. Niinistö, *Organometallic Precursors for Atomic Layer Deposition*, in *Precursor Chemistry of Advanced Materials*, R. Fischer, Editor. 2005, Springer Berlin Heidelberg. p. 125-145.

108. Gaskell, J.M., et al., *Liquid injection MOCVD and ALD of ZrO_2 using Zr–cyclopentadienyl precursors.* Surface and Coatings Technology, 2007. **201**(22–23): p. 9095-9098.
109. Rushworth, S., et al., *Thermal stability studies for advanced Hafnium and Zirconium ALD precursors.* Surface and Coatings Technology, 2007. **201**(22-23): p. 9060-9065.
110. Black, K., et al., *Deposition of ZrO_2 and HfO_2 thin films by liquid injection MOCVD and ALD using ansa-metallocene zirconium and hafnium precursors.* Journal of Materials Chemistry, 2008. **18**(38): p. 4561-4571.
111. Kukli, K., et al., *Behavior of zirconium oxide films processed from novel monocyclopentadienyl precursors by atomic layer deposition.* J. Vac. Sci. Technol. B 2009. **27**: p. 226-229.
112. Schrock, R.R., *Alkylidene complexes of niobium and tantalum.* Accounts of Chemical Research, 1979. **12**(3): p. 98-104.
113. Feldman, J. and R.R. Schrock, *Recent Advances in the Chemistry of "d^0" Alkylidene and Metallacyclobutane Complexes*, in *Progress in Inorganic Chemistry*. 2007, John Wiley & Sons, Inc. p. 1-74.
114. Schrock, R.R., *Living ring-opening metathesis polymerization catalyzed by well-characterized transition-metal alkylidene complexes.* Accounts of Chemical Research, 1990. **23**(5): p. 158-165.
115. Schrock, R.R., *High Oxidation State Multiple Metal-Carbon Bonds.* Chemical Reviews, 2002. **102**(1): p. 145-180.
116. Fürstner, A., *Groundbreaking Achievements in the Design of Well-Defined Metathesis Catalysts Shape Organic Synthesis.* Advanced Synthesis & Catalysis, 2002. **344**(6-7): p. 567-567.
117. Kealy, T.J. and P.L. Pauson, *A New Type of Organo-Iron Compound.* Nature, 1951. **168**: p. 4285.
118. Long, W.P. and D.S. Breslow, *Polymerization of Ethylene with Bis-(cyclopentadienyl)-titanium Dichloride and Diethylaluminum Chloride.* Journal of the American Chemical Society, 1960. **82**(8): p. 1953-1957.
119. Natta, G. and F. Danusso, *Stereoregular polymers and stereospecific polymerizations: the contributions of Giulio Natta and his school to polymer chemistry*. 1967: Symposium Publications Division, Pergamon Press.
120. Wilkinson, G., et al., *Bis-cyclopentadienyl derivatives of some transition elements* Journal of the American Chemical Society, 1953. **75**(4): p. 1011-1012.
121. Möhring, P.C. and N.J. Coville, *Group 4 metallocene polymerisation catalysts: quantification of ring substituent steric effects* 2006. **250**(1-2): p. 18-35.
122. Wailes, P.C., R.S.P. Coutts, and H. Weigold, *Organometallic Chemistry of Titanium, Zirconium and Hafnium*. 1974, New York: Academic Press Inc
123. Bergman, R.G., *Organometallic chemistry: C-H activation.* Nature, 2007. **446**(7134): p. 391-393.
124. Labinger, J.A. and J.E. Bercaw, *Understanding and exploiting C-H bond activation.* Nature, 2002. **417**(6888): p. 507-514.
125. *Methanol Industry*. Available from: http://methanol.org/Methanol-Basics/The-Methanol-Industry.aspx.
126. Berkaine, N., P. Reinhardt, and M.E. Alikhani, *Metal (Ti, Zr, Hf) insertion in the C-H bond of methane: Manifestation of an agostic interaction.* Chemical Physics, 2008. **343**(2-3): p. 241-249.
127. Andrews, L. and H.-G. Cho, *Matrix Preparation and Spectroscopic and Theoretical Investigations of Simple Methylidene and Methylidyne Complexes of Group 4−6 Transition Metals.* Organometallics, 2006. **25**(17): p. 4040-4053.

128. Andrews, L., H.-G. Cho, and X. Wang, *Reactions of Methane with Titanium Atoms: CH_3TiH, $CH_2=TiH_2$, Agostic Bonding, and $(CH_3)_2TiH_2$.* Inorganic Chemistry, 2005. **44**(13): p. 4834-4842.
129. Cho, H.-G., X. Wang, and L. Andrews, *Reactions of Methane with Hafnium Atoms: CH_2HfH_2, Agostic Bonding, and $(CH_3)_2HfH_2$.* Organometallics, 2005. **24**(12): p. 2854-2861.
130. Knobloch, D.J., E. Lobkovsky, and P.J. Chirik, *Dinitrogen cleavage and functionalization by carbon monoxide promoted by a hafnium complex.* Nat Chem, 2010. **2**(1): p. 30-35.
131. *Haber process*. Available from: http://en.wikipedia.org/wiki/Haber_process.

Chapter 2. Theoretical background

In the study of ALD reaction mechanisms, experimental analysis is limited in the degree in which it can analyze many individual aspects of a reaction, such as the Transition State (TS) or other fast intermediate complexes. While techniques like ultrafast spectroscopy may possibly be able to see the various states of a reaction, they each have limitations and added cost and complexity. Fourier Transform Infrared Spectroscopy (FTIR) can be affected by low sensitivity, Mass Spectroscopy is not a direct analysis method, and Synchrotron X-ray Photoelectron Spectroscopy (XPS), while extremely accurate, requires that the experiments are performed at a synchrotron: something to which not every research facility has easy access. To understand these processes, we thus turn to atomic-scale computational modelling, which is a complementary analysis technique to experiment that provides a much greater insight into the reaction mechanisms, specifically by revealing intermediate steps which may not be readily observable experimentally.

2.1 Computational Chemistry: Density Functional Theory

2.1.1 General electronic structure theory

One of the most powerful electronic structure analysis methods available currently is Density Functional Theory (DFT), which computes energy functions of wavefunctions (Ψ) (functionals[1]) that describe the electron states, to build up an interaction model between electrons in a many-body system. The end goal is the solution of the time-independent Schrödinger equation, the general form given in Equation 1, to some sufficiently accurate approximation.

$$\hat{H}\Psi_i\left(\vec{x}_1,\vec{x}_2,\ldots\vec{x}_N,\vec{R}_1,\vec{R}_2,\ldots\vec{R}_M\right)=E_i\Psi_i\left(\vec{x}_1,\vec{x}_2,\ldots\vec{x}_N,\vec{R}_1,\vec{R}_2,\ldots\vec{R}_M\right) \qquad \text{Equation 1}$$

In Equation 1, $\hat{H}$ is the Hamilton operator for a system of M nuclei and N electrons independent of the effects of an electric field, x_j is a coordinate describing the spin and position of each of the N electrons, R_k denotes the spatial coordinates of nucleus k, Ψ_i is the wavefunction of state i, and E_i is the energy of the state described by Ψ_i. The Hamiltonian

[1] Unlike a function, which takes a number as an input and returns a number, a functional takes a function as an input and returns a number.

operator consists of a sum of three terms, the kinetic energy, the interaction with the external potential and the electron-electron interaction. The external potential is the interaction of the electrons with the atomic nuclei.

To simplify the Schrödinger equation, it is valuable to consider the effects of modelling a system containing both electrons and nuclei. Because of the vast difference between their masses, nuclei and electrons move at significantly different speeds, with the heavier nuclei[2] appearing practically stationary from the reference frame of a light, fast-moving electron. The Born-Oppenheimer approximation, one of the most important approximations in quantum chemistry, takes the approximation of "practically stationary nuclei" and expands it so that the analysis is, in fact, done on a field of moving electrons and stationary nuclei. With this approximation, the potential energy due to intra-nuclear repulsion can be expressed simply as a constant and the kinetic energy of the nuclei is reduced to zero. By using the Born-Oppenheimer approximation, the solution of the Schrödinger equation only contains the electronic wavefunctions and energies.

2.1.2 Hartree-Fock theory

Within the Born-Oppenheimer approximation, the DFT analysis ultimately describes an interacting system of a number of electrons for which only the electron motion needs to be solved, described by a single Schrödinger equation of many bodies with an energy represented by the functional $E[\Psi]$. To solve such a system, we must find an N-electron wavefunction which gives the lowest energy for the functional $E[\Psi]$ and also satisfies the criteria to be a wavefunction: continuous everywhere and quadratic integratable. Searching for such a wavefunction in the space of all eligible wavefunctions, however, is prohibitively time-consuming and instead the set of possible wavefunctions is restricted to a likely subset of all wavefunctions. While there are many possible subsets to choose from, one of the simplest methods, the Hartree-Fock method, takes the many-electron wavefunction and expresses it as Hartree product (Slater determinant) of single-particle functions, as in Equation 2.

$$\Psi_i\left(\vec{x}_1, \vec{x}_2, \ldots \vec{x}_N\right) = \psi_1\left(\vec{x}_1\right)\psi_2\left(\vec{x}_2\right)\ldots\psi_N\left(\vec{x}_N\right) \qquad \text{Equation 2}$$

[2] The mass of H, the lightest proton, is approximately 1800 times that of an electron.

The Hartree-Fock method describes the problem as a set of one-electron spatial spin-orbitals: the product of a given spatial orbital and one of two orthonormal spin functions. Each of these wavefunctions, ψ, satisfies a one-electron Schrödinger Equation, where the average field of the other electrons defines the potential term. The Hartree-Fock method often provides a good model of chemical bonding and by using it we are able to obtain bond lengths, vibrational frequencies, and some relative energies in the case of main group element compounds [1].

One limiting aspect of the Hartree-Fock method is that only certain products of single-electron wavefunctions are suitable. Because electrons are indistinguishable, it is not possible to simply assign a single-electron wavefunction to a specific electron. The set of functions, therefore, must have an antisymmetrized product - a product where if any two parameters are interchanged, its sign changes. Such a product is termed the Slater Determinant, Φ_{SD}, which is given in Equation 3

$$\Phi_{SD} = \frac{1}{\sqrt{N!}} \det\left\{\psi_1\left(\vec{x}_1\right)\psi_2\left(\vec{x}_2\right)..\psi_N\left(\vec{x}_N\right)\right\} \qquad \text{Equation 3}$$

In Equation 3, the functions $\psi_i\left(\vec{x}_i\right)$ are the spin orbitals. These spin orbitals are then varied, as described in the Hartree-Fock method, yet kept orthonormal, until the energy expectation value (E_{HF}) of the Slater Determinant is minimized. The result is a set of wavefunctions of *N* electrons. This E_{HF} is therefore a functional of the spin orbitals from the Slater Determinant and is minimized by introducing a set of Lagrangian multipliers. The Lagrangian multipliers are the physical orbital energies and are themselves eigenvalues of the one-electron "Fock Operator".

Numerically, the minimization procedure is carried out through application of the Self-Consistent Field (SCF) method. Here, the Fock Operator is diagonalized to obtain a set of orbitals which are compared to the orbitals that themselves went into forming the operator. The new orbitals are then used to build a new Fock Operator and the process is repeated until the desired degree of consistency is obtained between input and output orbitals. The final operator, which can require various computational methods to assist in convergence, will then yield the set of orbitals that describe the *N*-electron problem at the Hartree-Fock level.

2.1.3 Density Functional Theory

The Kohn-Sham formulation [2, 3] of Density Functional Theory builds on Hartree-Fock theory by defining a system of *N* electrons in a non-interacting reference system built up from a set of orbitals. This method allows a large part of the kinetic energy to be computed to a good degree of accuracy. This arises since the Slater Determinant can be considered in two ways: as the approximation of the *N*-electron system discussed previously or as the exact wavefunction of a system of non-interacting electrons. In this second case, by applying a Hamiltonian with a local, effective potential, $V_s\left(\vec{x}\right)$, we can define a non-interacting reference system.

The effective potential includes the external potential and the effects of the interactions between the electrons, e.g., the exchange and correlation interactions. By careful selection of this effective potential, the density of the created system can match the ground state density of the desired system of interacting electrons. The total energy, being a functional of the density, can therefore be determined to some sufficiently accurate degree.

In practice, the utility of the theory rests on the approximation used for the exchange-correlation functional,[2] which is the sum of the error made in using a non-interacting kinetic energy and the error made in treating the electron-electron interaction classically. In other words, the exchange-correlation energy E_{XC} is the functional that contains everything that is unknown.

There are different functionals available that are more or less accurate for a studied system. The choice of which of these functionals to use depends on direct comparison with a more accurate theory or experimental data.

The simplest approximation is the local-density approximation (LDA), which is based upon the exact exchange energy for a uniform electron gas, which can be obtained from the Thomas–Fermi model [3, 4]. If the electron-electron interaction is approximated by the classical Hartree potential (exchange and correlation effects are neglected) then the total energy functional can be computed. In this case, the dependence of the kinetic and exchange energy on the density of the electron gas can be expressed as a local function of

the density. Further, the functional of the inhomogeneous system is approximated as an integral over a local function of the density. As a result the exchange and correlation energy density is the function of only the local value of the density. Central to this model is the assumption that we can write E_{XC} in the simple form of Equation 4:

$$E_{xc}[\rho] = \int \rho(\vec{r})\epsilon_{xc}\left(\rho(\vec{r})\right)d\vec{r} \qquad \text{Equation 4}$$

The exchange-correlation energy is decomposed into exchange and correlation terms linearly, given in Equation 5

$$E_{\mathrm{xc}}^{\mathrm{LDA}} = E_x^{LDA} + E_c^{LDA} \qquad \text{Equation 5}$$

In Equation 4, $\epsilon_{xc}\left(\rho(\vec{r})\right)$ is the exchange-correlation energy per particle of a uniform electron gas of density ρ. This energy is weighted with the probability that there is, in fact, an electron at this position in space. The conditional probability of finding an electron at r_2 given that there is an electron at r_1 is known as the exchange-correlation hole. The exchange-correlation hole of the uniform electron gas, which is used as model for the exact hole in the local density approximation, satisfies most of the important relations established for the true hole. However, the LDA model hole and the exact hole differ in many details. The centered LDA exchange hole is a better approximation for the more homogeneous molecular density than for the more inhomogeneous density of atoms. In particular, this causes the exchange energy of the molecular system to be too negative. In other words it causes a large overbinding.

The LDA produces large errors in the exchange and correlation energy, however the exchange energy is generally underestimated and the correlation energy overestimated and these errors tend to cancel. As a result of this, the LDA can be quite successful. The other reason for the success of the LDA is also due to the fact that the corresponding exchange-correlation hole system obeys most of the rules of the real system.

Local-density approximations are the starting point for the construction of more sophisticated approximations to the exchange-correlation energy, such as general gradient approximation (GGA) or hybrid functionals. This is because a desirable property of any approximate exchange-correlation functional is that it reproduces the exact results of the homogenous electron gas for non-varying densities. Thus, LDAs are often an explicit component of such functionals. However in order to account for the non-homogeneity of the true electron density it is important to use not only the information about the density at

a particular point, but to supplement the density with information about the gradient of the density. A natural progression beyond the LDA is thus to the gradient expansion approximation (GEA) in which first order gradient terms in the expansion are included. However, this results in an approximation for the exchange hole [5] which has a number of unphysical properties. For that reason the GEA does not lead to the desired improved accuracy but frequently performs even worse than the simple local density approximation. The problem was solved within the generalised gradient approximation (GGA) where the hole constraints have been restored simply by enforcing the restrictions for the hole [6]. The energy functional depends here on both the density and its gradient but retains the analytic properties of the exchange correlation hole as it is in the LDA. The form for a GGA functional is thus given in Equation 6.

$$E_{xc}[\rho_\alpha, \rho_\beta] = \int f(\rho_\alpha, \rho_{\beta,} \nabla\rho_\alpha, \nabla\rho_\beta) d\vec{r} \qquad \text{Equation 6}$$

In Equation 6, E_{XC} is often split into its exchange and correlation contributions as in Equation 7.

$$E_{xc}^{\mathrm{GGA}} = E_x^{GGA} + E_c^{GGA} \qquad \text{Equation 7}$$

The GGA improves significantly on the LDA's description of the binding energy of molecules. In particular, this feature led to the very widespread acceptance of DFT in the chemistry community during the early 1990's. A number of functionals within the GGA family [6-9] have been subsequently developed. The gradient-corrected exchange functionals include Becke88 (B), Perdew-Wang (PW91), Modified Perdew-Wang by Barone and Adamo (MPW), Gill96 (G96), and Perdew-Burke-Ernzerhof (PBE), while the gradient-corrected correlation functionals are Lee, Yang, and Parr (LYP), Perdew-Wang (PW91), Perdew 86 (P86), Becke96 (B96), and Perdew-Burke-Ernzerhof (PBE). The names of these functionals refer to their respective authors and the year of publication. In principle, each exchange functional could be combined with any of the correlation functionals, but only a few combinations are in use. The BLYP method, for example, combines Becke's 1988 exchange functional with the correlation functional by Lee, Yang, and Parr. Another often used GGA functional is BP86 composed of the Becke 1988 exchange functional and the Perdew 86 correlation functional. Thousands of benchmarking studies have been carried out, from which a frequent conclusion is that these methods produce results of similar quality [10].

Hybrid functionals are approximations to the exchange-correlation energy functional that incorporate a portion of the exact exchange energy functional from Hartree-Fock theory, along with exchange and correlation density functionals from DFT. Currently, the most popular and widely used hybrid functional is known as B3LYP, which stands for Becke, 3-parameter, Lee-Yang-Parr. The parameters define the hybrid functional, specifying how much of the exact exchange is mixed in. Hybrid functionals often perform better than LDA or even GGA approaches in predicting molecular geometries. For example, bond lengths computed in the G2 set[3] [11] using B3LYP and B3P86 show an average absolute deviation from experiment of 0.013 Å and 0.010 Å compared to 0.026 Å and 0.022 Å for the pure GGA functional BLYP and BP86, respectively [10].

2.2 Tools used in this work

In this work, a variety of computational tools have been used to carry out the DFT calculations and analysis. The most important of these is TURBOMOLE [12], the package in which the DFT calculations are directly performed. TURBOMOLE performs DFT analysis using atom-centered orbitals and this makes it suitable for gas-phase molecules and clusters.

The VASP package [13, 14] is another DFT package, which uses a plane wave basis set, rather than the atom-centered orbitals in TURBOMOLE [12]. The plane-wave approach is well suited to simulate condensed phases and surfaces and will be used for the latter in this thesis.

Other software tools were used to assist in the DFT calculation, such as MaterialsStudio. This package is used to create the atomic coordinates for use in DFT calculations, as well for analysis after the DFT calculation.

Viewmol and Xmakemol are other tools for graphically manipulating and viewing chemical systems, each with a range of options as to display different information about the system. Both are able to create and view atomic systems for a variety of input and output formats.

[3] The G2 set is the thermochemical data base which contains more than 50 experimentally well-established atomization energies of small molecules containing main group elements.

1. Szabo, A. and N.S. Ostlund, . Modern Quantum Chemistry, (McGraw Hill, New York, 1989)
2. Kohn, W. and L.J. Sham, *Self-Consistent Equations Including Exchange and Correlation Effects.* Physical Review, 1965. **140**(4A): p. A1133-A1138.
3. Parr, R.G. and W. Yang, *Density-Functional Theory of Atoms and Molecules*. 1989: Oxford University Press, USA.
4. Dirac, P.A.M., *Note on Exchange Phenomena in the Thomas Atom.* Mathematical Proceedings of the Cambridge Philosophical Society, 1930. **26**(03): p. 376-385.
5. Dreizler, R.M. and E.K. Gross, *Density functional theory : an approach to the quantum many body problem*. 1995, Berlin [u.a.]: Springer.
6. Perdew, J.P. and W. Yue, *Accurate and simple density functional for the electronic exchange energy: Generalized gradient approximation.* Physical Review B, 1986. **33**(12): p. 8800-8802.
7. Langreth, D.C. and M.J. Mehl, *Beyond the local-density approximation in calculations of ground-state electronic properties.* Physical Review B, 1983. **28**(4): p. 1809-1834.
8. Becke, A.D., *Density-functional exchange-energy approximation with correct asymptotic behavior.* Physical Review A, 1988. **38**(6): p. 3098-3100.
9. Lee, C., W. Yang, and R.G. Parr, *Development of the Colle-Salvetti correlation-energy formula into a functional of the electron density.* Physical Review B, 1988. **37**(2): p. 785-789.
10. Koch, W. and M.C. Holthausen, *A Chemist's Guide to Density Functional Theory. By Wolfram Koch and Max C. Holthausen*. 2001: WILEY-VCH Verlag GmbH.
11. Curtiss, L.A., et al., *Gaussian-2 theory for molecular energies of first- and second-row compounds.* The Journal of Chemical Physics, 1991. **94**(11): p. 7221-7230.
12. Ahlrichs, R., et al., *Electronic structure calculations on workstation computers: The program system turbomole.* Chemical Physics Letters, 1989. **162**(3): p. 165-169.
13. Kresse, G. and J. Hafner, *Ab initio molecular-dynamics simulation of the liquid-metal–amorphous-semiconductor transition in germanium.* Physical Review B, 1994. **49**(20): p. 14251-14269.
14. Kresse, G. and J. Furthmüller, *Efficiency of ab-initio total energy calculations for metals and semiconductors using a plane-wave basis set.* Computational Materials Science, 1996. **6**(1): p. 15-50.

Chapter 3. An *ab initio* evaluation of cyclopentadienyl precursors for the atomic layer deposition of hafnia and zirconia

This chapter was published in *"ECS Transactions"* as:

A. Zydor, S. Elliott, T. Leese, F. Song and S. Rushworth, *ECS Trans.* 2007, Volume **11**, Issue 7, Pages 113-121.

Reproduced with permission from ECS Trans. **2007** volume 11, issue 7, **113-121**. Copyright 2007, The Electrochemical Society.

For this chapter I did the calculations and the analysis related to the calculations

.

Thin film dielectrics based on hafnium or zirconium oxides are being introduced to increase the permittivity of insulating layers in nanoelectronic transistor and memory devices. Atomic layer deposition (ALD) is the process of choice for fabricating these films, and the success of this method depends crucially on the chemical properties of the precursor molecules. Much promise is shown by Hf and Zr precursors that contain cyclopentadienyl ($Cp=C_5H_{5-x}R_x$) ligands. We have carried out *ab initio* calculations of a range of heteroleptic metallocenes $[M(Cp)_{4-n}(L)_n]$, M = Hf/Zr, L = Me and OMe. Based on optimized monomer structures, we analyze reactivity with respect to ligand elimination, independent of surface effects, and thus compare the reactivity of the Cp-based precursors with amines and halides. The order in which different ligands are eliminated during ALD follows their energetics. The utility of computed dipole moments in predicting precursor volatility is discussed.

3.1 Introduction

Thin film dielectrics based on hafnium or zirconium oxides are being introduced instead of silica to increase the permittivity (*k*) of insulating layers in nanoelectronic transistor and memory devices [1]. Atomic layer deposition (ALD) is the leading process for depositing thin, conformal high-*k* films [2]. This is a surface-controlled variant of chemical vapour deposition (CVD) where the substrate is alternately and separately exposed to different vapour-phase precursors. The precursor pulses are separated by inert gas purges to eliminate gas-phase reactions and remove volatile by-products. The first reactant is chemisorbed on the substrate during the first pulse until the surface is saturated and no further reaction occurs. This layer reacts with the second precursor during the second pulse, again to saturation. The cycle is repeated and a solid film is built up, layer by layer, in a slow and controlled fashion. In contrast to CVD and other techniques, ALD allows the growth of films of high uniformity and conformality. Because of the steadiness of growth, control of thickness and composition down to the atomic level is possible. However, the viability of the process depends on using suitable precursor molecules. A successful ALD precursor should be volatile, stable in the gas-phase, but reactive on the substrate and growing surface, leading to inert by-products.

These are quite different criteria to those for standard MOCVD. The most popular precursors to date for zirconia and hafnia ALD have been halides such as MCl_4 and amides $M(NR_2)_4$, M = Zr/Hf, (see *e.g.* Table 1 in ref. [3]), but each poses distinct challenges [4].

Recently, high quality ZrO_2 and HfO_2 films have been deposited by ALD from methyl metallocenes [3-7], which are heteroleptic complexes that include methyl (Me = CH_3) and cyclopentadienyl ligands (Cp = $C_5H_{5-n}R_n$) [7]. $ZrCp_2Me_2$ sublimed at < 150°C at 2-3 mbar, leaving a few % residue, and in ALD with ozone it produced films at a rate of 0.6 Å/cycle at 310-365°C [3],[5]. Using $HfCp_2Me_2$ and ozone gave a slightly lower growth rate of 0.4 Å/cycle at 350°C [8]. Both precursors are solid and decompose thermally above 450°C.

Improved thermal stability has been achieved with substituted cyclopentadienyl precursors. $Hf(CpMe)_2(Me)_2$ and $Hf(CpMe)_2(Me)(OMe)$ have been used with O_3 and H_2O at 350-500°C to give ALD at growth rates of 0.5 and 0.4 Å/cycle respectively [4]. It is not clear why this

minor change in the Cp ligands gives such a dramatic improvement in thermal stability. Another advantage is that these precursors are liquids under conditions suitable for introduction of vapours to ALD systems (2-3 mbar, 60-65°C). $Hf(Cp)_2(OMe)_2$ and $Hf(CpMe)_2(OMe)_2$ volatilise at similar temperatures, give slightly higher growth rates, but decompose at lower temperatures (350-400°C).

This study is concerned with investigating minor molecular changes and their impact on the ALD of MO_2 films (M = Hf, Zr) using the combination of metal-containing precursor ML_4 and an oxygen source, such as H_2O or O_3. There are abundant protons on the surface of the growing oxide film (as OH groups) after the oxygen-containing pulse and purge. During the ML_4 pulse, precursor molecules adsorb and ligands are eliminated (as HL) by combining with remnants from the previous pulse, until the surface is saturated by ML_{4-n} fragments. The more HL that can be eliminated during this pulse, the more M that can adsorb and the higher the ALD growth rate. For a given size of ligand, there is thus a linear relationship between the amount of HL eliminated and the growth rate [9]. We therefore assert that ligand elimination is the critical surface reaction of ALD. Previous authors have computed the energetics of ligand elimination to evaluate the reactivity of ALD precursors [10-12][13]. We neglect other surface reactions, such as adsorption, diffusion and desorption, which probably have a secondary influence on ALD growth rate.

To find out why some of these precursor molecules are more successful in ALD than others, we carry out an *ab initio* study of the thermochemistry that underlies their surface reactivity. The aim is to obtain insights into the reaction mechanism for heteroleptic precursors and into the effect of chemical substitution.

3.2 Method

The precursor molecules and their ALD reaction products were modelled as isolated molecules in vacuum. The ground state electronic wavefunction of each molecule was calculated self-consistently within Kohn-Sham Density Functional Theory (DFT) using the TURBOMOLE suite of quantum chemical programs [14]. All species were closed shell. Unconstrained optimisation of the molecular geometry was carried out on the DFT potential energy hypersurface, but a vibrational analysis was not carried out. A good trade-off

between accuracy and computational cost was obtained by using the B-P86 functional [15, 16], the RI approximation [17-19] and the atom-centred SV(P) basis set [20] with effective core potentials of 28 electrons on Zr and of 60 electrons on Hf [21].

DFT yields accurate gas-phase structures, charge distributions (*e.g.* dipole moment) and reaction energetics (ΔE), so that the main source of error in this study is likely to be the choice of precursor model. We have chosen to compute ML_4 monomers in vacuum, looking at a wide range of different L. Some of these precursors probably evaporate as dimers M_2L_8 or as larger oligomers, which may be investigated in future work because of the relevance to volatility. For the purposes of the present analysis however, it is important that we restrict the study to a comparable series of molecules, namely 4-fold coordinated ML_4 monomers, and we will limit our analysis to those results that are insensitive to the size of oligomer. Even so, η^5-Cp ligands complicate this picture because they may behave like ligands of greater than 1-fold coordination.

As a model for ligand elimination, we evaluate the energetics of hydrolysis of the gas-phase precursor, where hydrolysis refers here to the replacement of ligand L with OH in the M complex and liberation of HL. Previous authors have also computed this quantity to evaluate the reactivity of ALD precursors, often termed 'ligand exchange'. $M(OH)_4$ is chosen as the reference system, common for all L, which is appropriate for the ALD of MO_2 because it involves the formation of M—O bonds. The actual ligand elimination reactions during ALD lead to the growth of an extended M—O network and this cannot be modelled by a small gas-phase cluster, as here. However the cluster model is appropriate for comparison of the chemistry that is intrinsic to different ligands, which is the aim of this study. Assuming thermodynamic equilibrium between surface fragments and gas-phase products, the amount of HL eliminated will depend on the energy change ΔE_{hyd} for the reaction.

$$ML_4 + 4H_2O \rightarrow M(OH)_4 + 4HL \qquad \text{Equation 1}$$

(If kinetically controlled, the activation energy for the reaction may also scale approximately with ΔE_{hyd}). We compute the change in internal energy and neglect entropy and zero-point effects, which may be approximately equal across the range of ligands compared here. Negative ΔE_{hyd} correspond to exoergic hydrolysis reactions at T=0 K.

Since many of the precursors that we consider are heteroleptic, *e.g.* $ML^1_xL^2_{4-x}$, ligand exchange may occur, during synthesis, storage or deposition, leading to a more stable isomer complex $ML^1_yL^2_{4-y}$. For the purposes of computation, we have considered all the possible ligand exchange reactions of each dimer $2ML^1_xL^2_{4-x}$ and have defined ΔE_{exch} as half ΔE of the most favourable such ligand exchange reaction. We assume that trimers and larger oligomers react in a similar way. Thus for the example of $ZrCp_2Me_2$, ΔE is computed for the following reactions:

$$ZrCp_2Me_2 \rightarrow ½.ZrCp_3Me + ½.ZrCpMe_3 \qquad \text{Equation 2}$$

$$ZrCp_2Me_2 \rightarrow ½.ZrCp_4 + ½.ZrMe_4 \qquad \text{Equation 3}$$

and the ΔE_{exch} that we quote is the lower of the two ΔE. Again, entropy and finite temperature effects are neglected.

3.3 Results

The 30 ZrL_4 and 11 HfL_4 homoleptic and heteroleptic precursors were computed using DFT. Local energetic minima were found for each precursor composition and no spontaneous decomposition reactions were observed. Examples of optimized structures are shown in Figure 1. There was sufficient space around the Zr/Hf centre in all monomers for all 5 atoms of the Cp ring to coordinate to the metal (η^5), with the exception of MCp_4, which shows one η^1-Cp. Zr—C distances ranged 224-234 pm for Zr-CH_3, 251 pm for Zr-(η^1-Cp) and 254-265 pm for Zr-(η^5-Cp). The optimum Zr—O distances in Zr-OCH_3 were in the range 195-199 pm. Distances to Hf were shorter by $\leq$1 pm than those to Zr.

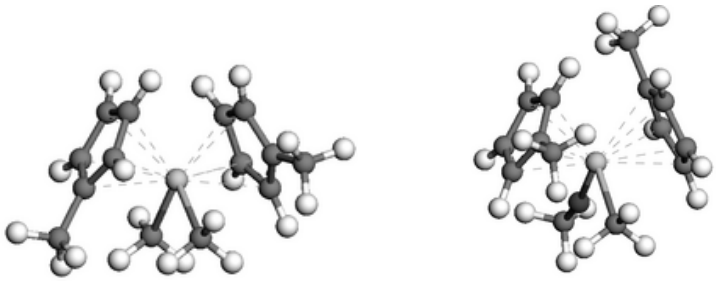


Figure 1. Computed structures of $Zr(\eta^5\text{-}CpMe)_2(Me)_2$, left, and $Zr(\eta^5\text{-}CpMe)_2(Me)(OMe)$, right (light-gray central atom = Zr, black = O, mid-gray = C, white = H). The corresponding Hf structures are very similar.

3.3.1 Reactivity and ALD growth rate

The computed ΔE_{hyd} data in Table I show that Zr-C bonds are much less stable than Zr-O bonds. The theoretical precursor $ZrMe_4$ has the most negative ΔE_{hyd} (nearly -900 kJ/mol), which is consistent with the difficulty of synthesis of alkyl zirconium compounds. By contrast, ΔE_{hyd}=+33 kJ/mol for the alkoxide $Zr(OMe)_4$ implies that elimination of MeOH is exoergic and that ALD growth would be slow. Similar energetics have been computed for $ZrCl_4$ (+78 kJ/mol in Table II; see also refs [11], [12]) and for $HfCl_4$ [12, 22] and are known to correlate with a low ALD growth rate. This positive value for ΔE_{hyd} is not consistent with the known hygroscopic properties of solid $ZrCl_4$ or $HfCl_4$ at room temperature However, the entropy of reaction of these solids with water is likely to substantially favor the reaction products. Other studies showed that replacement of only one Cl^- ligand with one OH^- group is exothermic [23]. However in our model, ΔE_{hyd} of the reaction Equation 1 is based on the replacement of all four ligands.

A moderately exoergic ΔE_{hyd} = -364 kJ/mol is obtained for $ZrCp_4$. We computed a similar value for the amines $Zr(NR^1R^2)_4$, *e.g.* ΔE_{hyd} = -382 kJ/mol for $R^1 = R^2$ = Me (Table II), or -96 kJ/mol per ligand, which compares well with previously computed values (-115 kJ/mol-ligand, ref. [13]). We therefore expect that the amines and metallocenes would perform similarly well in ALD, with comparable growth rates and similar optimum growth temperatures. We find that the overall reactivity of $ZrCp_4$ is modified upwards by successively replacing Cp with Me (ΔE_{hyd} = -403, -498, -698 kJ/mol) and downwards by replacing Cp with OMe (-233, -90, -14 kJ/mol). Within this Cp-Me-OMe family, mixed compounds of all three ligands also show a roughly linear relationship between ligand identity and ΔE_{hyd}.

There are however slight non-linearities in the energetics of the mixed compounds, which mean that certain compositions are favoured over others. This is apparent in the energetics of ligand exchange: for each heteroleptic Zr precursor, Table I shows ΔE_{exch} for the most likely such ligand exchange reaction. On the basis of ΔE_{exch}, $ZrCp_2Me_2$ is found to be the most stable compound in a mixture of Cp and Me ligands (ΔE_{exch} = 53 kJ/mol), while $ZrCpMe_3$ is marginally metastable against decomposition ($\Delta E_{exch} < 0$). This is consistent with the

successful synthetic route, where lithium complexes of the CpMe and Me ligands reacted with $HfCl_4$ to give the $Hf(CpMe)_2(Me)_2$ product in good yield (70% yield; ref. 4). The $Hf(MeCp)Me_3$ compound prepared by a similar route gave lower yield and proved to be less thermally stable. Likewise $ZrCp_2(OMe)_2$ is the most stable of the Cp/OMe complexes and $ZrCp_3(OMe)$ is predicted to decompose. We compute a slight energy gain (-13.1 kJ/mol) for the formation of $ZrCp_2(Me)(OMe)$ from $ZrCp_2Me_2 + ZrCp_2(OMe)_2$.

Table II shows the results of calculations on a variety of bulky substituted-cyclopentadienyls $M(CpR)_2(Me)_2$ for both M = Zr and M = Hf The identity of the metal cation has a small effect on ALD energetics: replacing Zr by Hf lowers ΔE_{hyd} by 17-25 kJ/mol for all Cp-derived complexes and by 2-9 kJ/mol for the amines given in Table II, meaning that the Hf precursors are slightly more reactive in ALD.

In our calculations, the effect of straight-chain substituent R on the Cp ligand is seen to be minor, adjusting ΔE_{hyd} by just -13 kJ/mol (R = Me) to +19 kJ/mol (R = ^{n}Pr) for both Zr and Hf. Steric crowding does not appear to be occurring within the ligand sphere: with just one substituent per Cp, the R groups are probably able to avoid each other in space. Thus, $Zr(CpMe)_2(Me)_2$ is predicted to show very similar energetics for ligand elimination as its non-substituted analogue $Zr(Cp)_2(Me)_2$ and the same is predicted to be true for $Zr(MeCp)_2(Me)(OMe)$ and the corresponding Hf series of compounds.

The effect of various alkoxide ligands is considered in Table III for the series of complexes $Zr(CpMe)_2(Me)(OR)$. Once more, the effect of R is relatively minor, augmenting ΔE_{hyd} by -11 to -26 kJ/mol as alkoxide bulk increases, probably indicative of a slight increase in crowding around Zr.

TABLE I. Calculated properties of precursors ZrL_4, L = Cp, Me and OMe. ΔE_{hyd} is the energy of reaction (Equation 1). ΔE_{exch} is the reaction energy for ligand exchange; only the lowest ΔE_{exch} is quoted but all others may be determined from ΔE_{hyd}.

Precursor	ΔE_{hyd} / kJ.mol-1 of ML_4	Dipole moment / D	Products with lowest ΔE_{exch}	ΔE_{exch} / kJ.mol-1 of ML_4
$Zr(\eta5\text{-}Cp)_3(\eta1\text{-}Cp)$	-363.8	3.5	$Zr(Cp)_4$	0.0
$Zr(Cp)_3(Me)$	-403.0	1.1	$Zr(Cp)_4+Zr(Cp)_2(Me)_2$	27.8
$Zr(Cp)_3(OMe)$	-233.4	0.7	$Zr(Cp)_4+Zr(Cp)_2(OMe)_2$	-6.3
$Zr(Cp)_2(Me)_2$	-497.7	1.5	$Zr(Cp)_3(Me)+Zr(Cp)(Me)_3$	53.0
$Zr(Cp)_2(Me)(OMe)$	-281.0	1.4	$Zr(Cp)_2(Me)_2+Zr(Cp)_2(OMe)_2$	13.1
$Zr(Cp)_2(OMe)_2$	-90.4	0.9	$Zr(Cp)_3(OMe)+Zr(Cp)(OMe)_3$	33.1
$Zr(Cp)(Me)_3$	-698.4	0.7	$Zr(Cp)_2(Me)_2+Zr(Me)_4$	-2.5
$Zr(Cp)(Me)_2(OMe)$	-451.0	1.8	$Zr(Cp)_2(Me)_2+Zr(Me)_2(OMe)_2$	1.5
$Zr(Cp)(Me)(OMe)_2$	-220.5	1.7	$Zr(Cp)_2(Me)(OMe)+Zr(Me)_3(OMe)$	9.5
$Zr(Cp)(OMe)_3$	-13.6	0.8	$Zr(Cp)_2(OMe)_2+Zr(OMe)_4$	14.9
$Zr(Me)_4$	-894.1	0.0	$Zr(Me)_4$	0.0
$Zr(Me)_3(OMe)$	-647.8	1.5	$Zr(Me)_4+Zr(Me)_2(OMe)_2$	2.8
$Zr(Me)_2(OMe)_2$	-407.1	2.2	$Zr(Me)_3(OMe)+Zr(Me)(OMe)_3$	6.2
$Zr(Me)(OMe)_3$	-178.8	2.0	$Zr(Me)_2(OMe)_2+Zr(OMe)_4$	8.0
$Zr(OMe)_4$	+33.4	0.0	$Zr(OMe)_4$	0.0
$Zr(OH)_4$	0.0	0.0	-	-

TABLE II. Calculated effect of bulk (R) of cyclopentadienyl ligand for precursors $M(RCp)_2(Me)_2$ with M = Zr, Hf and R = H, Me [CH_3], Et [C_2H_5], ^{n}Pr [$CH_2CH_2CH_3$], ^{n}Bu [$CH_2CH_2CH_2CH_3$], and for $M(RCp)_2(Me)(OMe)$ for R = H, Me. Data for common amine and halide precursors are given for comparison.

Precursor	ΔE_{hyd} / kJ.mol^{-1} of ML_4		Dipole moment / D	
	M = Zr	M = Hf	M = Zr	M = Hf
$M(Cp)_2(Me)_2$	-497.7	-515.6	1.5	1.4
$M(CpMe)_2(Me)_2$	-510.3	-529.0	1.3	1.3
$M(CpEt)_2(Me)_2$	-476.2	-495.0	1.3	1.3
$M(Cp^nPr)_2(Me)_2$	-478.7	-497.2	1.5	1.5
$M(Cp^nBu)_2(Me)_2$	-481.4	-506.1	1.5	1.6
$M(Cp)_2(Me)(OMe)$	-281.0	-300.0	1.4	1.4
$M(CpMe)_2(Me)(OMe)$	-296.6	-315.4	1.6	1.5
$M(NMe_2)_4$	-373.6	-381.9	0.3	0.3
$M(NEtMe)_4$ = TEMAZ/TEMAH	-379.2	-381.4	0.2	0.2
$M(NEt_2)_4$	-424.2	-429.2	0.3	0.3
MCl_4	+78.2	+67.6	0.0	0.0

TABLE III. Calculated effect of bulk (R) of alkoxide ligand in precursors $Zr(CpMe)_2(Me)(OR)_4$ with R = Me, Et, ^{i}Pr $[C(CH_3)_2]$, ^{t}Bu $[C(CH_3)_3]$, ^{neo}Pe $[CH_2C(CH_3)_3]$.

Precursor	ΔE_{hyd} / kJ.mol^{-1} of ML_4	Dipole moment / D
$Zr(CpMe)_2(Me)(OMe)$	-296.6	1.6
$Zr(CpMe)_2(Me)(OEt)$	-307.5	1.8
$Zr(CpMe)_2(Me)(O^{i}Pr)$	-313.0	1.7
$Zr(CpMe)_2(Me)(O^{t}Bu)$	-322.4	1.6
$Zr(CpMe)_2(Me)(O^{neo}Pe)$	-310.7	1.5

3.3.2 Dipole moment and volatility

Tables I and II show that homoleptic complexes ML^1_4 are computed to have low dipole moment, as expected, because they are tetrahedrally-symmetric [$M(Me)_4$, $M(OMe)_4$, MCl_4] or nearly symmetric [$M(NR^1R^2)_4$]. The exception is MCp_4, where crowding between Cp groups distorts the ligand shell, resulting in one η^1-ligand and a large dipole moment (3.5 D, Table I).

The heteroleptic complexes have inherently lower symmetry and show a wide range of dipole moments. A slightly lower dipole moment for complexes with Cp ligands is discernible relative to those with Me or OMe [*e.g.* 0.7-0.8 D for $ZrCpMe_3$ and $ZrCp(OMe)_3$ *vs* 1.5-2.0 D for $ZrMe_3(OMe)$ and $ZrMe(OMe)_3$; see Table I], which may reflect the more delocalized negative charge in the Cp ligand. This suggests that Cp-containing precursors may be more volatile than comparable precursors without Cp.

The dipole data show no general effect due to alkyl/alkoxide ligands. However $Zr(MeCp)_2Me_2$ and $Hf(MeCp)_2Me_2$ show a slightly lower dipole moment (1.3 D, Table II) than the alkoxide-containing analogues $Zr(MeCp)_2(Me)(OMe)$ and $Hf(MeCp)_2(Me)(OMe)$ (1.5-1.6 D) and so the former can be expected to be more volatile.

The computations show that the identity of the metal cation has no significant effect on the dipole moment (Table II), and hence on the volatility. It is also found that additional bulk at the Cp ligand (Table II) and at the alkoxide ligand (Table III) has little effect on the dipole moment, as expected for non-polar R groups. However, dipole moment is just one contributor to the intermolecular forces that control volatility. The model agrees with experimental volatility trends for the compounds concerned (5) although it is likely that other non-bonded interactions between alkyl R groups and mass effects have a significant impact on volatility, and these have not been considered in the current calculations of monomers.

3.4 Discussion

The central mechanistic question for heteroleptic complexes such as $Zr(CpMe)_2(Me)(OMe)$ is in what order the ligands will be eliminated during ALD. Our data reveal a clear thermodynamic preference for elimination of ligands in the sequence: 1) Me followed by 2) Cp followed by 3) OMe followed by 4) Cl. The elimination reactions during ALD are in fact governed by the *kinetics* of proton transfer to the ligand at the surface, which has not been computed here, but it is likely that the activation energies for this set of similar reactions follow the same trends as the ΔE_{hyd}.

Taking the example of $Zr(Cp)_2(Me)_2$, the computed energetics suggest that all Me ligands would be eliminated as CH_4 during the ZrL_4 pulse, as well as some elimination of Cp, depending on the availability of surface-OH at a given growth temperature. The predominant intermediate on the surface at the end of this pulse would therefore be surf-$Zr(Cp)_2$ or ZrCp. The remaining Cp would be eliminated during the subsequent O-precursor pulse (H_2O or O_3), and an OH-terminated surface would be regenerated. This accounts well for the results of *in situ* quadruople mass spectrometry on $Zr(Cp)_2(Me)_2$+D_2O ALD at 200-400°C, where 80-90% of the CH_3D and 30-40% of the CpD was found to desorb during the ZrL_4 pulse (8) .

In a similar way, we can predict the mechanism and half-reactions for the ALD of ZrO_2 from $Zr(CpMe)_2(Me)(OMe)$ and H_2O. During the $Zr(CpMe)_2(Me)(OMe)$ pulse, all Me ligands and a proportion of the CpMe ligands will be eliminated, leaving a surface predominantly covered

with a mixture of surf-Zr(CpMe)(OMe) and surf-Zr(OMe). The more CpMe that can be eliminated during the Zr precursor pulse, the higher the ALD growth rate will be. We would expect exactly the same mechanism for the Hf derivative.

One major advantage of $M(CpMe)_2(Me)_2$ over MCp_2Me_2 is that the former is liquid but the latter solid under pressures and temperatures typically used in ALD precursor introduction systems (3, 4, 6). The former also show lower evaporation/sublimation temperatures. We have not attempted to completely compute intermolecular forces for these substances. (Indeed, dispersion interactions are not reliably accounted for in DFT). Simply looking at dipole-dipole interactions, we see that substituting non-polar groups on the Cp ligands has negligible impact in the dipole moments. Clearly, dipole interactions do not determine the phase of these precursors, and dipole moment data are of limited usefulness in predicting precursor volatility in this case.

The other striking difference between $M(CpMe)_2(Me)_2$ and MCp_2Me_2 is the enhanced thermal stability of the former, performing well in self-limiting ALD up to 500°C (4). $ZrCp_2Me_2$ in particular shows a tendency to decompose at elevated temperatures (5). It has been proposed that variations in the strength of M-Cp *vs* M-CpMe bonding may account for this. However, our calculations show no substantial difference in bond strength across the range of CpR ligands. This is consistent with the similar growth rates (0.4-0.6 Å/cycle) and onset temperatures for ALD (ca. 350°C) for experiments using the MCp_2Me_2 and $M(CpMe)_2(Me)_2$ precursors with ozone (3, 6). Given this quantitative similarity between M-Cp and M-(CpMe) bonding, it is apparent that the mechanism for precursor decomposition must be more involved than just M-Cp bond scission.

The calculations revealed no significant difference between Zr and Hf precursors, consistent with the very similar chemistry shown by these elements. Hf precursors showed slightly shorter metal-ligand bonds, identical dipole moments and slightly higher ALD reactivity when compared to the analogous Zr complex. Experimentally however, $HfCp_2Me_2$ has a slightly lower growth rate than the Zr analogue, albeit in different studies (3, 6). More dramatically, thermogravimetric analysis experiments show substantial decomposition of $Zr(CpMe)_2(Me)_2$, but not of $Hf(Cp)_2(Me)_2$ (5). Our calculations provide no hints to explain such a difference in thermal stability between Zr and Hf compounds and further mechanistic

work is ongoing to establish the root cause of the decomposition process for the Zr compound.

Ligand-ligand interaction in most of the complexes computed here seems to be low, as evidenced by the roughly additive ΔE_{hyd} of the Cp-Me-OMe family. Despite their bulk, three Cp ligands in η^5 coordination can be accommodated around a single metal centre (but a fourth Cp shifts to η^1). We therefore recognize that many of these precursors may evaporate as oligomers, with bridging-Cp or bridging-Me, whereas the current calculations have been limited to monomers. Precursor adsorption is likely to be very different for monomers and oligomers. However, this does not affect our conclusions on the inherent reactivity of the different ligands. Overall, we expect that oligomers would be slightly less reactive towards elimination than monomers, but might undergo *in situ* decomposition reactions that generate more reactive species at the surface. Explicit computation of oligomers will therefore be an interesting extension of this work.

3.5 Conclusion

We have carried out DFT calculations on a series of Cp precursors of Zr and Hf in order to evaluate and improve their effectiveness in ALD of the respective oxides. With respect to the rate-determining reaction of ALD (ligand elimination), we find that the Cp complexes are roughly as reactive as amide precursors, and that reactivity can be tuned in a near-linear fashion by introducing methyl or methoxide ligands. Among the heteroleptic precursors, there is a slight energetic preference for those with two Cp ligands [$Zr(Cp)_2(Me)_2$, $Zr(Cp)_2(OMe)_2$] although in actual ALD the precursor $Zr(MeCp)_2(Me)(OMe)$ out performs both these compounds. Adding a bulky R group to Cp was found to have little effect on reactivity or dipole moment.

1. Wilk, G.D., R.M. Wallace, and J.M. Anthony, *High-kappa gate dielectrics: Current status and materials properties considerations.* Journal of Applied Physics, 2001. **89**(10): p. 5243-5275.
2. Suntola, T., *Atomic layer epitaxy.* Materials Science Reports, 1989. **4**(5): p. 261-312.
3. Niinistö, J., et al., *In Situ Quadrupole Mass Spectrometry Study of Atomic-Layer Deposition of ZrO_2 Using $Cp_2Zr(CH_3)_2$ and Water.* Langmuir, 2005. **21**(16): p. 7321-7325.
4. Niinistö, J., et al., *Atomic Layer Deposition of HfO_2 Thin Films Exploiting Novel Cyclopentadienyl Precursors at High Temperatures.* Chemistry of Materials, 2007. **19**(13): p. 3319-3324.
5. Rushworth, Surf. Coat. Tech., 2007.
6. Putkonen, M. and L. Niinisto, *Zirconia thin films by atomic layer epitaxy. A comparative study on the use of novel precursors with ozone.* Journal of Materials Chemistry, 2001. **11**(12): p. 3141-3147.
7. Putkonen, M. and L. Niinistö, *Organometallic Precursors for Atomic Layer Deposition*, in *Precursor Chemistry of Advanced Materials*, R. Fischer, Editor. 2005, Springer Berlin Heidelberg. p. 125-145.
8. Niinisto, J., et al., *Controlled growth of HfO_2 thin films by atomic layer deposition from cyclopentadienyl-type precursor and water.* Journal of Materials Chemistry, 2005. **15**(23): p. 2271-2275.
9. Elliott, S.D., *Predictive process design: a theoretical model of atomic layer deposition.* Computational Materials Science, 2005. **33**(1–3): p. 20-25.
10. Widjaja, Y. and C.B. Musgrave, *Atomic layer deposition of hafnium oxide: A detailed reaction mechanism from first principles.* The Journal of Chemical Physics, 2002. **117**(5): p. 1931-1934.
11. Han, J.H., et al., *A quantum chemical study of ZrO_2 atomic layer deposition growth reactions on the SiO_2 surface.* Surface Science, 2004. **550**(1–3): p. 199-212.
12. Jeloaica, L., et al., *Density functional theory study of $HfCl_4$, $ZrCl_4$, and $Al(CH_3)_3$ decomposition on hydroxylated SiO_2: Initial stage of high-k atomic layer deposition.* Applied Physics Letters, 2003. **83**: p. 542.
13. Kelly, M.J., et al., *In-Situ Infrared Spectroscopy and Density Functional Theory Modeling of Hafnium Alkylamine Adsorption on Si−OH and Si−H Surfaces.* Chemistry of Materials, 2005. **17**(21): p. 5305-5314.
14. Ahlrichs, R., et al., *Electronic structure calculations on workstation computers: The program system turbomole.* Chemical Physics Letters, 1989. **162**(3): p. 165-169.
15. Becke, A.D., *Density-functional exchange-energy approximation with correct asymptotic behavior.* Physical Review A, 1988. **38**(6): p. 3098-3100.
16. Perdew, J.P., *Density-functional approximation for the correlation energy of the inhomogeneous electron gas.* Physical Review B, 1986. **33**(12): p. 8822.
17. Eichkorn, K., et al., *Auxiliary basis sets to approximate Coulomb potentials (Chem. Phys. Letters 240 (1995) 283).* Chemical Physics Letters, 1995. **242**(6): p. 652-660.
18. Eichkorn, K., et al., *Auxiliary basis sets for main row atoms and transition metals and their use to approximate Coulomb potentials.* Theoretical Chemistry Accounts: Theory, Computation, and Modeling (Theoretica Chimica Acta), 1997. **97**(1): p. 119-124.
19. Sierka, M., A. Hogekamp, and R. Ahlrichs, *Fast evaluation of the Coulomb potential for electron densities using multipole accelerated resolution of identity approximation.* The Journal of Chemical Physics, 2003. **118**(20): p. 9136-9148.

20. Schafer, A., H. Horn, and R. Ahlrichs, *Fully optimized contracted Gaussian basis sets for atoms Li to Kr.* The Journal of Chemical Physics, 1992. **97**(4): p. 2571-2577.
21. Andrae, D., et al., *Energy-adjusted ab initio pseudopotentials for the second and third row transition elements.* Theoretical Chemistry Accounts: Theory, Computation, and Modeling (Theoretica Chimica Acta), 1990. **77**(2): p. 123-141.
22. Widjaja, Y. and C.B. Musgrave, *Quantum chemical study of the mechanism of aluminum oxide atomic layer deposition.* Applied Physics Letters, 2002. **80**(18): p. 3304-3306.
23. Delabie, A., et al. *Atomic layer deposition of hafnium silicate gate dielectric layers*. 2007: AVS.

Chapter 4. Mechanism for zirconium oxide atomic layer deposition using bis(methylcyclopentadienyl)methoxymethyl zirconium

This chapter was published in *"Applied Physics Letters"* as:

J. W. Elam, M. J. Pellin, S. D. Elliott, A. Zydor, M. C. Faia, and J. T. Hupp, Appl. Phys. Lett. **91**, 253123 (2007)

Copyright 2007 American Institute of Physics. This article may be downloaded for personal use only. Any other use requires prior permission of the author and the American Institute of Physics.
The following article may be found at http://link.aip.org/link/?apl/91/253123

For this chapter I did the calculations and parts of the analysis related to the calculations. The experimental part was done by Dr. J. W. Elam and collaborators.

The mechanism for zirconium oxide atomic layer deposition using bis(methylcyclopentadienyl)methoxymethyl zirconium and H_2O was examined using *ab initio* calculations of hydrolysis energies to predict the order of ligand loss. These predictions were tested using *in situ* mass spectrometric measurements which revealed that the methyl ligand and 66% of the methylcyclopentadienyl ligands are lost during the zirconium precursor adsorption. The remaining 34% of the methylcyclopentadienyl ligands and the methoxy ligand are lost during the subsequent H_2O exposure. These measurements agree very well with the predictions, demonstrating that thermodynamic calculations are a simple and accurate predictor for the reactivity of these compounds.

Atomic layer deposition (ALD) is a thin film growth method using alternating, self-limiting reactions between gaseous precursors and a solid surface to deposit materials in an atomic layer-by-layer fashion [1]. Zirconium oxide (ZrO_2) is a promising high-dielectric constant replacement for SiO_2 in future microelectronic devices [2], and also has applications in photovoltaics [3] and catalysis [4, 5]. ALD is an attractive method for preparing ZrO_2 thin films because it affords precise thickness control and superb conformality [6-8]. Understanding the ALD mechanism is important because the mechanism affects the growth rate and purity of the films. Additionally, a mechanistic understanding can guide proper precursor selection. In this study, ab initio calculations are performed to predict the order in which the ligands are lost during ZrO_2 ALD. These predictions are tested using in situ quadrupole mass spectrometry (QMS).

We focus on the heteroleptic precursor, bis(methylcyclopentadienyl)methoxymethyl zirconium $Zr(MeCp)_2(Me)(OMe)$, abbreviated ZrL_4, with ligands L = MeCp, Me, and OMe. Heteroleptic precursors facilitate mechanistic studies and allow precursor fine-tuning. The Zr and Hf versions of this precursor are thermally stable to 500°C [9] and produce high quality dielectric films [10]. Using H2O as oxygen source, the expected ALD reaction is:

$$ZrL_4\,(gas) + 2H_2O(gas) \rightarrow ZrO_2\,(solid) + 4HL(gas) \qquad \text{Equation 1}$$

Equation 1 provides no information about the surface-mediated mechanism of growth or about the order of ligand release. This information is relevant because steric hindrance between the ligands remaining after the ZrL_4 pulse will dictate the ALD growth rate [11].

At the start of the ZrL_4 pulse, the growing surface is covered with hydroxyls (surf-OH) that provide protons (H^+). The adsorption of ZrL_4 produces ligands on the surface (L^- = $MeCp^-$, Me^-, and OMe^-), which can combine with protons and desorb as HL. The kinetics of this elimination reaction will be determined by the relative bond strengths[1] of Zr—L vs. H—L at the surface, and by surface properties such as the O—H strength and H^+ diffusion rate. To

[1] Although reaction rates are governed by activation energies rather than bond enthalpies, the relative activation energies are likely to follow the same trends as bond enthalpies in this set of similar reactions.

compare different ligands, it is adequate to compute the different Zr—L vs. H—L bond enthalpies and to ignore effects that are specific to surface geometry [12].

We define the gas-phase Brønsted basicity (BB) of L^- relative to OH^- as:

$$\Delta E_{BB} = \Delta E \text{ for } L^- + H_2O \rightarrow HL + OH^- \qquad \text{Equation 2}$$

The more negative ΔE_{BB}, the stronger the BB of L^- and the stronger the H—L bond. We compute the change in internal energy neglecting entropy/temperature effects. We likewise define the Lewis basicity (LB) of L^- relative to OH^- as:

$$\Delta E_{LB} = ¼.\Delta E \text{ for } 4L^- + Zr(OH)_4 \rightarrow ZrL_4 + 4OH^- \qquad \text{Equation 3}$$

Stronger Lewis bases with strong Zr—L bonding show more negative ΔE_{LB}. Combining these equations, $\Delta E_{hyd} = \Delta E_{BB} - \Delta E_{LB}$ where:

$$\Delta E_{hyd} = ¼\Delta E \text{ for } ZrL_4 + 4H_2O \rightarrow Zr(OH)_4 + 4HL \qquad \text{Equation 4}$$

Negative ΔE_{hyd} corresponds to an exoergic hydrolysis reaction at T = 0 K. ΔE_{hyd} thus reflects the relative strengths of Zr^{4+} and H^+ bonding to L^-, using H_2O and $Zr(OH)_4$ as common reference molecules. Equation 4 is thus a model reaction for HL elimination whenever surf-OH and surf-L are present. The resemblance of Equation 4 to the overall growth reaction with H_2O as precursor (Equation 1) is coincidental, since Equation 1 contains no useful mechanistic information.

The species in Equation 4 were modeled as isolated molecules in vacuum. The ground state electronic wavefunction of each molecule was calculated self-consistently within Kohn-Sham Density Functional Theory (DFT) using TURBOMOLE [13] with the B-P86 functional [14, 15], an atom-centered SV(P) basis set [14, 15], and a 28-electron effective core potential on Zr [16]. All species were closed shell. Unconstrained optimization of the molecular geometry was carried out on the DFT potential energy hypersurface, but a vibrational analysis was not carried out. This method has been applied previously to heteroleptic Zr precursors [17].

Table I. Computed energies (kJ/mol) for ligands in model ALD reactions. The Brønsted basicity ΔE_{BB} is from Equation 2, the Lewis basicity ΔE_{LB} from Equation 3 and the hydrolysis energy $\Delta E_{hyd} = \Delta E_{BB} - \Delta E_{LB}$ from Equation 4. The ligand with the most negative ΔE_{hyd} is predicted to be eliminated first.

Ligand	Elimination product	ΔE_{BB}	ΔE_{LB}	ΔE_{hyd}
Me	CH_4	-46.9	+176.6	-223.5
MeCp	MeCpH	+274.7	+375.1	-100.4
OMe	MeOH	+160.9	+152.5	+8.4

The calculated energetics are shown in Table 1. The computed BB values decrease as MeCp > OMe > Me. The computed LB values are similar for Me and OMe but larger for MeCp. Applying Equation 4, ΔE_{hyd} increases as OMe > MeCp > Me. We therefore predict that Me ligands will be eliminated first during the ZrL_4 pulse, followed by MeCp ligands if there are sufficient surf-OH. The OMe ligands along with some MeCp should be eliminated during the H_2O pulse.

To test these predictions, ZrO_2 ALD was monitored with a quadrupole mass spectrometer [18, 19] (QMS, Stanford Research Systems RGA300) installed in a viscous flow reactor[20] at 350°C using alternating exposures to $Zr(MeCp)_2(Me)(OMe)$ (Epichem) for 3 s and deionized H_2O for 2 s with 5 s purge periods between exposures. The $Zr(MeCp)_2(Me)(OMe)$ was vaporized at 95°C. We verified that these conditions yield self-limiting ZrO_2 growth using ellipsometric analysis of films deposited on silicon.

The top three solid traces in **Fig. 1** present the m/z = 79, m/z = 16, and m/z = 31 QMS signals recorded during ZrO_2 ALD. The dotted lines at the bottom of the figure show the dosing times for the $Zr(MeCp)_2(Me)(OMe)$ and H_2O precursors with a high value designating an exposure to the indicated precursor. The middle portion of the graph between 30-92 s shows 5 ALD cycles in which the $Zr(MeCp)_2(Me)(OMe)$ and H_2O precursors are pulsed sequentially. Between 0-30 s, only the $Zr(MeCp)_2(Me)(OMe)$ precursor is pulsed to measure the background for this compound. Similarly, only the H_2O is pulsed between 92-120 s to evaluate the H_2O background. Note that during the background measurements, both a 2 s

exposure followed by a 5 s exposure are used to maintain the same timing sequence as in the ALD cycles.

During the ZrO_2 ALD cycles, m/z = 31 peaks are only observed during the H_2O exposures and the corresponding background is small (~15%), indicating that the methoxy ligand (-OMe) is released exclusively during the H_2O reaction. Similar results were obtained monitoring m/z = 32 in agreement with the cracking pattern for methanol [21] produced by the reaction of methoxy ligands with the hydroxylated surface.

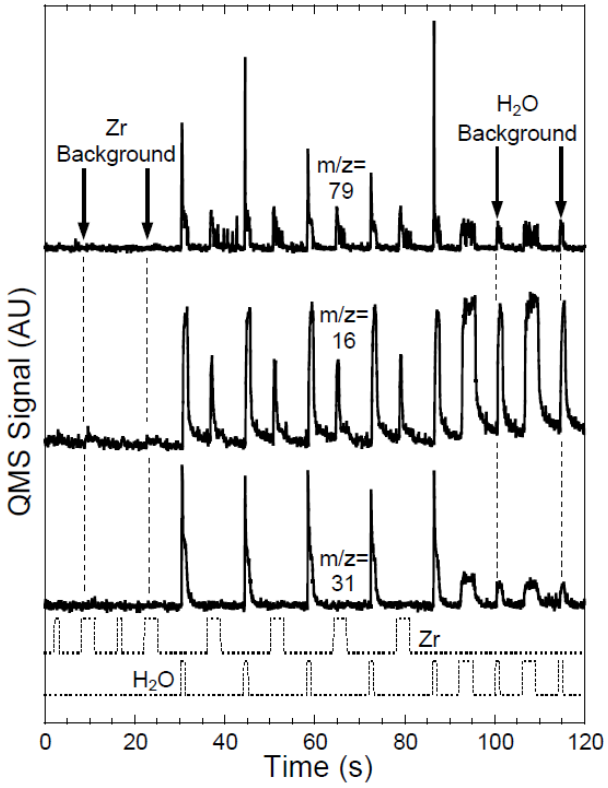


Figure 1. QMS signals for m/z = 31 (MeOH), m/z = 16 (CH_4), and m/z = 79 (MeCpH) measured during ZrO_2 ALD. The $Zr(MeCp)_2(Me)(OMe)$ and H_2O doses are indicated by the dotted lines at the bottom. The $Zr(MeCp)_2(Me)(OMe)$ and H_2O background signals are measured before and after the five, consecutive ZrO_2 ALD cycles as indicated.

The m/z = 16 trace in Figure 1 shows the amount of CH_4 released during the ZrO_2 ALD along with the corresponding background measurements performed as described above. Peaks in the m/z=16 signal are observed when dosing both the $Zr(MeCp)_2(Me)(OMe)$ and H_2O precursors. However, while the $Zr(MeCp)_2(Me)(OMe)$ background is negligible at m/z = 16, the H_2O background and ALD signals are identical within the experimental error.

Consequently, CH_4 is only released during the $Zr(MeCp)_2(Me)(OMe)$ exposures of the ZrO_2 ALD.

The m/z = 79 signals attributed to methylcyclopentadiene (MeCpH) formed during the ZrO_2 ALD in Figure 1 reveal that MeCpH is released during both of the precursor exposures. Similar results were obtained using m/z = 80, and 77 consistent with the cracking pattern for HCpMe [21]. Integration of the m/z = 79 peaks shows that while the $Zr(MeCp)_2(Me)(OMe)$ background is negligible, 44% of the signal observed during the H_2O exposures is background. After background correction, we conclude that 66% of the CpMe ligands are eliminated during the $Zr(MeCp)_2(Me)(OMe)$ exposures, and the remainder are released during the subsequent H_2O exposures. The calculated ΔE_{hyd} = - 100.4 eV suggests that elimination of all CpMe ligands should occur during the metal precursor pulse. However, the ligand elimination pattern will be also determine by different surface effects , e.g. availability of OH groups and steric hindrance [11]. The way that the precursor adsorbs on the surface and which of its ligands are closest to the OH surface groups can also have impact. The gas-phase model does not include those effects.

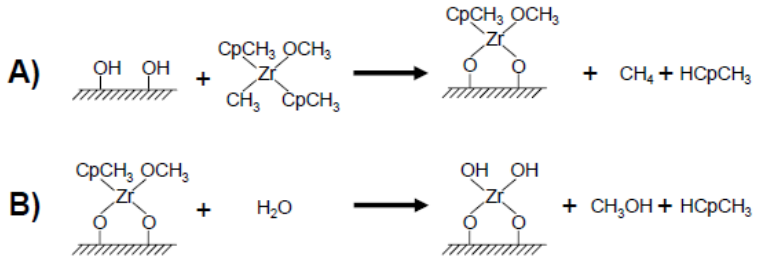


Figure 2. Illustration of proposed ZrO_2 ALD mechanism.

On the base of this simple gas-phase model and measurements we suggest the mechanism for ZrO_2 ALD in Figure 2. In step A, $Zr(MeCp)_2(Me)(OMe)$ reacts with the hydroxylated surface releasing the Me ligand as CH_4 and one or more of the MeCp ligands as MeCpH. This modified surface is exposed to H_2O in step B, liberating any remaining MeCp ligands as MeCpH, and all of the OMe ligands as MeOH. The QMS measurements indicate that, on average, 1.32 MeCp ligands are removed in step A, so that 32% of the $Zr(MeCp)_2(Me)(OMe)$ molecules react with three hydroxyls and release both MeCp ligands in step A.

Following the $Zr(MeCp)_2(Me)(OMe)$ adsorption, the surface is covered with MeCp and OMe in the ratio ~2:3. Consequently, the steric bulk of these ligands will limit the ALD growth

rate. However, because the Me ligand is eliminated before saturation, replacing the Me with a bulkier alkyl group should not affect the growth rate.

The QMS measurements follow the ligand release pattern suggested by the ΔE_{hyd} calculations in Table 1. This agreement lends support to our assertion that a simple comparison of bond strengths captures the essential information for predicting the ALD mechanism. We have also identified the important precursor properties: strong affinity of Me for H^+ of surf-OH, weak bonding of MeCp to Zr, and similar bonding of OMe to Zr and H.

1. Leskelä, M. and M. Ritala, *Atomic layer deposition (ALD): from precursors to thin film structures.* Thin Solid Films, 2002. **409**(1): p. 138-146.
2. Wilk, G.D., R.M. Wallace, and J.M. Anthony, *High-kappa gate dielectrics: Current status and materials properties considerations.* Journal of Applied Physics, 2001. **89**(10): p. 5243-5275.
3. Menzies, D.B., et al., *Modification of mesoporous TiO_2 electrodes by surface treatment with titanium(IV), indium(III) and zirconium(IV) oxide precursors: preparation, characterization and photovoltaic performance in dye-sensitized nanocrystalline solar cells.* Nanotechnology, 2007. **18**(12).
4. Wootsch, A., et al., *Carbon monoxide oxidation over well-defined Pt/ZrO_2 model catalysts: Bridging the material gap.* Applied Surface Science, 2006. **253**(3): p. 1310-1322.
5. Nicholas, C.P. and T.J. Marks, *Zirconium hydrocarbyl chemisorption on sulfated metal oxides: New supports, chemisorption pathways, and implications for catalysis.* Langmuir, 2004. **20**(22): p. 9456-9462.
6. Kukli, K., et al., *Influence of growth temperature on properties of zirconium dioxide films grown by atomic layer deposition.* Journal of Applied Physics, 2002. **92**(4): p. 1833-1840.
7. Kosola, A., et al., *Effect of annealing in processing of strontium titanate thin films by ALD.* Applied Surface Science, 2003. **211**(1–4): p. 102-112.
8. Kukli, K., et al., *Atomic layer deposition of ZrO_2 and HfO_2 on deep trenched and planar silicon.* Microelectronic Engineering, 2007. **84**(9-10): p. 2010-2013.
9. Rushworth, S., et al., *Thermal stability studies for advanced Hafnium and Zirconium ALD precursors.* Surface & Coatings Technology, 2007. **201**(22-23): p. 9060-9065.
10. Niinistö, J., et al., *Atomic Layer Deposition of HfO_2 Thin Films Exploiting Novel Cyclopentadienyl Precursors at High Temperatures.* Chemistry of Materials, 2007. **19**(13): p. 3319-3324.
11. Puurunen, R.L., *Growth per cycle in atomic layer deposition: A theoretical model.* Chemical Vapor Deposition, 2003. **9**(5): p. 249-257.
12. Elliott, S.D., *Improving ALD growth rate via ligand basicity: Quantum chemical calculations on lanthanum precursors.* Surface & Coatings Technology, 2007. **201**(22-23): p. 9076-9081.
13. Ahlrichs, R., et al., *Electronic-Structure Calculations On Workstation Computers - The Program System Turbomole.* Chemical Physics Letters, 1989. **162**(3): p. 165-169.
14. Becke, A.D., *Density-Functional Exchange-Energy Approximation With Correct Asymptotic-Behavior.* Physical Review A, 1988. **38**(6): p. 3098-3100.
15. Perdew, J.P., *Density-Functional Approximation For The Correlation-Energy Of The Inhomogeneous Electron-Gas.* Physical Review B, 1986. **33**(12): p. 8822-8824.
16. Andrae, D., et al., *Energy-Adjusted Abinitio Pseudopotentials For The Second And Third Row Transition-Elements.* Theoretica Chimica Acta, 1990. **77**(2): p. 123-141.
17. Zydor, A., et al., *An ab initio Evaluation of Cyclopentadienyl Precursors for the Atomic Layer Deposition of Hafnia and Zirconia.* Electrochemical Society Transactions, 2007. **11**(7): p. 113-121.
18. Niinisto, J., et al., *In situ quadrupole mass spectrometry study of atomic-layer deposition of ZrO_2 using $Cp_2Zr(CH_3)_2$ and water.* Langmuir, 2005. **21**(16): p. 7321-7325.
19. Rahtu, A. and M. Ritala, *Reaction mechanism studies on the zirconium chloride-water atomic layer deposition process.* Journal of Materials Chemistry, 2002. **12**(5): p. 1484-1489.
20. Elam, J.W., M.D. Groner, and S.M. George, *Viscous Flow Reactor with Quartz Crystal Microbalance for Thin Film Growth by Atomic Layer Deposition.* Reviews of Scientific Instruments, 2002. **73**(8): p. 2981-2987.
21. *Eight Peak Index of Mass Spectra*. Vol. 1. 1991, Cambridge, UK: Mass Spectometry Data Centre, The Royal Society of Chemistry.

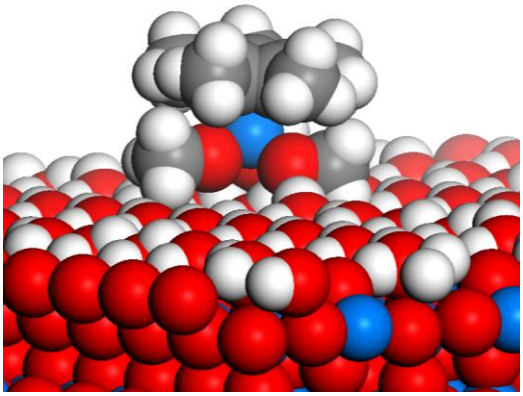
Chapter 5. First principles simulation of reaction steps in the atomic layer deposition of titania: dependence of growth on Lewis acidity of titanocene precursor

The chapter was published in "Physical Chemistry Chemical Physics" as:

Zydor, V. G. Kessler and S. D. Elliott, Phys. Chem. Chem. Phys., 2012, **14**, 7954

The following article may be found at http://dx.doi.org/10.1021/jp9072608

For this chapter I did the calculations, analyses which lead to major conclusions and first draft of the publication. The experimental part was done by Prof Vadim G. Kessler



The precursor [Ti(Cp)(OMe)$_3$] hydrogen-bonds to the hydrated TiO_2 surface, but does not undergo ALD reactions, because Cp* increases steric crowding, reduces electrophilicity and prevents Ti (blue) from coordinating directly to the surface.*

It is a common finding that titanocene-derived precursors do not yield TiO_2 films in atomic layer deposition (ALD) with water. For instance, ALD with $Ti(OMe)_4$ and water gives 0.5 Å/cycle, while $TiCp^*(OMe)_3$ does not show any growth (Me = CH_3, Cp* = $C_5(CH_3)_5$). From mass spectrometry we found that $Ti(OMe)_4$ occurs in the gas phase practically exclusively as a monomer. We then used first principles density functional theory (DFT) to model the ALD reaction sequence and find the reason for the difference in growth behaviour. Both precursors adsorb initially via hydrogen-bonding. The simulations reveal that the Cp* ligand of $TiCp^*(OMe)_3$ lowers the Lewis acidity of the Ti centre and prevents its coordination to surface O ('densification') during both of the ALD pulses. The effect of Cp* on Ti seems to be both steric (full coordination sphere) and electronic (lower electrophilicity). This crucial step in the sequence of ALD reactions is therefore not possible in the case of $TiCp^*(OMe)_3 + H_2O$, which means that there is no deposition of TiO_2 films.

5.1 Introduction

5.1.1 Thin film deposition of titania

Atomic layer deposition (ALD) is a highly-controllable, uniform deposition technique based on alternating reactions of gas-phase precursors with a surface [1-4]. Due to the self-limiting nature of the reaction each phase deposits only a single atomic monolayer and the characteristics of the thin-film can be adjusted via the deposition conditions (pressure, temperature) and the number of deposition cycles. The ALD process is additionally highly conformal, making it overall a widely-used choice for the deposition of ultra-thin, precise-thickness films over topographically-patterned surfaces. Of the materials that can be deposited by ALD, TiO_2 is highly desirable for the variety of applications in which it is used as a thin film [5], such as photocatalysis [6-10] self-cleaning surfaces [11-13] and as a component of high-*k* [14] and ferroelectric materials (*e.g.* strontium titanate) [15]. Despite the breadth of research into TiO_2 ALD, however, details about the mechanistic reaction of the titanium precursors with the surface are still not well understood. Using computational chemistry techniques, these interactions may be modeled and the underlying reaction mechanisms better understood, so as to improve the deposition process.

It is reported [16] that 'molecular layering' of TiO_2 from $TiCl_4$ + H_2O was described by Aleskovskii and co-workers already in 1965. However, Cl-containing precursors and by-products are corrosive and, in some cases, involatile (*e.g.* $SrCl_2$). Amides and alkoxides of Ti do not have these disadvantages in ALD, but undergo relatively facile thermal decomposition. The most stable of these, $Ti(OMe)_4$, where Me = CH_3, shows ALD growth rates with H_2O of 0.4-0.6 Å/cycle up to 300°C, but steadily higher rates above this temperature due to decomposition [17]. $Ti(OMe)_4$ is a tetramer in the solid phase but evaporates predominantly as a monomer [18]. Ti_2-containing aggregates have been reported from mass spectrometry of the vapor, but without quantifying their intensity or identifying their origin. In this paper we carry out a detailed analysis of the evaporation process of $Ti(OMe)_4$ via mass spectrometry, so as to determine whether this precursor reacts as a monomer in ALD (section 5.2).

The poor thermal stability of amides and alkoxides means that there is a need for halide-free Ti precursors that are stable at elevated temperatures but that are also reactive with H_2O in thermal ALD to produce TiO_2 or titanates. The cyclopentadienyl ligand (C_5H_5, Cp) and derivatives such as the pentamethylcyclopentadienyl ligand (C_5Me_5, Cp*) form stable, volatile complexes with many metals and so have been investigated as metal precursors for ALD, finding particular utility for depositing pure films at high temperatures. Cp-based ligands are large: from quantum chemical calculations we estimate a van der Waals diameter of 0.86 nm and an area of 0.58 nm^2 for the Cp ring when complexed [19]. Therefore, only one Cp* or two Cp ligands can be accommodated around the Ti^{4+} cation, along with other, smaller ligands. Thus, ZrO_2 and HfO_2 have been deposited from H_2O and $ZrCp_2Me_2$ [20], $HfCp_2Me_2$ [21], $Zr(MeCp)_2(OMe)Me$ and $Hf(MeCp)_2(OMe)Me$ [22] and complexes with bridged Cp_2 ligands [23]. Mass spectrometry [24] and density functional calculations [25] have shed light on how the various ligands react and also on why $TiCp_2Me_2$ is too unstable to be isolated [26]. The mono-Cp 'piano-stool' complexes $Zr(Cp)(NMe_2)_3$ [27] and $Hf(Cp)(NMe_2)_3$ [28] appear to be less reactive in ALD, yielding good films with ozone rather than H_2O as co-reagent.

Cp-containing Ti complexes have therefore been investigated as high-temperature ALD precursors. Experiments show that the Cp-containing Ti precursor $TiCp^*(OMe)_3$ does not yield TiO_2 films in thermal ALD with water [29], although it does produce TiO_2 or titanates with oxygen plasma [15, 30]. This is in stark contrast to the successful $Ti(OMe)_4 + H_2O$ process, which differs by just one ligand [17]. The aim of this work is to explain this difference. There has been relatively little work to date on the first principles simulation of TiO_2 ALD compared to that of ZrO_2 and HfO_2. Hu and Turner used a cluster models to investigate the initial steps of ALD from $TiCl_4 + H_2O$ [31] and $TiI_4 + H_2O$ [32]. For amidotitanium precursors, Haran *et al.* have investigated adsorption onto self-assembled monolayers [33] and Rodríguez-Reyes *et al.* have computed decomposition reactions on silicon [34]. Terranova *et al.* [35] and Mäkinen *et al.* [36] have computed the reactivity of a TiO_2-anatase substrate towards alumina ALD. The mechanistic steps that we propose come from our first principles study of the mechanistic steps in the ALD of alumina [37] and our extension of this to rare earth oxides, seeing the effect of surface geometry and intrinsic acidity [38]. Preliminary results were published in Ref. [39].

5.1.2 ALD mechanism

In ideal ALD, precursors react only on the growing surface and not in the gas-phase. The film growth reactions of TiO_2 from a Ti-precursor with ligands L (here, L = Cp* or L = OMe) may therefore be written:

$$TiL_{4\,(g)} \leftrightarrows \text{surf-}(TiL_4) \leftrightarrows \text{surf-}(O_xTiL_{4-x}) \leftrightarrows \text{bulk-}TiO_2, \qquad \text{Equation 1}$$

The position of the equilibria between the steps in Equation 1 depends on the reaction energetics and on the availability of reagents during the pulse-purge cycle of ALD. The first step is molecular adsorption. The second step shows the nature of adsorption changing as ligands are eliminated. Ligands are progressively eliminated from the surface (during both Ti and O pulses) and, instead, surface oxygen progressively satisfies Ti coordination, so that $0 \leq x \leq 4$. However, $x = 4$ is not the maximum number of oxygen atoms to which Ti can coordinate; 'bulk-TiO_2' indicates a coordination environment for Ti like that in the interior of the as-deposited thin film, *e.g.* 6-coordinate Ti in amorphous TiO_2. This 'bulk' status may not be reached until after many ALD cycles.

In a general sense, the whole sequence in Equation 1 is the reactive adsorption of a precursor onto the surface. Describing the ALD reaction mechanism means describing each of the steps in Equation 1 and, in particular, describing the various interactions between ML_x adsorbates and the substrate or growing surface.

'Ligand exchange' is one class of reaction that coordination complexes can undergo. For instance, in chemical vapor deposition, metal complexes can exchange ligands with other gas-phase reagents, *e.g.* $TiCl_{4\,(g)} + NH_{3\,(g)} \rightarrow TiCl_3(NH_2)_{\,(g)} + HCl_{\,(g)}$ [40]. The overall reaction shows one ligand being replaced with another, preserving the coordination number of the metal. However the underlying mechanism is more complex [41], consisting of association of the new ligand and increase in coordination number [*e.g.* $TiCl_4(NH_3)$], rearrangement within this complex to give a ligand adduct [$TiCl_3(HCl)(NH_2)$] and dissociation of the adduct, lowering the coordination number. This reaction is therefore controlled by the electrophilicity of the metal, the nucleophilicities of the ligands and the relative sizes of metal and ligands [41]. Analogous 'ligand exchange' reactions are postulated when metal

complexes react with surfaces, as in ALD [42]. The overall effect in ALD may be the exchange of one ligand for another, or for a surface atom, but the underlying mechanism is likely to include similar association and dissociation steps that depend on the electronic and steric properties of the metal centre, ligands and surface. Therefore, these are the factors that we probe in the current paper for the thermal ALD of TiO_2 from $Ti(Cp^*)(OMe)_3 + H_2O$ in comparison with $Ti(OMe)_4 + H_2O$.

A well-behaved and well-characterised ALD process is that of Al_2O_3 from trimethylaluminium ($AlMe_3$, TMA) and H_2O. TMA reacts with hydroxylated surfaces to form a new O-Al bond at the surface and release methane [43]. Therefore, in the ALD process, the half-reaction for the TMA pulse shows Me_2Al-Me being replaced by Me_2Al-O_{surf}, while in the H_2O pulse, Al_{surf}-Me is replaced by Al_{surf}-OH [44, 45], *i.e.* 'ligand exchange'. Atomic-scale cluster calculations [46] have revealed the individual steps behind the half reactions, namely chemisorption of each molecular precursor to form a Lewis adduct (Al-O bonds), followed by transfer of successive protons to methyl groups and desorption of methane. Calculations with a more realistic surface model [37] showed that the ligand elimination steps are accompanied by an increase in the coordination number of Al and diffusion to bulk-like sites. In this paper, we will examine whether these mechanistic ideas from TMA + H_2O can explain the ALD experiments with cyclopentadienyl Ti precursors.

We therefore use first principles density functional theory (DFT) to examine the mechanistic steps of adsorption, elimination and densification of $TiCp^*(OMe)_3$ *versus* $Ti(OMe)_4$ in Equation 1. The computations start from the assumption that the water step has finished, leaving a hydrated surface. We generate atomic geometries so as to consider the following steps, which may be distinct steps separated by energy barriers, or may happen in tandem with one another, and are repeated depending on the availability of precursors, adsorption sites, ligands and protons:

(i) adsorption of the precursor molecule at the surface;
(ii) coordination of metal atom to the surface;
(iii) proton transfer to ligand to form adduct;
(iv) elimination of ligand adduct by desorption;
(v) further coordination of metal atom to surface oxygen.

Steps (ii) and (v) are examples of 'densification', by which the coordination number of newly-deposited metal and oxygen atoms increases towards that of the bulk material [47, 48]. Desorption [step (iv)] causes the coordination number of the metal cation to decrease.

5.2 Mass spectrometric experiment

To understand the mechanism, it is important to know the chemical structure of the gas-phase precursor that impinges upon the surface during ALD, in particular as an input to molecular modelling. The structure and chemistry of titanium methoxide has been investigated by Write and Williams[18], who have found this compound to be a tetramer in the solid phase. The mass-spectrometry data were used to evaluate aggregation in the gas phase and indicated the monomer to be mostly present in the gas phase with highest observed mass at m/z = 142, corresponding to the loss of the OCH_3 ligand (or, actually, OCH_2) from the molecular $Ti(OCH_3)_4$ unit, m = 172. The presence of aggregates in the gas phase could not be ruled out but the intensity for the peaks supposed to correspond to these species was comparable with the background. There were indications that fragments such as $Ti_2(OCH_3)_6^+$ and $Ti_2O(OCH_3)_5^+$ were observed in the mass spectrum, however, without indication of their intensity and identification of what fraction of the total gas phase composition they can constitute. These are the questions to be resolved in this section of the paper.

5.2.1 Method for mass spectrometry

Titanium methoxide was received from Aldrich (cat. no. 463582) and handled in dry nitrogen atmosphere using a glove box. The product was used as received without any further purification. The evaporation and mass-spectral study was carried out with JEOL JMS-SX/SX102A (JEOL, Japan) tandem mass spectrometer, operating at an accelerating voltage of 10 kV. Electron ionization (EI) mass spectra (with scan range of m/z 500-1500) were recorded using a direct probe with evaporation of the samples into the ion source kept at *ca.* 200ºC and an electron beam energy of 70 eV. Analysis of the evaporation process was carried out exploiting the methodology reported earlier [49], based on analysis of the correlation between the total ion current profile and the profile of ions, originating from gas phase species with well-established composition.

5.2.2 Experimental results from mass spectroscopy

The majority of peaks in the mass-spectrum of titanium methoxide belong clearly to the fragmentation tree of the $Ti(OCH_3)_4$ monomer. In fact, in contrast to Write and Williams[18], we were able to observe the molecular ion at m/z = 172 and the ion resulting from the loss of a hydrogen atom from it at m/z = 171 showing relatively high intensity (Figure 1). Further fragmentation follows the pathways typical for metal alkoxides with the loss of either an alkoxide ligand, OCH_3, or a dialkyl ether molecule CH_3OCH_3. A pathway specific for a methoxide is the loss of a formaldehyde molecule, CH_2O.

It is interesting to note the presence of the ion with m/z = 185 (7.5% intensity) originating apparently from a minor admixture of $Ti(OCH_3)_3(OC_2H_5)$ and indicating that the industrial product is obtained most probably through alcohol interchange from the cheaper and readily-available titanium ethoxide. It is even worth noting that the fragments corresponding to further fragmentation of these species are not observed in the spectrum, demonstrating that this admixture is truly minor and is visible just due to its relatively high stability and volatility.

The only ion corresponding to aggregated species observable in the mass-spectra was $Ti_2O(OCH_3)_5^+$, m/z = 267, with truly low intensity (below 0.5%). The ion currents for m/z = 171 and 185 both reveal high correlation with the total ion current, indicating that the evaporation of titanium methoxide occurs almost solely in the form of monomeric species. The non-Gaussian shape of the ion current profile indicates the possibility of a thermolytic process in the solid phase on evaporation. It can be hypothesised that the presence of a minor amount of oxo-substituted dinuclear species $Ti_2O(OCH_3)_6$, revealed by the traces of $Ti_2O(OCH_3)_5^+$ ions in the fragmentation pattern, is originating from the decomposition in the solid phase and, thus, is not testifying to any possibility of chemically congruent transfer of the molecular aggregates of titanium methoxide into the gas phase.

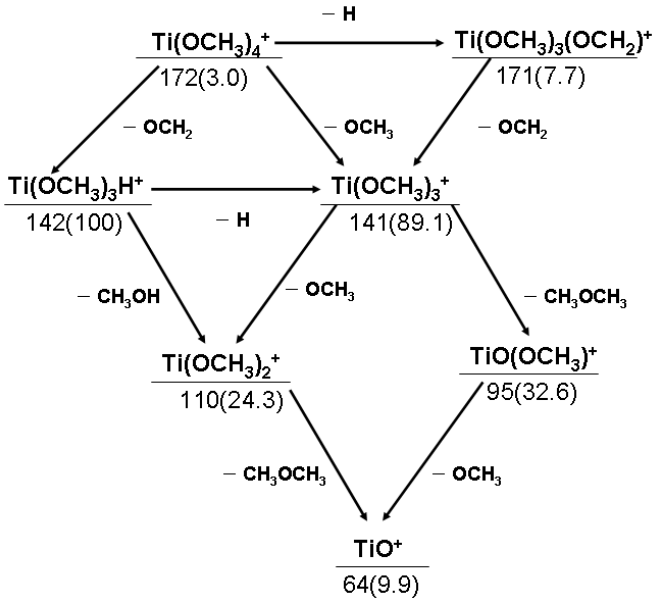


Figure 1: Fragmentation pattern of $Ti(OCH_3)_4$ with numbers indicating m/z and percentage intensity in parentheses.

5.3 First principles study of mechanism

5.3.1 Computational method

We use periodic density functional theory (DFT) as implemented in the VASP code (version 4.6)[50, 51], with the Projected Augmented Wave description of cores [52, 53] and the Perdew Burke Ernzerhof functional [54], which has been found to yield H-bonding energetics accurate to $\pm$ 0.1 eV [55, 56]. The valence electron basis is a set of plane waves with a kinetic energy cutoff of 396 eV. For the bulk oxides, *k*-point sampling is performed with a 4 × 4 × 6 Monkhorst–Pack sampling grid. As a model for TiO_2 we use the rutile crystal structure and as a model for the surface of the growing film we use the most stable bare face, (1 1 0). Appropriate *k*-point sampling is employed: 4 × 4 × 1, 2 × 2 × 1, 1 × 2 × 1 and Γ-point grids for the (1 × 1), (2 × 2), (4 × 2) and (4 × 4) surface expansions of the cell, respectively. The bulk lattice constants are determined using the Murnaghan equation of state [57]. The geometries of the precursor and product molecules $Ti(OMe)_4$, $TiCp^*(OMe)_3$, Cp*H, MeOH and H_2O are individually relaxed in a box of dimensions 20 × 20 × 20 Å, with a 396 eV cutoff energy and Γ-point sampling. Based on mass spectrometry (section 5.2), monomeric $Ti(OMe)_4$ is used as the model for the gas-phase species. Computed energy

changes at T = -273.15 °C are quoted and the contribution of entropy to the free energy at higher temperatures is not included. In all cases we expect that entropy will cause the gas-phase species to be favoured over adsorbates, as previously computed [37], but this will have no bearing on our study of precursor-surface bonding.

5.3.2 Results for ligand basicity and 'ligand exchange'

We can use the computed first principles energies to compare the theoretical reactivity of $TiCp^*(OMe)_3$ and $Ti(OMe)_4$ with respect to the standard ALD reaction for oxides with H_2O.

$$TiCp^*(OMe)_{3\,(g)} + 2H_2O_{\,(g)} \rightarrow TiO_{2\,(s)} + HCp^*_{\,(g)} + 3MeOH_{\,(g)} \qquad \text{Equation 2}$$

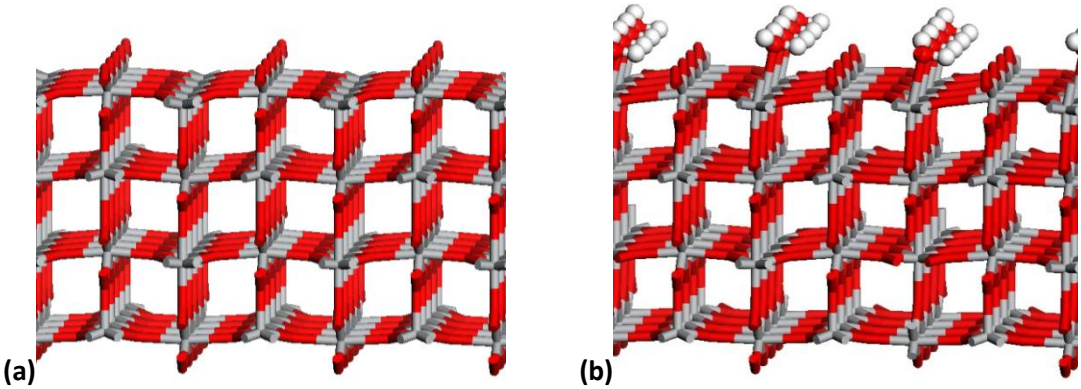


Figure 2: Atomic structure of four trilayer-deep slab of rutile TiO_2 showing a) bare (1 1 0) surface cell expansion (4 x 2) (b) hydrated surface with eight H_2O per cell (colour online: light grey = Ti, red = O, white = H, dark grey = C; sticks = rutile substrate, balls = adsorbates).

The computed energy at T = -273.15 °C of Equation 2 is ΔE = –26.79 eV, which compares with ΔE = –26.71 eV for $Ti(OMe)_4$. This shows that the $[Cp^*]^-$ ligand is more Brønsted basic than $[OMe]^-$ by 0.08 eV, *i.e.* slightly more reactive towards H^+. (Estimating the entropy change in Equation 2 would reveal the free energy change at typical ALD temperatures, but would obscure the difference in Bronsted basicity). 'Ligand exchange' should therefore be slightly more favoured in Cp* than in OMe. The experimental result is in apparent contradiction of this thermodynamic driving force, since ALD does not proceed for $TiCp^*(OMe)_3 + H_2O$ but does for $Ti(OMe)_4 + H_2O$. Therefore, rather than overall energetics, we must consider the detailed reaction mechanism at the surface (Equation 1) and the associated kinetics, which is the subject of the next sections. Our interest is in whether

there are energetic barriers particular to $TiCp^*(OMe)_3$ during the initial steps of its reaction with the surface.

5.3.3 Surface models of bare and hydrated titanium oxide

Bulk TiO_2 is most stable in the tetragonal rutile structure, with six atoms per primitive unit cell. The computed lattice constants are a = 4.6625 Å, c = 2.9700 Å, which are in good agreement with experiment (a = 4.5845 Å, c = 2.9533 Å). A slab was constructed for the rutile (1 1 0) surface and properties were found to converge at a slab thickness of four trilayers (*e.g.* surface energy of the bare surface converged to 0.40 $\pm$ 0.01 Jm^{-2}), consistent with previous calculations [58].

Because of the limits of computation time, the minimum vacuum thickness was usually employed: 10 Å between adjacent bare slabs, which generally meant > 5 Å between the bottommost O's of one slab and the topmost adsorbate H's of the next slab. The bottom face was kept bare (*i.e.* unhydrated) so as to avoid spurious H-bonding interactions. Some spurious van der Waals interaction can however be expected. Our tests show that the resulting adsorption energies are converged to $\pm$ 0.1 eV with respect to vacuum thickness. These tests also show that a larger vacuum (13 Å) is necessary for this level of accuracy when adsorbates are so large and weakly-adsorbed that they approach within 3 Å of the next slab (Figure 3b and Figure 6b).

In constructing the hydroxylated surface, we have to determine physically reasonable hydroxylation coverages. The (4 × 2) surface cell can accommodate eight water molecules and this is computed to be the most energetically favourable coverage at T = -273.15 °C. The adsorption energy of -0.8 eV/H_2O indicates quite strong chemisorption, similar to molecular adsorption on smooth surfaces of TiO_2-anatase [59]. We find that the water molecules are preferentially adsorbed molecularly (Figure 2b), in agreement with other studies on rutile (1 1 0) and other smooth TiO_2 surfaces such as anatase (1 0 1) [35]. We therefore refer to this as the 'hydrated' surface. However it is worth mentioning that the water monolayer dissociates gradually with temperature [60], which is consistent with the gas-phase entropy (1.1 eV/H_2O at T = 275 °C) being greater than the average chemisorption energy. We expect both molecular hydration and dissociative hydroxylation to occur on the rougher

surface[35] that probably exists during ALD growth, but determining such a realistic structure is beyond our current scope. We therefore use this model of a hydrated surface for our calculations of Ti-precursor adsorption.

For these computations, the adsorption energy of the precursor is computed from:

$$E_{ads} = [E(ads) + E(prod)] - [E(prec) + E(surf)], \quad \text{Equation 3}$$

where E(ads) is the total DFT energy (at T = -273.15 °C) of the slab containing the precursor (or precursor fragment) adsorbed on the surface, E(prec) and E(prod) are the total DFT energies of gas phase precursor and by-products respectively in a large cell, and E(surf) is the total DFT energy of the hydrated surface slab prior to adsorption, all geometries fully relaxed within the fixed simulation cell. Note that we include reactive adsorption, *e.g.* where ligands from the precursor react with surface protons and a by-product such as MeOH is eliminated, and in these cases E_{ads} is the sum of reaction energies for molecular adsorption and elimination.

5.3.4 Results for precursor adsorption onto hydrated surfaces

Figure 3 presents the relaxed structures computed for $TiCp^*(OMe)_3$ and $Ti(OMe)_4$ adsorbed at the hydrated (1 1 0) surface of titanium oxide [step (i) of the ALD mechanism]. As starting structures, each precursor monomer was placed above the H_2O-terminated surface and all ions were fully relaxed. A number of other adsorption geometries were tested, but the ones discussed in this section were found to be the most stable.

Upon molecular adsorption of $TiCp^*(OMe)_3$ at the hydrated TiO_2 surface, the energy gain at T = -273.15 °C is -0.4 eV when oriented via OMe (Figure 3a). In the case of $Ti(OMe)_4$ the energy gain is slightly greater, -0.5 eV (Figure 3b). The attraction of the precursors to the hydrated surface via OMe is due to hydrogen bonding between H of surface-bound water and O of precursor methoxy groups (typical H-O distances 1.6 Å). The adsorption energies are plotted in Figure 4.

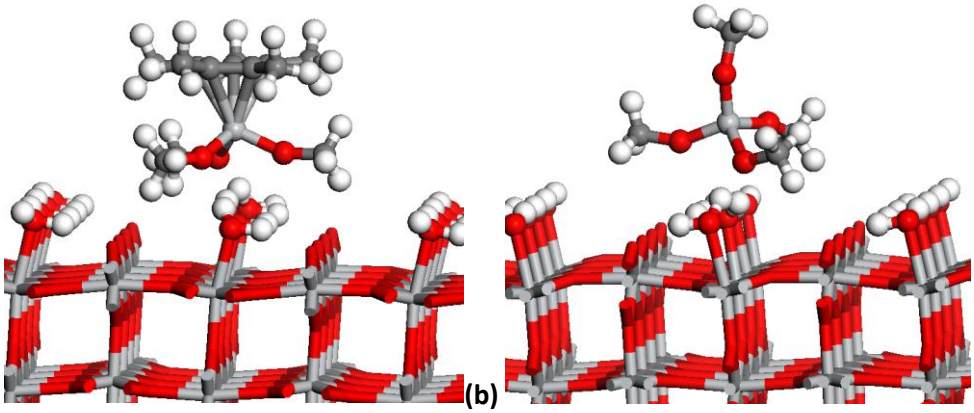
(a)  (b)

Figure 3: Molecular adsorption of (a) $TiCp^*(OMe)_3$ via OMe, (see Figure 6 for adsorption via Cp*) and (b) $Ti(OMe)_4$ at the hydrated (1 1 0) surface of TiO_2 with thicker vacuum. The computed adsorption energies are (a) E_{ads} = -0.4 eV and (b) E_{ads} = -0.5 eV.

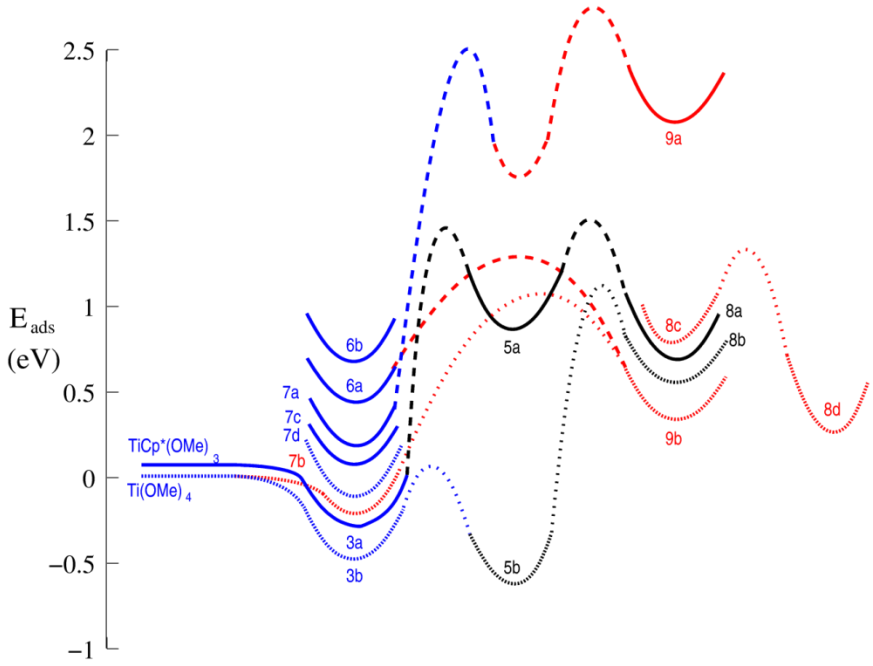


Figure 4: Computed potential energy curves for adsorption of $TiCp^*(OMe)_3$ (solid minima) and $Ti(OMe)_4$ (shaded minima) onto titania surfaces at T = -273.15 °C, followed by H-transfer and desorption of MeOH or Cp*H (each step being separated on the x-axis). Labels are for the figures depicting the structures. Colour online shows the mode of adsorption: molecular via H-bonding (blue), chemisorbed Ti at non-bulk position (black) and chemisorbed Ti at bulk position (red). The +0.08 eV offset of the Cp* curves relative to OMe accounts for the computed difference in overall ΔE. The expected pathways are 3a→5a→8a, 3b→5b→8b, 7a→9a, 7b→9b and 6a→9b.

During the relaxation we do not observe spontaneous H transfer from the H_2O-terminated surface to the precursor, which indicates that there is an energetic barrier towards H transfer. To investigate Ti precursor coordination to surface O [step (ii)], H-transfer [step (iii)] and ligand elimination [step (iv)], hydrogen atoms from the hydrated surface were moved 'by hand' towards OMe ligands and the geometry was then relaxed. This assures that the precursor can adsorb onto a 2-coordinated O at the surface (actually, Ti-OH). In this way, the Brønsted product MeOH is formed, but we find that it remains associated with Ti and does not desorb spontaneously. The resulting structure for $Ti(OMe)_4$ is shown in Figure 5b: the ligands (including MeOH bound loosely to Ti) have distorted away from the surface so as to allow the adsorbing Ti atom to coordinate to surface O (Ti-O distance =1.81 Å). Ti-O coordination is step (ii) of the oxide ALD mechanism proposed above. The overall adsorption energy of all steps leading to this geometry is E_{ads} = -0.6 eV, neglecting entropy. Relative to initial adsorption (Figure 3b) the energy is -0.1 eV, indicating that the ALD reactions of $Ti(OMe)_4$ form a thermodynamically favourable sequence (Figure 4).

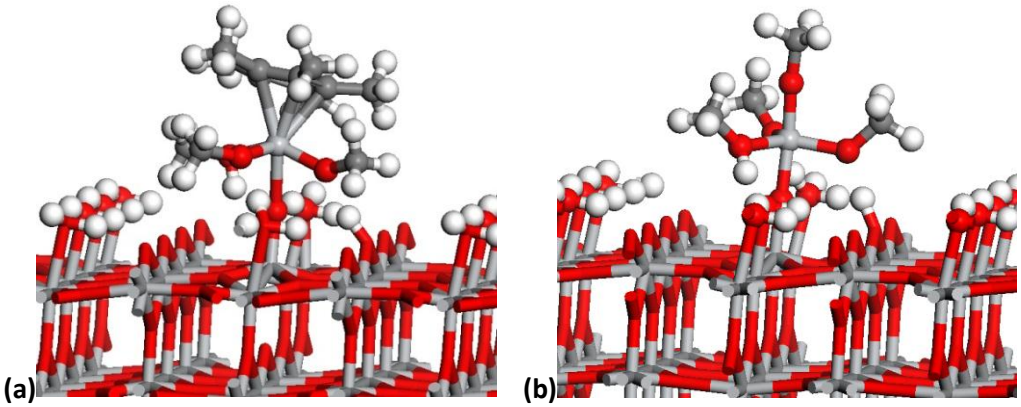


Figure 5: Reactive adsorption and H-transfer at the hydrated surface of TiO_2 for the precursors (a) $TiCp^*(OMe)_3$, E_{ads} = +0.8 eV, and (b) $Ti(OMe)_4$, E_{ads} = -0.6 eV. Hydrogen from the surface is moved 'by hand' towards an OMe ligand and the structure is relaxed.

An analogous adsorption structure for $TiCp^*(OMe)_3$ was tested and optimized. It was difficult to accommodate the molecule on the hydrated surface. This appears to be due to the bulky Cp* ligand, which hinders the distortion of MeO/MeOH ligands away from the surface and thus hinders the association of Ti to surface oxygen [step (ii)]. Figure 5a shows the lowest-energy optimized geometry out of many trials, with a relaxed Ti-O distance of

2.26 Å. It is possible that still more structures have to be tested to find the actual lowest energy. In all of our trials, the computed adsorption energy was consistently found to be positive, which indicates a thermodynamic barrier against chemisorption after H-transfer, even at T = -273.15 °C. For instance, the calculated adsorption energy for the geometry in Figure 5a relative to the hydrated surface is E_{ads} = +0.8 eV which is unstable relative to desorption and significantly higher than that obtained for $Ti(OMe)_4$.

Having examined H-transfer to OMe, we then investigated adsorption geometries that could lead to H-transfer to Cp* and production of HCp*. We could not find any thermodynamically favourable adsorption route via Cp*, as illustrated by the two examples in Figure 6. In fact, even the lowest energy structure obtained (Figure 6a) shows endothermic adsorption that suggests substantial strain and repulsion. This becomes worse when the precursor is angled in an attempt to open up access to precursor-Ti from surface oxygen (Figure 6b). In this orientation, adsorption [step (i)] is unfavoured and neither Ti-O bonding [step (ii)] nor H-transfer [step (iii)] can occur.

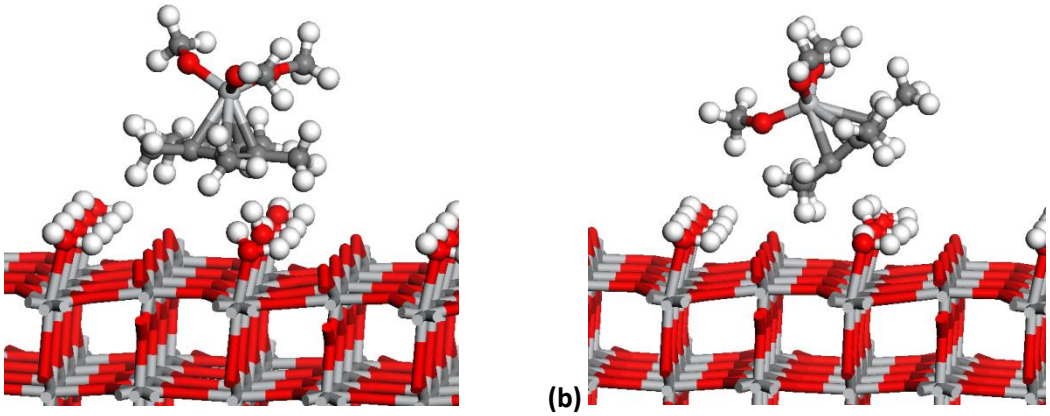


Figure 6: Optimized geometries showing the interaction of Cp* group of $TiCp^*(OMe)_3$ with the hydrated surface of TiO_2: (a) E_{ads} = +0.4 eV, (b) E_{ads} = +0.3 eV. Adsorption via OMe is more stable (Figure 3). 3 Å thicker vacuum is used so as to converge the adsorption energy in (b).

The other possible coordination site for adsorbing Ti on the rutile surface is bridging oxygen, which is the expected location of the next Ti in the rutile structure. The computed structures (prior to H-transfer) are presented in Figure 7. In the case of $TiCp^*(OMe)_3$ it was found to be impossible to coordinate Ti to the bridging oxygen. While relaxing the structure the precursor moved away from the hydrated surface to a shallow minimum at E_{ads} = +0.1 eV

and a Ti-O distance of 3.9 Å (Figure 7a). For $Ti(OMe)_4$ it was much easier to form a bond with bridging oxygen (Figure 7b). Here, OMe ligands are flexible and have room in the ligand sphere to move away from the surface and let Ti coordinate to surface oxygen [step (ii)]. The adsorption energy on the hydrated surface is E_{ads} = -0.2 eV. Like the H-bonded adsorbate (see above), this structure is likely to have a sufficiently long lifetime on the surface to allow H-transfer and ligand elimination to take place, while $TiCp^*(OMe)_3$ is so weakly adsorbed to bridging oxygen that such subsequent reactions are probably not possible.

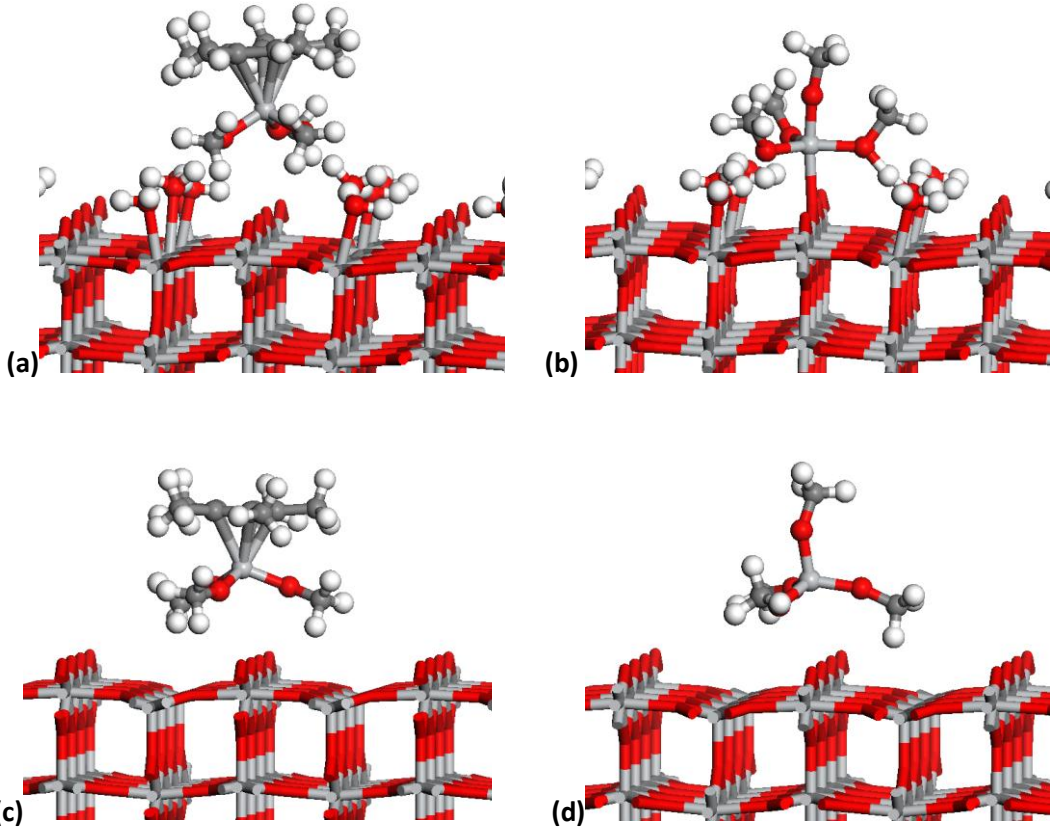


Figure 7: Adsorption at bridging oxygen of the (1 1 0) surface of TiO_2 of (a) $TiCp^*(OMe)_3$ onto hydrated surface, E_{ads} = +0.1 eV, (b) $Ti(OMe)_4$ onto hydrated surface, E_{ads} = -0.2 eV, (c) $TiCp^*(OMe)_3$ onto bare surface, E_{ads} = +0.02 eV, and (d) $Ti(OMe)_4$ onto bare surface, E_{ads} = -0.1 eV.

To check whether this effect is due to crowding with the adsorbed water of the hydrated surface, we have checked adsorption onto the bare TiO_2 surface, where bridging-O atoms are more prominent. This corresponds to the realistic situation of adsorption onto portions

of the surface that are much less hydrated. Crowding does appear to be relieved in the Cp* case, with E_{ads} = +0.02 eV for TiCp*$(OMe)_3$ (Figure 7c), while the absence of H-bonding makes adsorption less favourable for the homoleptic alkoxide [E_{ads} = -0.1 eV for $Ti(OMe)_4$ (Figure 7d)].

5.3.5 Results for elimination of ligands and densification

Step (iv) is the elimination of ligand adducts by desorption, which can be expected to relieve steric hindrance within the ligand sphere. We have seen above that H-transfer to the MeO ligand is more likely than H-transfer to Cp*, and in this section the reaction steps following desorption of MeOH are investigated.

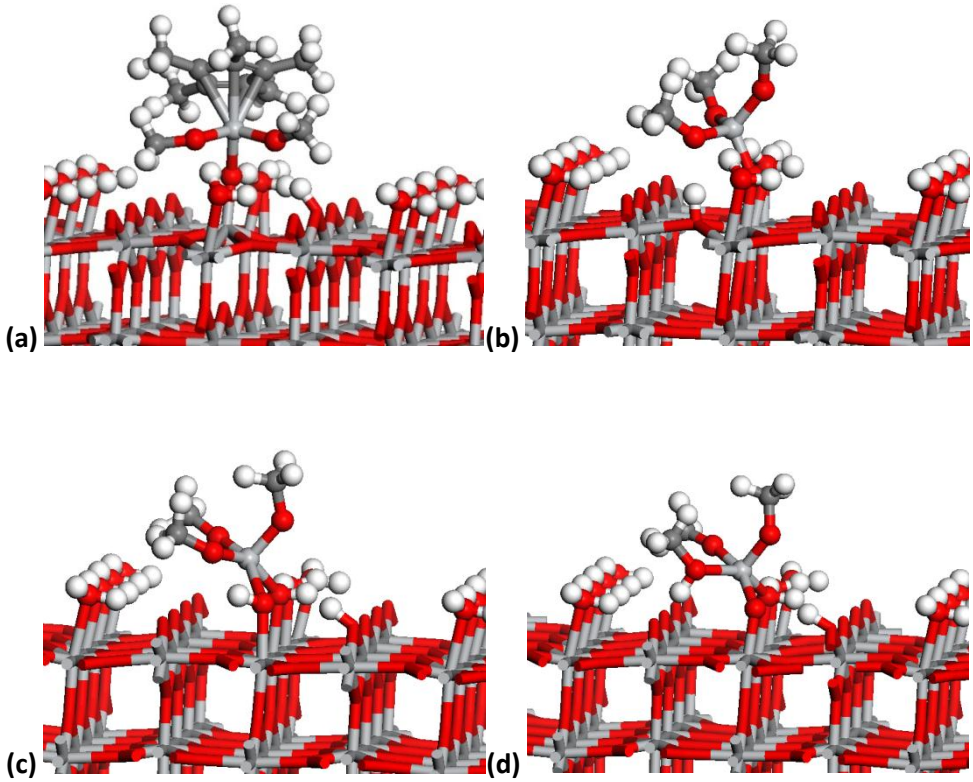


Figure 8: Adsorbate structures after desorption of one MeOH unit from the structures in Figure 5, bonding to O that originated from hydration of surface: (a) surf-O-Ti(Cp*)$(OMe)_2$, E_{ads} = +0.6 eV, (b) surf-O-Ti(OMe)3, E_{ads} = +0.6 eV, (c) surf-O_2-Ti$(OMe)_3$, E_{ads} = +0.8 eV, followed by H-transfer to give (d) surf-O_2-Ti$(OMe)_2$(MeOH), E_{ads} = +0.3 eV.

As can be seen in Figure 8a, elimination of one MeOH relieves steric hindrance within the Cp*-containing precursor fragment and allows Ti of the adsorbate to approach 0.3 Å closer to the surface oxygen (optimized Ti-O = 1.95 Å), although still not as close as the non-Cp* fragment (1.81 Å, Figure 8b). Some residual strain in the Cp* fragment may be evident in the distortion of surface Ti bound to the adsorbate away from subsurface oxygen (Ti-O = 2.84 Å versus 2.14 Å for non-Cp*). However this strain has little effect on the computed energetics: E_{ads} = +0.6 eV for TiCp*$(OMe)_2$ is very close to E_{ads} = +0.6 eV for the non-Cp* fragment, $Ti(OMe)_3$.

The $Ti(OMe)_3$ fragment can coordinate to two surface oxygens (Figure 8c), with a slight energy cost probably due to associated H-transfer on the surface. This increase in Ti coordination number is an example of 'densification', step (v) of the molecule-surface interaction, although in this case it merely restores Ti to five-fold coordination, as prior to MeOH desorption (Figure 5b). This step has the effect of moving Ti to a bulk-like position for crystalline rutile. Steric crowding means that we are unable to find such a densified configuration for the TiCp*$(OMe)_2$ fragment.

Subject to the availability of surface protons, the elimination process can continue. H-transfer to another ligand of the non-Cp* adsorbate yields a $Ti(OMe)_2$(MeOH) fragment (Figure 8d), with E_{ads} = +0.3 eV relative to the gas-phase molecule and hydrated surface, or ΔE_{elim} = +0.9 eV at T = -273.15 °C relative to the $Ti(OMe)_3$(MeOH) fragment (Figure 5b).

As ligands are eliminated, the preference of the adsorbed fragment for surface sites may change. An instance of this is presented in Figure 9b, where $Ti(OMe)_3$ is more stable when bound to a single bridging oxygen (E_{ads} = +0.3 eV, Ti-O = 1.88 Å) than when bound to a terminal oxygen originating from hydration (E_{ads} = +0.6 eV in Figure 8b). Although the coordination number of Ti does not change, this migration of the fragment to the bridging O can be interpreted as another example of densification [step (v)], since this is the expected position for the next Ti atom in the rutile structure. Comparing to the $Ti(OMe)_4$ fragment adsorbed at the same bridging site (Figure 7b), we see that ΔE_{elim} = +0.6 eV, which is less than that computed at the terminal site. This illustrates the interplay between elimination and densification, with the loss of ligands affecting the favoured coordination mode. We suppose that this is primarily a steric effect. As evidence for this, the corresponding Cp*-

containing structure is strongly unfavoured (Figure 9a, E_{ads} = +2.0 eV, Ti-O = 2.15 Å), although the lack of hydrogen bonding between remaining methoxides and surface protons may also play a role in this case.

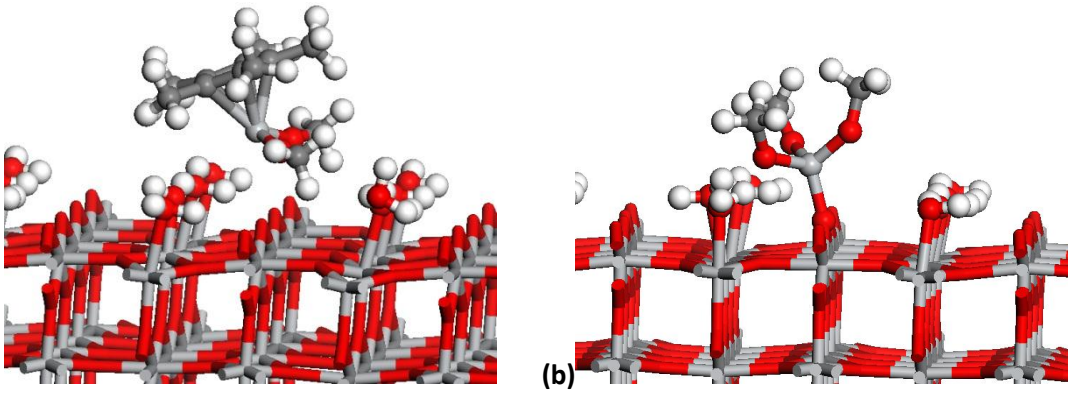


Figure 9: Adsorbate structures after desorption of one MeOH unit, bonding to bridging O: (a) surf-O-Ti(Cp*)$(OMe)_2$, E_{ads} = +2.0 eV, (b) surf-O-$Ti(OMe)_3$, E_{ads} = +0.3 eV.

It is possible to continue this survey and compute precursor fragments at various adsorption sites as the sequence of ligand elimination reactions proceeds in ALD, but we have not done so. These later reaction steps probably affect the efficiency of the ALD process (growth rate, temperature dependence *etc.*) once molecules are adsorbing and growth is taking place. The later steps are not as important as the initial steps in addressing the subject of this paper, namely, why no growth at all occurs for $TiCp^*(OMe)_3 + H_2O$.

5.4 Discussion

While solid titanium methoxide occurs as a tetramer, in the gas phase there is no evidence of such molecular aggregates in the mass spectrometric data presented here. We therefore consider the $Ti(OMe)_4$ molecule as the adsorbing species for study of the mechanism of this precursor from first principles.

Our calculations of precursor molecules on model TiO_2 surfaces show that molecular adsorption [step (i)] can take place, subject to steric constraints. Interaction via the methoxide ligands is favoured due to H-bonding and terminal OH_2 is more accessible than bridging O. Together these factors mean that $Ti(OMe)_4$ can adsorb in various orientations on

various sites, whereas $TiCp^*(OMe)_3$ is constrained to a particular geometry, making adsorption of the latter an entropically less-favoured process. The computed adsorption energies are mostly positive (*i.e.* unfavourable); those that are negative do not exceed -0.5 eV and are therefore smaller in magnitude than the translational and rotational entropy of the gas-phase molecules at T = 275°C [*e.g.* we compute $T(\Delta S_{transl}+\Delta S_{rot.})$ = 1.6 eV for $TiCp^*(OMe)_{3(g)}$]. Molecular adsorption is therefore not thermodynamically favoured, but a small population of molecules may have sufficient lifetime on the surface for H-transfer reactions to take place. This is consistent with the experimental detection at 275°C (but not at 325°C) of Cp* and OMe by ^{13}C NMR when porous silica is treated with $TiCp^*(OMe)_3$ [29].

The most striking difference that we have seen between $TiCp^*(OMe)_3$ and $Ti(OMe)_4$ is during the first H-transfer step of the ALD reaction [step (iii)], when a proton moves from a surface-bound water molecule (or hydroxyl group on other surfaces) to a methoxide ligand. The formation of Ti-O bonds is strongly exothermic and the overall ALD reaction (Equation 2) yields nearly -27 eV/TiO_2. Therefore a driving force for protonation of ligands, weakening of metal-ligand bonds and elimination of ligands can be the concomitant formation of Ti-O bonds to the surface, which is termed 'densification' [step (ii)][47]. This explains why transfer of H to $Ti(OMe)_4$ (Figure 5b) is energetically favourable by -0.1 eV relative to the H-bonded molecule. By contrast, H-transfer to $TiCp^*(OMe)_3$ is highly unfavoured (Figure 5a, +1.1 eV), because there is no flexibility in the ligand shell to allow Ti to coordinate to the surface. We have not computed activation energies for the reaction, but it must be even higher than the energy computed for the intermediate. The inability of Ti to coordinate to surface O therefore causes a high barrier towards subsequent steps in the ALD reaction of $TiCp^*(OMe)_3$.

Methoxide is weakly basic and the hydrated TiO_2 surface is weakly acidic, so that the acid-base reaction producing MeOH is endothermic on its own [*e.g.* ΔE_{elim} = +0.9 eV for $Ti(OMe)_2(MeOH)$ relative to $Ti(OMe)_3(MeOH)$]. Initially, the MeOH molecule remains complexed to Ti, but thermal energy will favour desorption [$T(\Delta S_{transl} + \Delta S_{rot.})$ = 1.1 eV/K for $MeOH_{(g)}$ at 275°C]. Desorption of MeOH leads to less-crowded structures where the energetic effect of Cp* is lessened (Figure 4).

Bulk-like sites for Ti lead to the most compact ('densified') structures and should be the thermodynamically preferred location for Ti atoms to grow. The actual energetics of migration to these sites emphatically illustrates the effect of remaining ligands on Ti (especially the Cp* group). For molecular $Ti(OMe)_4$, migration from terminal O to bridging O costs +0.3 eV (Figure 3b to Figure 7b), while for $TiCp^*(OMe)_3$ the cost is +0.5 eV (Figure 3a to Figure 7a). For fragments with one less methoxide ligand, migration yields -0.2 eV for $Ti(OMe)_3$ (Figure 8b to Figure 9b) but costs +1.4 eV for $TiCp^*(OMe)_2$ (Figure 8a to Figure 9a). One may expect this trend to continue, with densification becoming increasingly favoured as ligands are eliminated. These are tentative clues to how ALD chemistry determines the morpohology of as-deposited films, an aspect about which almost nothing is known at present.

We have seen that $TiCp^*(OMe)_3$ adsorbs on TiO_2 via H-bonding [step (i)] but is too crowded to allow a new Ti-O bond to form [step (ii)]. We find that elimination of ligands [step (iv)] is thermodynamically favoured at typical process temperatures, but can not occur if Ti remains uncoordinated to the surface. Nevertheless, molecular adsorption of $TiCp^*(OMe)_3$ is quite strong and as the ALD pulse continues the surface probably becomes saturated with the unreacted precursor, with OMe ligands pointing down towards the surface and Cp* ligands pointing up (Figure 7a). During the purge, some Ti molecules may desorb (leading to no growth) and others may persist on the surface so as to be exposed to the H_2O pulse. Since Cp* is hydrophobic, there may be little adsorption of H_2O during this pulse [step (i)] and little H-transfer [step (iii)], so that film growth is negligible. Furthermore, as in the metal pulse, elimination of MeOH or Cp*H [step (iv)] will not be favoured unless Ti can at the same time coordinate to surface O [step (ii)], which, as we have seen, is hindered due to the steric demand of Cp*. In fact, it is possible that H_2O will find routes to adsorb directly onto the TiO_2 surface during the H_2O pulse and displace entire Ti-precursor molecules, which would desorb without reaction. Therefore, we suggest that the barrier to initial H-transfer to $TiCp^*(OMe)_3$ also prevents growth reactions taking place during the H_2O pulse.

Successful ALD has been achieved using alternative oxygen sources with $TiCp^*(OMe)_3$, yielding growth rates of 0.30 Å/cycle with O_3 [30] and 0.54 Å/cycle with O_2 plasma[15]. These low growth rates are consistent with persistence of the Ti-precursor as an adsorbed molecule until the O-precursor pulse. Oxidation of the Cp* ligand by O_3 or O_2 plasma

evidently reduces steric hindrance, allows adsorbate Ti to coordinate to surface O and leads to film growth.

We have looked in detail at the steric effect of the Cp* group, but it is also possible that this ligand influences the ALD reactions via the electronic structure of the Ti-Cp* complex. There is a high degree of covalency between Ti and cyclopentadienyl ligands, which causes the electrophilicity of the Ti centre in $TiCp^*(OMe)_3$ to decrease relative to that in $Ti(OMe)_4$. We have seen evidence for this in population analyses of the computed electronic structure of the ground state of the precursor molecules, where the positive charge on Ti is 0.4*e* lower in the Cp* complex than in the homoleptic alkoxide. The lower electrophilicity of the Cp* complex is also evident in the smaller energy gap between HOMO and LUMO levels (the gap for the Cp* complex is 77% of that for the pure alkoxide), bearing in mind that unoccupied orbitals are poorly described by DFT. We would therefore expect Ti-(OMe) bonding to be weaker in the Cp* complex and elimination of the methoxide ligands to be more favoured in that complex, a trend that is not seen in the computed energetics. However we have seen that coordination of the adsorbing Ti to the surface [step (ii)] is more important than ligand elimination. Reduced electrophilicity of the Ti centre in the Cp* case would mean that Ti-O bonding between adsorbing Ti and surface oxygen is weaker, which is indeed observed in our calculations (*e.g.* Figure 5a). Therefore, the electronic effect of the Cp* ligand reinforces the steric effect, insofar as both act to reduce the Lewis acidity of the Ti centre and prevent coordination to the basic sites on the surface.

Little is known about the actual morphology of the oxide surface during ALD but it is likely that it contains a variety of Ti-O geometries and may be described as 'rougher' than the model surface considered here. This would probably mean higher Brønsted acidity when hydrated/hydroxylated [35], facilitating H-transfer and ligand elimination [step (iii)]. It would also mean higher Lewis basicity in terms of under-coordinated O atoms protruding from the surface [38], so that these can more easily coordinate to adsorbing Ti [steps (ii) and (v)]. Overall then, the ALD reactions on the actual surface may be more energetically favoured than those computed on a smooth model surface.

In contrast to TiO_2, the other group 4 oxides ZrO_2 and HfO_2 can be successfully grown by ALD from cyclopentadienyl-containing precursors and water [20-24]. For instance, it is found

that $Zr(MeCp)_2(Me)(OMe)+H_2O$ yields ZrO_2 films with the order of elimination of ligands following their Brønsted basicity (CH_4, then MeCpH, then MeOH)[25]. It appears that there is no impediment to the coordination of Zr to surface O in this case. One explanation is ionic size. From estimates of the ionic radii for six-coordinate M^{4+} cations, *R*(Ti) = 0.61 Å, *R*(Zr) = 0.72 Å, *R*(Hf) = 0.76 Å, we can estimate that the area available for ligands around a hard sphere of radius *R*(Zr) and *R*(Hf) is 139% and 155% respectively of that available around a sphere of radius *R*(Ti). This extra space facilitates coordination to the surface. In addition, the methyl ligand is so reactive that its elimination is likely to be rapid and complete, opening up more space around the metal centre.

'Ligand exchange' is an often-used term to describe half reactions in some ALD processes and (except for the fact that the surface is not a 'ligand') it serves to highlight the thermodynamic driving force towards swapping metal-ligand bonding for metal-surface bonding in ALD. In some cases, such simple 'exchange' is adequate to explain the ALD half-reactions[25], but in other cases (as here) a more detailed view of the ALD mechanism is required, properly describing the changes in coordination at the metal centre as individual reaction steps take place. In the example considered here, the $TiCp^*(OMe)_3$ molecule is apparently too hindered to allow 'exchange' of OMe with surface-O. More correctly, Ti in the adsorbate is too hindered to allow coordination to extra oxygen atoms of the surface, which may be thought of as the first step of densification. Without this step, elimination of ligand adducts (MeOH) from the adsorbate is not possible in either precursor pulse, despite H-transfer, and no ALD growth takes place. 'Densification' describes well the changes in coordination at the Ti centre and so seems to be a more useful label for this reaction than 'ligand exchange'.

Thus, the poor kinetics of an individual step makes the thermodynamically favoured product inaccessible. Referring back to Equation 1, we conclude that ALD is successful only if the complete sequence of reactions from gaseous precursors to bulk-like product takes place (perhaps over many ALD cycles). In each reaction step [(i)-(v) above], the adsorption mode changes and the adsorbate becomes densified into a film as ligands are lost and Ti bonds increasingly to O. We see therefore that ALD is the result of the repeated occurrence of three chemical mechanisms – precursor adsorption, ligand elimination and adsorbate densification – that are closely intertwined.

5.5 Conclusion

Films may be successfully deposited using $Ti(OMe)_4$ in a thermal H_2O-based ALD process, while there is no growth from $TiCp^*(OMe)_3$. Mass spectrometry confirms that titanium methoxide evaporates as the $Ti(OMe)_4$ monomer, so that the difference in growth can not be due to aggregation in the gas phase. DFT calculations were used to further probe the differences between these precursors by considering the mechanistic steps of oxide ALD: (i) adsorption of the precursor molecule at the surface during the Ti-precursor pulse, (ii) coordination of metal atom to the surface, (iii) proton transfer to ligand to form adduct, (iv) elimination of ligand adduct by desorption, (v) further coordination of metal atom to surface oxygen. The simulations reveal that the Cp* ligand of $TiCp^*(OMe)_3$ lowers the Lewis acidity of the Ti centre and prevents its coordination to surface O ('densification') during both of the ALD pulses. The effect of Cp* on Ti seems to be both steric (full coordination sphere) and electronic (lower electrophilicity). By contrast, crowding is much less in monomeric $Ti(OMe)_4$ and so there is no impediment to chemical bonding of Ti from that adsorbate to the surface. This crucial step in the sequence of ALD reactions is therefore not possible in the case of $TiCp^*(OMe)_3 + H_2O$, which means that there is no deposition of TiO_2 films. On the other hand, oxidation of the bulky Cp* ligand with O_3 does allow Ti-O coordination and the subsequent sequence of growth reactions to proceed, which is why ALD with $TiCp^*(OMe)_3 + O_3$ is successful. These findings may also be relevant in understanding the ALD of other 'piano-stool' complexes of the type $[MCpX_3]$. In general, this work highlights the important role played by densification reactions during deposition of material from a vapor, where the coordination number of the metal increases from that of a metal organic precursor to that of a bulk material.

1. Leskelä, M. and M. Ritala, *Atomic layer deposition (ALD): from precursors to thin film structures.* Thin Solid Films, 2002. **409**(1): p. 138-146.
2. Leskelä, M. and M. Ritala, *Atomic Layer Deposition Chemistry: Recent Developments and Future Challenges.* Angewandte Chemie International Edition, 2003. **42**(45): p. 5548-5554.
3. George, S.M., A.W. Ott, and J.W. Klaus, *Surface Chemistry for Atomic Layer Growth.* The Journal of Physical Chemistry, 1996. **100**(31): p. 13121-13131.
4. George, S.M., *Atomic Layer Deposition: An Overview.* Chemical Reviews, 2009. **110**(1): p. 111-131.
5. Ritala, M., et al., *Titanium isopropoxide as a precursor in atomic layer epitaxy of titanium dioxide thin films.* Chemistry of Materials, 1993. **5**(8): p. 1174-1181.
6. Kemell, M., et al., *Atomic Layer Deposition of Nanostructured TiO_2 Photocatalysts via Template Approach.* Chemistry of Materials, 2007. **19**(7): p. 1816-1820.
7. Linsebigler, A.L., G. Lu, and J.T. Yates, *Photocatalysis on TiO_2 Surfaces: Principles, Mechanisms, and Selected Results.* Chemical Reviews, 1995. **95**(3): p. 735-758.
8. Pheamhom, R., C. Sunwoo, and D.-H. Kim. *Characteristics of atomic layer deposited TiO_2 films and their photocatalytic activity*. 2006: AVS.
9. Ni, M., et al., *A review and recent developments in photocatalytic water-splitting using for hydrogen production.* Renewable and Sustainable Energy Reviews, 2007. **11**(3): p. 401-425.
10. Fujishima, A., X. Zhang, and D.A. Tryk, *TiO_2 photocatalysis and related surface phenomena.* Surface Science Reports, 2008. **63**(12): p. 515-582.
11. Paz, Y., et al., *Photooxidative self-cleaning transparent titanium dioxide films on glass.* Journal of Materials Research, 1995. **10**(11): p. 2842-2848.
12. Wang, R., et al., *Light-induced amphiphilic surfaces.* Nature, 1997. **388**(6641): p. 431-432.
13. Miyauchi, M., et al., *Reversible wettability control of TiO_2 surface by light irradiation.* Surface Science, 2002. **511**(1–3): p. 401-407.
14. Albertin, K.F. and I. Pereyra, *Study of reactive sputtering titanium oxide for metal-oxide-semiconductor capacitors.* Thin Solid Films, 2009. **517**(16): p. 4548-4554.
15. Langereis, E., et al., *Remote Plasma ALD of $SrTiO_3$ Using Cyclopentadienlyl-Based Ti and Sr Precursors.* Journal of The Electrochemical Society, 2011. **158**(2): p. G34-G38.
16. Puurunen, R.L., *Surface chemistry of atomic layer deposition: A case study for the trimethylaluminum/water process.* Journal of Applied Physics, 2005. **97**(12): p. 121301.
17. Pore, V., et al., *Atomic Layer Deposition of Photocatalytic TiO_2 Thin Films from Titanium Tetramethoxide and Water.* Chemical Vapor Deposition, 2004. **10**(3): p. 143-148.
18. Wright, D.A. and D.A. Williams, *The crystal and molecular structure of titanium tetramethoxide.* Acta Crystallographica Section B, 1968. **24**(8): p. 1107-1114.
19. S. Elliott, A. Zydor, and M. Nolan, *presented at the 8th International Conference on Atomic Layer Deposition, "Cyclopentadienyl precursors for ALD: Insights from atomic scale simulation",*. 2008, 29 June - 2 July **Bruges, Belgium**.
20. Putkonen, M., et al., *ZrO_2 Thin Films Grown on Silicon Substrates by Atomic Layer Deposition with $Cp_2Zr(CH_3)_2$ and Water as Precursors.* Chemical Vapor Deposition, 2003. **9**(4): p. 207-212.
21. Niinisto, J., et al., *Controlled growth of HfO_2 thin films by atomic layer deposition from cyclopentadienyl-type precursor and water.* Journal of Materials Chemistry, 2005. **15**(23): p. 2271-2275.
22. Dezelah, C.L., et al., *The Atomic Layer Deposition of HfO_2 and ZrO_2 using Advanced Metallocene Precursors and H_2O as the Oxygen Source.* Chemical Vapor Deposition, 2008. **14**(11-12): p. 358-365.

23. Black, K., et al., *Deposition of ZrO_2 and HfO_2 thin films by liquid injection MOCVD and ALD using ansa-metallocene zirconium and hafnium precursors.* Journal of Materials Chemistry, 2008. **18**(38): p. 4561-4571.
24. Niinistö, J., et al., *In Situ Quadrupole Mass Spectrometry Study of Atomic-Layer Deposition of ZrO_2 Using $Cp_2Zr(CH_3)_2$ and Water.* Langmuir, 2005. **21**(16): p. 7321-7325.
25. Elam, J.W., et al., *Mechanism for zirconium oxide atomic layer deposition using bis(methylcyclopentadienyl)methoxymethyl zirconium.* Applied Physics Letters, 2007. **91**(25): p. 253123.
26. Zydor, A. and S.D. Elliott, *Thermal Stability of Precursors for Atomic Layer Deposition of TiO_2, ZrO_2, and HfO_2: An Ab Initio Study of alpha-Hydrogen Abstraction in Bis-cyclopentadienyl Dimethyl Complexes.* The Journal of Physical Chemistry A, 2010. **114**(4): p. 1879-1886.
27. Niinisto, J., et al., *Novel mixed alkylamido-cyclopentadienyl precursors for ALD of ZrO_2 thin films.* Journal of Materials Chemistry, 2008. **18**: p. 5243-5247.
28. Niinistö, J., et al., *Growth and phase stabilization of HfO_2 thin films by ALD using novel precursors.* Journal of Crystal Growth, 2010. **312**(2): p. 245-249.
29. S. Haukka, et al., *"Study on Thermal Stability and Water Reactivity of Various Metal-Organic Titanium Precursors", presented at the 10th International Conference on Atomic Layer Deposition, 21 June 2010, Seoul, Korea.*
30. Rose, M., et al., *Atomic Layer Deposition of Titanium Dioxide Thin Films from $Cp^*Ti(OMe)_3$ and Ozone.* The Journal of Physical Chemistry C, 2009. **113**(52): p. 21825-21830.
31. Hu, Z. and C.H. Turner, *Initial Surface Reactions of TiO_2 Atomic Layer Deposition onto SiO_2 Surfaces: Density Functional Theory Calculations.* The Journal of Physical Chemistry B, 2006. **110**(16): p. 8337-8347.
32. Hu, Z. and C.H. Turner, *Atomic Layer Deposition of TiO_2 from TiI_4 and H_2O onto SiO_2 Surfaces: Ab Initio Calculations of the Initial Reaction Mechanisms.* Journal of the American Chemical Society, 2007. **129**(13): p. 3863-3878.
33. Haran, M., J.R. Engstrom, and P. Clancy, *Ab initio calculations of the reaction mechanisms for metal-nitride deposition from organo-metallic precursors onto functionalized self-assembled monolayers.* Journal of the American Chemical Society, 2006. **128**: p. 836-47.
34. Rodriguez-Reyes, J.C.F. and A.V. Teplyakov, *Mechanisms of adsorption and decomposition of metal alkylamide precursors for ultrathin film growth.* Journal of Applied Physics, 2008. **104**(8): p. 084907.
35. Terranova, U. and D.R. Bowler, *Effect of hydration of the TiO_2 anatase (101) substrate on the atomic layer deposition of alumina films.* Journal of Materials Chemistry, 2011. **21**(12): p. 4197-4203.
36. Mäkinen, V., K. Honkala, and H. Häkkinen, *Atomic Layer Deposition of Aluminum Oxide on TiO_2 and Its Impact on N_3 Dye Adsorption from First Principles.* The Journal of Physical Chemistry C, 2011. **115**(18): p. 9250-9259.
37. Elliott, S.D. and J.C. Greer, *Simulating the atomic layer deposition of alumina from first principles.* Journal of Materials Chemistry, 2004. **14**: p. 3246-3250.
38. Nolan, M. and S.D. Elliott, *Competing Mechanisms in Atomic Layer Deposition of Er_2O_3 versus La_2O_3 from Cyclopentadienyl Precursors.* Chemistry of Materials, 2009. **22**(1): p. 117-129.
39. Zydor, A. and S.D. Elliott, *$TiCp(OMe)_3$ versus $Ti(OMe)_4$ in Atomic Layer Deposition of TiO_2 with WaterAb Initio Modelling of Atomic Layer Deposition Surface Reactions.* Journal of Nanoscience and Nanotechnology, 2011. **11**(9): p. 8089-8093.

40. Cross, J.B. and H.B. Schlegel, *Molecular Orbital Studies of Titanium Nitride Chemical Vapor Deposition: Gas Phase Complex Formation, Ligand Exchange, and Elimination Reactions.* Chemistry of Materials, 2000. **12**(8): p. 2466-2474.
41. Park, J.-K., et al., *Reaction Mechanism for the Hydrolysis of Titanium Alkoxides.* Bulletin of the Korean Chemical Society, 2003. **24**(5): p. 671-673.
42. Ritala, M., et al., *Atomic force microscopy study of titanium dioxide thin films grown by atomic layer epitaxy.* Thin Solid Films, 1993. **228**(1–2): p. 32-35.
43. Peglar, R.J., F.H. Hambleton, and J.A. Hockey, *Surface structure and catalytic cracking properties of the SiO_2BCl_3, SiO_2AlMe_3, and SiO_2AlCl_3 systems: I. Infrared and analytical studies.* Journal of Catalysis, 1971. **20**(3): p. 309-320.
44. George, S.M., et al., *Atomic layer controlled deposition of SiO_2 and Al_2O_3 using ABAB… binary reaction sequence chemistry.* Applied Surface Science, 1994. **82–83**(0): p. 460-467.
45. Puurunen, R.L., et al., *IR and NMR Study of the Chemisorption of Ammonia on Trimethylaluminum-Modified Silica.* The Journal of Physical Chemistry B, 2000. **104**(28): p. 6599-6609.
46. Widjaja, Y. and C.B. Musgrave, *Quantum chemical study of the mechanism of aluminum oxide atomic layer deposition.* Applied Physics Letters, 2002. **80**(18): p. 3304-3306.
47. Olivier, S., et al., *Insights into Crystalline Preorganization of Gas-Phase Precursors: Densification Mechanisms.* Chemistry of Materials, 2008. **20**(4): p. 1555-1560.
48. Hu, Z., J. Shi, and C. Heath Turner, *Molecular dynamics simulation of the Al_2O_3 film structure during atomic layer deposition.* Molecular Simulation, 2009. **35**(4): p. 270-279.
49. Kessler, V.G., G.A. Seisenbaeva, and S. Gohil, *Molecular structure design of single source precursors and multivariate analysis of their evaporation in dynamic vacuum using EI-Mass spectrometry. An approach to Barium–Strontium Titanate–Niobate as a case study.* Surface and Coatings Technology, 2007. **201**(22–23): p. 9082-9088.
50. Kresse, G. and J. Hafner, *Ab initio molecular-dynamics simulation of the liquid-metal–amorphous-semiconductor transition in germanium.* Physical Review B, 1994. **49**(20): p. 14251-14269.
51. Kresse, G. and J. Furthmüller, *Efficiency of ab-initio total energy calculations for metals and semiconductors using a plane-wave basis set.* Computational Materials Science, 1996. **6**(1): p. 15-50.
52. Blöchl, P.E., *Projector augmented-wave method.* Physical Review B, 1994. **50**(24): p. 17953-17979.
53. Kresse, G. and D. Joubert, *From ultrasoft pseudopotentials to the projector augmented-wave method.* Physical Review B, 1999. **59**(3): p. 1758-1775.
54. Perdew, J.P., K. Burke, and M. Ernzerhof, *Generalized Gradient Approximation Made Simple.* Physical Review Letters, 1996. **77**(18): p. 3865-3868.
55. Ireta, J., J. Neugebauer, and M. Scheffler, *On the Accuracy of DFT for Describing Hydrogen Bonds: Dependence on the Bond Directionality.* The Journal of Physical Chemistry A, 2004. **108**(26): p. 5692-5698.
56. Thanthiriwatte, K.S., et al., *Assessment of the Performance of DFT and DFT-D Methods for Describing Distance Dependence of Hydrogen-Bonded Interactions.* Journal of Chemical Theory and Computation, 2010. **7**(1): p. 88-96.
57. Murnaghan, F.D., *The Compressibility of Media under Extreme Pressures.* Proc. Natl. Acad. Sci. U.S.A., 1944. **30**(9): p. 244-247.

58. Nolan, M., et al., *Electronic structure of point defects in controlled self-doping of the TiO_2 (110) surface: Combined photoemission spectroscopy and density functional theory study.* Physical Review B, 2008. **77**(23): p. 235424.
59. Chizallet, C., et al., *Insights into the Geometry, Stability and Vibrational Properties of OH Groups on γ-Al_2O_3, TiO_2-Anatase and MgO from DFT Calculations.* Topics in Catalysis, 2009. **52**(8): p. 1005-1016.
60. Sebbari, K., et al., *Investigation of hydrogen bonds and temperature effects on the water monolayer adsorption on rutile TiO2 (110) by first-principles molecular dynamics simulations.* Surface Science, 2011. **605**(13–14): p. 1275-1280.

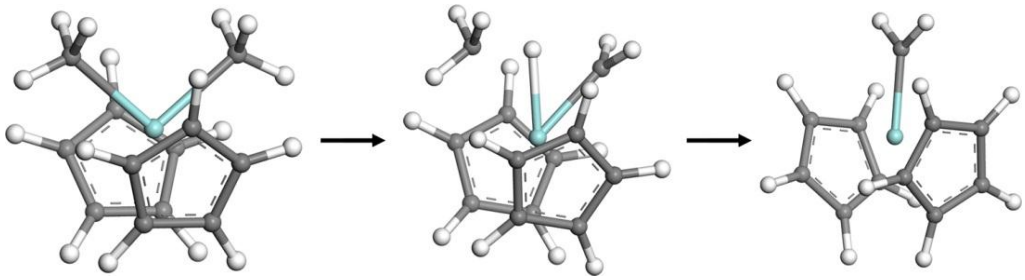
Chapter 6. The thermal stability of precursors for atomic layer deposition of TiO_2, ZrO_2 and HfO_2: an *ab initio* study of α-Hydrogen abstraction in biscyclopentadienyl dimethyl complexes

This chapter was published in the "Journal of Physical Chemistry" as:

Zydor and S.D. Elliott, J. Phys. Chem. A, Vol. **114**, No. 4, 2010 1879–1886

The following article may be found at http://dx.doi.org/10.1021/jp9072608

For this chapter I did the calculations, the analysis and the writing with some assistance of Dr. Simon Elliott.



Thin film dielectrics based on hafnium and zirconium oxides are being introduced to increase the permittivity of insulating layers in nanoelectronic transistor and memory devices. Atomic layer deposition (ALD) is the process of choice for fabricating these films and the success of this method depends crucially on the chemical properties of the precursor molecules. Designing new precursors requires molecular engineering and chemical tailoring to obtain specific physical properties and performance capabilities. A successful ALD precursor should be volatile, stable in the gas-phase, but reactive on the substrate and growing surface, leading to inert by-products. This study is concerned with the thermal stability in the gas phase of Ti, Zr and Hf precursors that contain cyclopentadienyl (Cp = $C_5H_{5-x}R_x$) ligands. We use density functional theory (DFT) to probe the non-ALD decomposition pathway and find a mechanism via intramolecular α-H transfer that produces an alkylidene complex. The analysis shows that thermal stabilities of complexes of the type $MCp_2(CH_3)_2$ increase down group 4 (M = Ti, Zr and Hf) due to an increase in the HOMO-LUMO band gap of the reactants, which itself increases with the electrophilicity of the metal. Precursor decomposition via this pathway in the gas phase can therefore be avoided by replacing the α-H donor or acceptor ligands, or by increasing the electrophilicity of the metal. This illustrates how the ALD process window can be widened by rational molecular design based on mechanistic understanding.

6.1 Introduction

Thin films based on zirconia (ZrO_2) or hafnia (HfO_2) are being used as high-permittivity dielectrics in the latest generation of transistors, and show promise as insulating layers in memories and high-value capacitors [1]. This has in part been enabled by the development of atomic layer deposition (ALD) processes for these materials, delivering films of high purity and uniformity with sub-nanometre thickness control [2]. The ALD process depends intimately on the chemistry of the precursor molecules, and so considerable attention is now being paid to the design, synthesis and properties of organometallic compounds of Zr and Hf.

ALD is a special type of chemical vapour deposition (CVD) in which precursors are admitted separately into the reactor [2]. Ideal ALD is achieved if the reaction of the precursor with the surface is self-limiting, finishing once the surface is saturated with precursor fragments (*e.g.* ligands or hydroxyl groups). Sufficient precursor exposure will then lead to uniform film growth, even coating complex three-dimensional substrates. To achieve ALD's unique characteristic the precursor must have specific properties. It should be volatile and vaporize rapidly at the reproducible rate, conditions that are usually met for liquid precursors, but not for solids. For self-terminating surface reactions it should not self-react, but it should be reactive on the substrate and growing surface. However many precursor molecules undergo intra- or inter-molecular reactions, either in the gas-phase or on the surface, that do not self-limit and are termed decomposition reactions. In general, such non-ALD decomposition is thermally activated, and so can also be significant when the precursor is heated to volatilise it or when it enters the heated chamber of the ALD reactor. Non-ALD decomposition can lead to the waste of precursor chemicals, uncontrolled film growth, impure films, poor thickness control, and uneven coating in two and three dimensions. For example, Zr and Hf amide precursors show deleterious decomposition as the reactor temperature is increased. As-deposited hafnium oxide films showed non-uniformity that increased from 1% to 5% of the film thickness as the deposition temperature was raised, indicating a contribution from non-ALD decomposition reactions. For zirconium oxide, similar roughness was already observed at much lower deposition temperatures [3].

Recently, a new family of cyclopentadienyl precursors of Zr and Hf have been introduced [4], some of which show enhanced thermal stability and are more suitable for high-temperature growth. The stability of the family of cyclopentadienyl precursors has been

investigated in static thermogravimetric experiments, revealing a significant difference between the stability of Zr and Hf compounds: the involatile residues for $Hf(MeCp)_2Me_2$ and $Zr(MeCp)_2(OMe)Me$ are very low (< 2%) indicating that no significant decomposition occurs as the precursors are volatilized [5]. In contrast, the very high residue (> 50%) observed for $Zr(MeCp)_2Me_2$ shows that decomposition occurs under relatively mild conditions ($\sim$ 200 °C). $Zr(MeCp)_2Me_2$ decomposes violently after 4h at 160 °C.

Currently, little is known about these differences in thermal stability and about the underlying mechanism of decomposition of ALD precursor molecules. However, to design new ALD precursors and develop and optimize an ALD process for the deposition of new materials requires knowledge of the reaction mechanism. Most of the studies on ALD modelling have been dedicated on ALD mechanisms[6] and the reactions of precursors with the surface[7],[8], The presence of thermal decomposition means that we also need to understand the mechanism of precursor reactions that happen in the gas-phase. Therefore, the aim of our studies is to investigate possible decomposition reaction pathways and to explain the observed differences in thermal stability. The precursor complexes that are the subject of this study are denoted ML_2Me_2 where M is a group 4 metal M = Ti, Zr or Hf and the ligands are L = Cp, MeCp, OMe, Me (Me = CH_3).

The molecules that we study here are new to the ALD research area but have been widely studied in organometallic and organic synthesis. A derivative of the Ti complex functions as a Ziegler Natta polymerisation catalyst [9]. Tebbe *et al.* [10] discovered that a complex derived from titanocene dichloride and trimethylaluminium olefinates carbonyl compounds [11, 12] such as ketones, aldehydes and amides. For esters and thioesters it is more efficient to use dimethyl titanocene (the Petasis reagent), [11] which undergoes thermal elimination of CH_4 from the position α to the metal, to afford a titanium alkylidene complex ($Cp_2Ti{=}CH_2$), also known as a Schrock carbine [13]. Alkylidenes can generally be obtained by the α-deprotonation of di- or polyalkyl complexes of coordinatively saturated early transition metals in high oxidation states (d^0) [14, 15].

It is known that the reactivity of tetraalkyl complexes of transition metals strongly depends on steric effects between the alkyl ligands and on the identity of metal itself, [13, 16] affecting both the mechanism and the energetics of the decomposition reaction. Two mechanisms of methane elimination from tetramethyl complexes of Ti, Zr and Hf were studied through: 1) intramolecular and 2) intermolecular α-H abstraction [17]. Schrock *et al.*

have postulated that when the alkyl group is small, *e.g.* methyl, the first step is bimolecular α-hydrogen abstraction, which is rate-determining [13, 18-21]. The calculated activation enthalpies according to the bimolecular mechanism are in the order $ZrMe_4$ (64.9 kJ/mol) < $HfMe_4$ (82.8 kJ/mol) ~ $TiMe_4$ (83.7 kJ/mol), which is in agreement with measurements [16, 17, 22]. When the alkyl group becomes bulkier, the bimolecular mechanism becomes unfavorable because of steric reasons and the unimolecular mechanism becomes favored instead. In the case of complexes with bulkier alkyl ligands, theory and experiment show the stability increasing in the order $TiNp_4$ < $ZrNp_4$ < $HfNp_4$ (Np = neopentyl C_5H_{11}), which is consistent with unimolecular decomposition [17, 23]. Indeed, unimolecular α-H abstraction is found to proceed readily in group 4 organometallics where there is significant crowding and a suitable acceptor ligand, with first-order reaction kinetics indicative of a rate determining step where C-H bonds are made and broken in a cyclic reaction path [17, 24]. Consistent with this, CH_4 was observed as a product of the decomposition of $TiCp_2Me_2$, $ZrCp_2Me_2$ and $HfCp_2Me_2$ and it was shown that dissociation of the M-Me bond or abstraction of H from a methyl group is the rate determining step [25]. The thermal stability of these compounds is found to increase down group 4, which suggests an electronic effect at the metal centre. The question of steric *versus* electronic effects has also been discussed for Nb and Ta alkylidenes [13]. It is suggested that any change in the ligands that increases the electrophilicity of the metal should increase the rate of α-H abstraction and elimination of CH_4. Looking here at group 4, the chemistry of Zr and Hf compounds is very similar to one another. In particular, the ground-state properties of ZrO_2 and HfO_2, such as their structure and vibrational frequencies, are very similar[26]. By contrast, the difference in excited-state properties is much greater; *e.g.* the adiabatic electron affinity of HfO_2 was determined to be 2.14 ± 0.03 eV, and that of ZrO_2 was determined to be 1.64 ± 0.03 eV, indicating that HfO_2 is more ionic than ZrO_2 [26].

Therefore, in the ML_2Me_2 complexes that we study here, bulky ligands (such as L = Cp) may favour unimolecular α-H transfer between the methyl ligands, and there may be electronic reasons for differences between M = Ti, Zr and Hf. We propose Equation 1 as a possible decomposition pathway:

$$ML_2Me_2 \rightarrow ML_2(CH_2) + CH_4 \qquad \text{Equation 1}$$

As outlined above, there is much evidence for α-hydrogen abstraction during the decomposition of transition metal complexes. The aim of our work is to investigate and

understand the mechanism of α-hydrogen abstraction in case of MCp_2Me_2 complexes for M = Ti, Zr, Hf, which is possibly the first step in their decomposition. We use density functional theory (DFT) to calculate the electronic and molecular structure and characterize this decomposition pathway (precursors, transition states (TS) and products; activation energy E_a and reaction energy ΔE). In order to find out what role is played by the non-reacting ligands (spectator ligands) L the calculations were also performed for L= MeCp, Me, and OMe in the complexes ZrL_2Me_2. In the case of $Zr(MeCp)_2Me_2$ we briefly test the competing reaction of β-hydrogen abstraction. For a series of choices of metal M = Ti, Zr, Hf and ligand L = Cp, MeCp, Me, OMe, we use DFT vibrational analyses to confirm the nature of the stationary points and to obtain entropy and free energy changes.

As illustrated by the catalytic activity mentioned above, the carbene product is highly reactive, and so it is likely that further unimolecular or bimolecular reactions follow Equation 1. It is not our attempt to calculate this wide range of subsequent reactions. However, we include a brief study of β-H abstraction as a competing first step (Equation 2) or second step reaction (Equation 3) of decomposition process, as was suggested for related molecule $TiCp^*_2Me_2$ ($Cp^* = C_5Me_5$) [20].

6.2 Theoretical methods

The precursor molecules and their ALD reaction products were modeled as isolated molecules in vacuum. The ground state electronic wavefunction of each molecule was calculated self-consistently within Kohn-Sham Density Functional Theory (DFT) using the TURBOMOLE suite of quantum chemical programs [27]. All species were closed shell. Unconstrained optimization of the molecular geometry was carried out on the DFT potential energy hypersurface. Vibrational analysis was performed for each considered structure in order to characterize the nature of the stationary point. A stationary point found by a geometry optimization is a minimum (local or global following its stability) when all the vibrational frequencies are real. In contrast, it is a transition state (TS) linking two minima when there is one imaginary frequency. A good trade-off between accuracy and computational cost was obtained by using the B-P86 functional, the RI approximation, [28-30] and the atom-centered TZVP(P) basis set [31] with effective core potentials of 28 electrons on Zr and of 60 electrons on Hf [32].

6.3 Results

6.3.1 Decomposition pathway

The computed reaction coordinate for Equation 1 is primarily the transfer of H from one methyl group to the other, producing CH_4 which dissociates from the complex, leaving methylene bound to the metal centre in $ML_2(CH_2)$ (Figure 1). H-transfer is coupled with the slight contraction of the $C(CH_4)$-M-$C(CH_2)$ angle, where in our notation $C(CH_4)$ represents a carbon atom in a leaving methyl group and $C(CH_2)$ is a carbon atom of the remaining methyl group. At the TS, the four atoms involved in the reaction are co-planar, namely $C(CH_4)$, $C(CH_2)$, H and M.

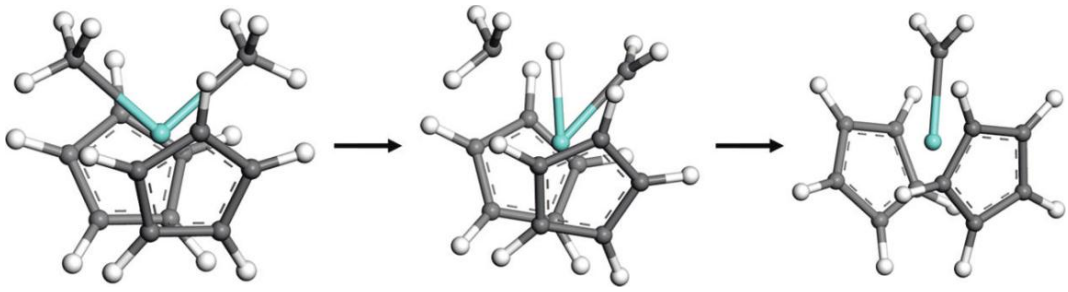


Figure 1 – Ball and stick representations of computed structures of precursor (reactant), TS and product along decomposition pathway (Equation 1) for L = Cp, M = Zr; white = hydrogen, grey = carbon, blue = Zr.

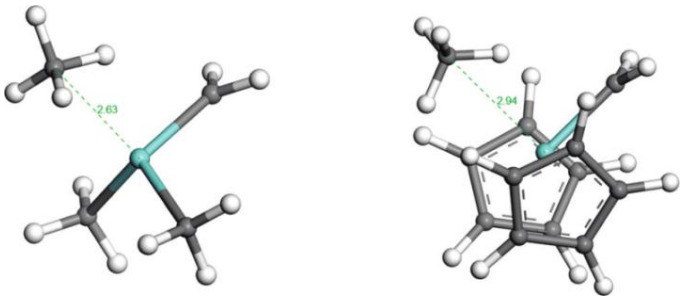


Figure 2 – Ball and stick representations of computed structure of intermediate occurring during the decomposition pathway (Equation 1) for L = Me, Cp, M = Zr, white = hydrogen, grey = carbon, blue = Zr. The depth of the minimum of the intermediates is reflected in the M-$C(CH_4)$ distances: 2.94 Å and 2.63 Å for L = Cp and Me respectively.

The computed energetics of Equation 1 for L = Cp are presented in Table 1 and Figure 3. The activation energy and overall endothermicity become greater down the group, with the Ti complex most likely to decompose, the Zr complex substantially more stable, and the Hf

complex slightly more stable again. The decomposition reaction leads to a carbene product of higher energy than compared to the reactant, and this carbene is in turn likely to be highly reactive. The stability of the carbene product decreases down the group. The reasons for these differences are explored below. The entropic contribution is slightly less at the TS, but increases substantially as the second product molecule is formed, lowering ΔG for the overall reaction by over 20 kJ/mol at 298 K. In the cases of M = Zr and Hf, the DFT energies show a slight minimum in the dissociation channel (Figure 2) consisting of weakly bound CH_4, which opens up the possibility of the reverse reaction occurring. However, this minimum disappears when corrected for entropy at $T > 0$.

For the corresponding decomposition reaction of $Zr(MeCp)_2(Me)(OMe)$ to $Zr(MeCp)_2(CH_2)$ and MeOH the computed reaction energy is ΔE = 299 kJ/mol, but we were unable to find a TS which leads to these products. However, we found a minimum on the dissociation channel similar to the intermediates presented in Figure 2. The energy cost for the formation of this intermediate compared to the reactant is ΔE = 217 kJ/mol.

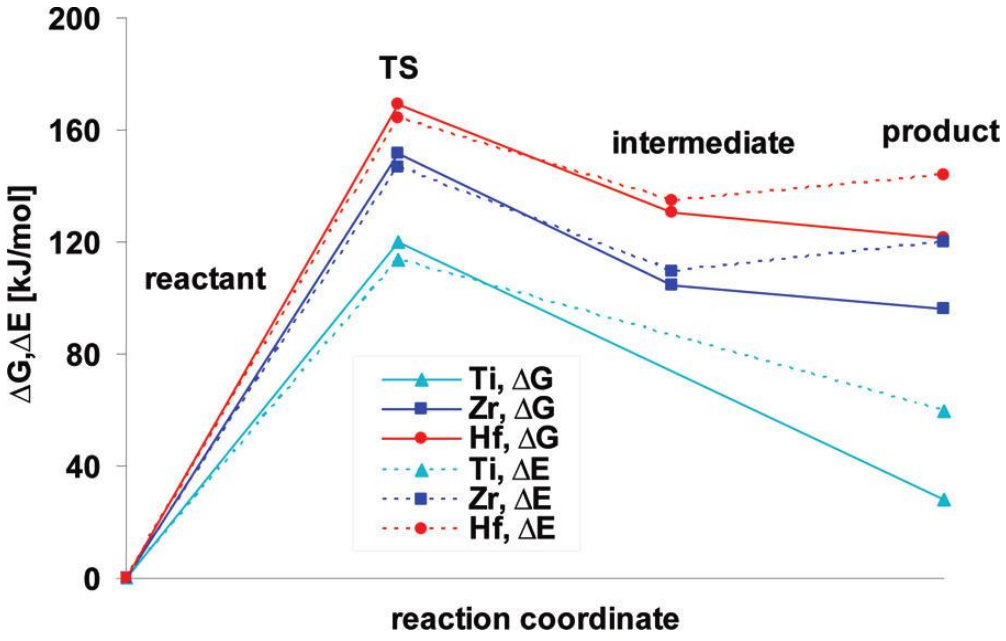


Figure 3 – Computed energetics along the decomposition pathway from the data in Table 1. Lines are to guide the eye.

Table 1: Energetics along the decomposition pathway Equation 1 computed using DFT. Positive values indicate an energetic cost relative to the reactants. The Gibbs free energy is obtained from $\Delta G = \Delta H - T \cdot \Delta S$ at T = 298 K. Illustrated in Figure 3.

		$TiCp_2Me_2$	$ZrCp_2Me_2$	$HfCp_2Me_2$
TS	E_a **(kJ/mol)**	114	147	164
	S_a **(kJ/mol·K)**	-0.020	-0.016	-0.016
	G_a **(kJ/mol)**	120	151	169
intermediate	ΔE **(kJ/mol)**	-	109	135
	ΔS **(kJ/mol·K)**	-	0.016	0.015
	ΔG **(kJ/mol)**	-	104	130
product	ΔE **(kJ/mol)**	60	120	145
	ΔS **(kJ/mol·K)**	0.106	0.080	0.077
	ΔG **(kJ/mol)**	28	96	121

Table 2: Selected parameters of the DFT optimized structures of MCp_2Me_2 (reactants), M = Ti, Zr or Hf, transition states and products according to Equation 1. The centroid of the C atoms of Cp is denoted Cp_{cent}.

Distance [Å]	$TiCp_2Me_2$			$ZrCp_2Me_2$			$HfCp_2Me_2$		
	React.	**TS**	**Prod.**	**React.**	**TS**	**Prod.**	**React.**	**TS**	**Prod.**
M-C(CH_2)	2.18	1.98	1.95	2.29	2.09	2.07	2.28	2.09	2.07
M-C(CH_4)	2.18	2.46	-	2.29	2.55	-	2.28	2.55	-
M-H	2.85	1.80	-	2.851	1.94	-	2.856	1.94	-
CH_3-H	1.10	1.41	-	1.10	1.40	-	1.10	1.37	-
H-CH_2	1.10	1.57	1.10	1.10	1.66	1.10	1.10	1.71	1.10
M-Cp_{cent}	2.10	2.10	2.09	2.26	2.24	2.22	2.26	2.24	2.21
M-Cp_{cent}	2.10	2.08	2.05	2.25	2.24	2.22	2.26	2.24	2.21
Angle [°]									
C(CH_4)-M-C(CH_2)	94.4	83.2	-	99.8	81.3	-	97.8	82.1	-
Cp_{cent}-M-Cp_{cent}	134.9	131.4	143.0	133.5	136.9	144.4	133.2	136.3	143.8

6.3.1 Effect of the metal cation

In order to understand the different decomposition behaviour of M = Ti, Zr and Hf, we have analysed their atomic and electronic structure along the reaction pathway for L = Cp. Table 2 lists the most important structural parameters.

The primary factor is the size of the cation: M-C distances are consistently 0.10-0.15 Å shorter for M = Ti than for the other M, while those for Zr and Hf are generally identical to within 0.01 Å. However in all cases, the M-C(CH_2) distance decreases by 0.2 Å as M-CH_3 is transformed into M-CH_2, and most of this decrease has already occurred when the TS is reached. The angle that the methyl ligands subtend at the metal centre in the reactant complex is 94° for M = Ti and 98-100° for M = Zr, Hf. This narrows to a more consistent 81-83° at the TS.

Ti-Cp distances remain roughly constant throughout the reaction, but the Cp ligands have space to move apart in the product, as evidenced by the wider Cp_{cent}-Ti-Cp_{cent} angle. For Zr and Hf, the product complexes show a similar widening of this angle, accompanied here by a 0.05 Å shortening of M-Cp_{cent}.

The electronic structure of the reactants, transition states, and products is analysed in terms of the HOMO (highest occupied molecular orbital), LUMO (lowest unoccupied molecular orbital) and energy gap between these orbitals (Table 3). Since DFT functionals such as B-P86 systematically underestimate the energies of unoccupied orbitals, we consider only the trends across these systems. The HOMO is nearly degenerate with the HOMO-1 in the reactant (because of near-symmetry) and these orbitals are the only occupied ones to show significant M:*d* character. Plotting these orbitals Figure 4 reveals that they are three-centre σ-bonding between M and the two C_{2v}-symmetric C(CH_3) atoms, but the proportion of M character in Mulliken population analysis is seen to be slightly more for Ti than for Zr and Hf (not quoted here). There is a very small contribution from Cp:π to the HOMO.

The LUMO of the reactant is of predominantly M:*d* character (not plotted here) and its energy rises down the group Ti, Zr, Hf. Consequently, the energy gap from HOMO to LUMO is strongly dependent on M, increasing down the group from 290 kJ/mol for M = Ti to 373 kJ/mol for M = Hf (Table 3). On the basis of total charge density from Mulliken population analysis, the positive charge of M also increases down the group (Table 3), consistent with higher ionicity.

Table 3: Analysis of HOMO (highest occupied molecular orbital) (see Figure 4) and LUMO (lowest unoccupied molecular orbital) during decomposition: energy level of the HOMO and LUMO, energy gap between HOMO and LUMO (ε_g), total charge density *q* of metal cation [M] from Mulliken population analysis.

		Reactant	TS	Product
$TiCp_2Me_2$	ε_g (kJ/mol)	290	265	129
	LUMO (E_h)	-0.100	-0.064	-0.114
	HOMO (E_h)	-0.211	-0.165	-0.163
	q [Ti]	0.17	-0.02	0.35
$ZrCp_2Me$	ε_g (kJ/mol)	349	288	135
	LUMO (E_h)	-0.078	-0.052	-0.106
	HOMO (E_h)	-0.211	-0.162	-0.157
	q [Zr]	0.56	0.17	0.41
$HfCp_2Me_2$	ε_g (kJ/mol)	373	298	125
	LUMO (E_h)	-0.068	-0.044	-0.104
	HOMO (E_h)	-0.210	-0.158	-0.152
	q [Hf]	0.62	0.25	0.49

C_{2v} symmetry is lifted as H-transfer proceeds. Both HOMO and LUMO shift in energy. In all of the Cp complexes the HOMO becomes destabilised as the reaction proceeds. At the transition state, the energy of the LUMO also rises but then falls in the product.

As the reaction proceeds, the HOMO-LUMO energy gap decreases for all the complexes leading to the products of almost identical HOMO-LUMO gaps (125-135 kJ/mol). In contrast with the reactants, the product complexes show very similar HOMO orbital structures for M = Ti, Zr, Hf.

At the TS we see the electron density in the HOMO shifting from $C(CH_4)$ to both $C(CH_2)$ and M. The product HOMO is of predominantly $C(CH_2)$:*p* and M:*d* character, and plots of this orbital confirm that it is M-$C(CH_2)$ π-bonding Figure 4. At the TS, calculations show a negligible HOMO population on the transferring H and negligible change in the overall electron density on that H, suggesting the transfer of neutral H. Already at the TS we see the creation of new bonding between the H and $C(CH_4)$ of length 1.399 Å. Based on this, we

propose in Figure 5 the way that HOMO electrons are transferred along the decomposition pathway.

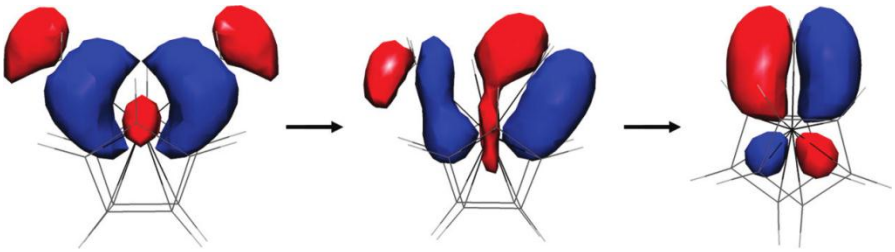


Figure 4 – Plotted HOMO orbitals of computed structures of reactant, transition state and product along decomposition pathway (Equation 1) for L = Cp, M = Zr.

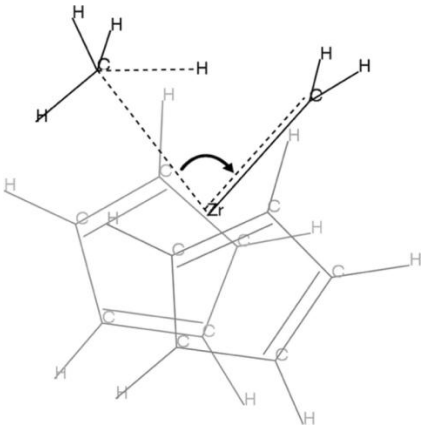


Figure 5 – Line representations of computed structure of TS occurring during the decomposition pathway (Equation 1) for M = Zr, L = Cp. Bond lengths indicate that a partial H-CH_3 bond (dotted line) is formed in the TS. The arrow indicates the observed transfer of HOMO electrons during the decomposition. The spectator ligands are in grey.

6.3.2 Effect of the spectator ligands

In order to determine what role is played by the non-reacting ligands (spectator ligands) in the unimolecular decomposition reaction (Equation 1), we have considered this reaction pathway for a variety of alternative non-reacting ligands L = Cp, MeCp, Me, and OMe in the complexes ZrL_2Me_2. It has been shown, however, that in the case of smaller spectator ligands (L = Me), the decomposition reaction in fact proceeds by bimolecular, intermolecular α-hydrogen abstraction because of the release of steric interactions [17].

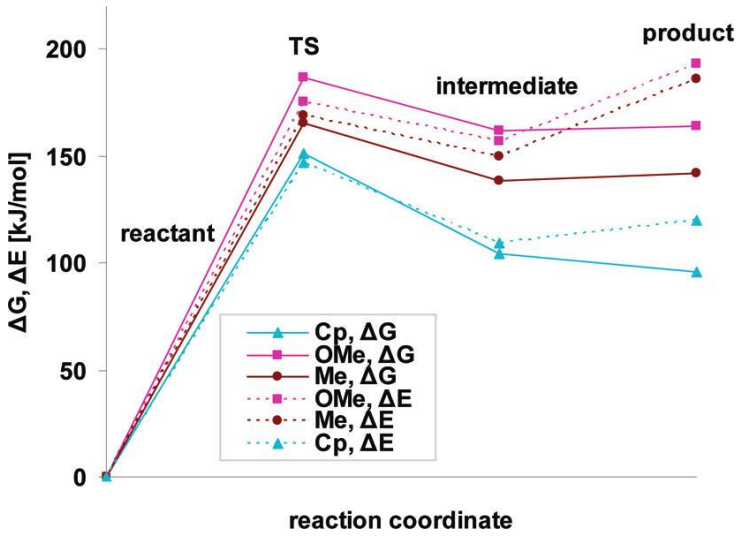


Figure 6 – Computed energetics along the decomposition pathway (Equation 1) from the data in Table 6. Lines are to guide the eye.

The computed energetics of Equation 1 for L = Cp, Me, and OMe are presented in Figure 6 and Table 4. We see that the identity of the non-reacting ligand has a strong impact on the decomposition reaction. The activation energy and overall endothermicity become greater when replacing Cp with Me and OMe. The most likely complex to decompose is $ZrCp_2Me_2$ which has the lowest activation energy, while $ZrMe_4$ and then $Zr(OMe)_2Me_2$ seem to be more stable in this decomposition pathway. In all the cases of L = Cp, OMe and Me the DFT energies show a minimum in the dissociation channel as was shown already for $ZrCp_2Me_2$. However, in contrast to $ZrCp_2Me_2$, the minimum for L = Me and OMe (Figure 6) is deeper and does not quite disappear when corrected for entropy at $T > 0$, which opens up the possibility of the reverse reaction occurring. The entropic contribution is small at the TS for all the complexes, decreasing for L = Cp and OMe but increasing for L = Me and even more for MeCp. The entropy increases substantially as the product molecules are formed, lowering ΔG for the overall reaction by 24, 39, 29 and 44 kJ/mol for L = Cp, MeCp, OMe, and Me respectively at $T = 298$ K.

In order to understand the influence of spectator ligands L = Cp, MeCp, Me, and OMe on different decomposition behaviours of ZrL_2Me_2 complexes, we have analysed their atomic and electronic structure along the reaction pathway Equation 1. Figure 5 lists the most important structural parameters.

The effect of the spectator ligands on the reacting ligands is particularly reflected in the $C(CH_4)$-Zr-$C(CH_2)$ angles. The angle to which the reacting methyl ligands subtend at the

Table 4: Energetics along the decomposition pathway (Equation 1) computed using DFT. Positive values indicate an energetic cost relative to the reactants. The Gibbs free energy is obtained from $\Delta G = \Delta E - T \cdot \Delta S$ at T = 298 K. Illustrated in Figure 6.

		$ZrCp_2Me_2$	$Zr(MeCp)_2Me_2$	$ZrMe_4$	$Zr(OMe)_2Me_2$
TS	E_a **(kJ/mol)**	147	150	169	175
	S_a **(kJ/mol·K)**	-0.016	-0.008	0.012	-0.038
	G_a **(kJ/mol)**	151	152	166	187
Intermediate	ΔE **(kJ/mol)**	109	114	150	157
	ΔS **(kJ/mol·K)**	0.016	-0.025	0.037	-0.018
	ΔG **(kJ/mol)**	104	122	139	162
Product	ΔE **(kJ/mol)**	120	121	186	193
	ΔS **(kJ/mol··K)**	0.080	0.130	0.147	0.098
	ΔG **(kJ/mol)**	96	82	142	164

metal centre in the reactant complex is 107° for $Zr(OMe)_2Me_2$ and due to tetrahedral symmetry is 109° for $ZrMe_4$, while in the Cp complex it is tightened up to 100°. This narrows to a more consistent 81-86° at the TS for all complexes, although here again we see the steric effect of the Cp ligands, tightening up the $C(CH_4)$-Zr-$C(CH_2)$ angle by about 5°.

Zr-$C(CH_2)$ distances differ slightly (< 0.1 Å) in the reactants. In all cases the Zr-$C(CH_2)$ distance decreases by 0.22-0.24 Å as Zr-CH_3 is transformed into Zr-CH_2 and most of this decrease has already occurred when the TS is reached.

M-L distances of spectator ligands remain roughly constant throughout the reaction. As a result of the decreasing $C(CH_4)$-Zr-$C(CH_2)$ angle at the TS, the spectator ligands have space to move apart, as evidenced by the wider L-M-L angle. This angle keeps increasing along the decomposition pathway for Cp and OMe but decreases back to 111° in the case of the $ZrMe_4$ complex.

The electronic structure of the HOMO during the decomposition reaction of $ZrMe_4$ and $ZrMe_2(OMe)_2$ is presented in Table 6 in terms of the energy level of the HOMO and LUMO as well as the energy gap between these orbitals. We repeat in the tables here the information on $ZrMe_2Cp_2$ to better explain the effect of spectator ligands in the group of Zr complexes.

Table 5: Selected parameters of the DFT-optimized structures of ZrL_2Me_2 (reactants), L = Cp, Me, OMe, transition states and products according to Equation 1. The centroid of the C atoms of Cp is denoted Cp_{cent}. The point symmetry group of each molecule is also given.

	$ZrCp_2Me_2$			$Zr(OMe)_2Me_2$			$ZrMe_4$		
Distance [Å]	**React.**	**TS**	**Prod.**	**React.**	**TS**	**Prod.**	**React.**	**TS**	**Prod.**
symmetry	C_{2v}	C_1	C_{2v}	C_{2v}	C_1	C_s	T_d	C_1	C_s
M-C(CH_2)	2.29	2.09	2.07	2.25	2.06	2.02	2.23	2.04	1.99
M-C(CH_4)	2.29	2.55	-	2.25	2.46	-	2.23	2.42	-
M-L/Cp_{cent}	2.26	2.24	2.22	1.93	1.95	1.94	2.23	2.25	2.23
Angle [°]									
C(CH_4)-M-C(CH_2)	99.8	81.3	-	107.1	85	-	109.5	86.0	-
L-M-L	133.5	136.9	144.4	117.3	125.5	128.5	109.5	115.2	110.8

Table 6: Analysis of HOMO (highest occupied molecular orbital) and LUMO (lowest unoccupied orbital) during decomposition: energy level of the HOMO and LUMO, energy gap between HOMO and LUMO (ε_g), total charge density *q* of metal cation [M] from Mulliken population analysis.

		Reactant	**TS**	**Product**
$ZrMe_2Cp_2$	q [Zr]	0.56	0.17	0.41
	q [C=]	0.56	0.17	0.41
	q [C]	0.56	0.17	0.41
	q [H]	0.56	0.17	0.41
$ZrMe_4$	ε_g (kJ/mol)	411	285	170
	LUMO (E_h)	-0.070	-0.071	-0.104
	HOMO (E_h)	-0.227	-0.180	-0.169
	q [Zr]	0.89	0.93	0.91
$ZrMe_2OMe_2$	ε_g (kJ/mol)	416	327	147
	LUMO (E_h)	-0.052	-0.040	-0.097
	HOMO (E_h)	-0.210	-0.165	-0.153
	q [Zr]	1.22	0.94	0.97

Mulliken population analysis along the reaction pathway shows a gradual transfer of HOMO electron density from a three-centre σ C(Me)-Zr-C(Me) bond (in the case of $ZrMe_2(OMe)_2$) and a five-centre σ C_2(Me)-Zr-C_2(Me) bond (in case of $ZrMe_4$) to a two-centre π Zr-C(CH_2) bond, similar to that detailed above for L = Cp. The product has two occupied orbitals localised on Zr-C(CH_2), the higher of which is of Zr:*d*-C:*p* π-bonding character similar to all product complexes.

Mulliken population analysis reveals that HOMO and HOMO-1 orbitals show significant M:*d* character. The proportion of M character is seen to be more for the $ZrMe_4$ complex than for $ZrCp_2Me_2$ and $ZrMe_2OMe_2$ complexes. As in all Cp complexes, the LUMO of L = Me and OMe complexes are also of predominantly M:*d* character. As presented in Table 6, the energy gap from HOMO to LUMO is strongly dependent on non-reacting ligands. The influence of Cp ligands is clearly seen here: the energy gap is 62-67 kJ/mol lower compared to Me and OMe ligands.

Examining the HOMO and LUMO energies of the reactants reveals two different causes for the greater band gap when Cp is replaced by Me or OMe. In the reactant $ZrMe_4$, four orbitals show Zr-C character. As expected in tetrahedral symmetry, three of them are degenerate in energy and constitute the HOMO. In total, 8 electrons are delocalised over both reacting and spectator Me ligands. More delocalisation means that the HOMO is much lower in energy than in the Cp and OMe cases, and the band gap is correspondingly higher. In contrast, Cp and OMe spectator ligands have very little contribution to the reactant HOMO in their respective complexes. The L = OMe spectator is seen to drive up the LUMO energy level, again opening the band gap. This destabilisation of empty Zr:*d* states is also reflected in the highly ionic character of the Zr centre (*q*(Zr) in Table 6), consistent with the nucleophilic ligands L = OMe. The differences between the complexes with different L are most obvious in the reactants, and less marked in the product.

6.3.3 Possible reaction of 'spectator' ligands

In a case of the $Zr(MeCp)_2Me_2$ complex we have also investigated the possibility of decomposition via β-hydrogen abstraction from one methyl group of the MeCp ligand yielding a tuck-in complex according to Equation 2:

$$ML_2Me_2 \rightarrow ML_2(CH_2) + CH_4 \qquad \text{Equation 2}$$

The activation energy is calculated to be E_a = 144 kJ/mol and Gibbs free energy G_a = 156 kJ/mol at T = 298 K, with some variation with rotation of the two MeCp units. This activation energy is comparable with that computed for α-hydrogen abstraction. However, in the case of $TiCp^*_2Me_2$, isotope labelling experiments show that this reaction plays a minor part in decomposition (only 2% of the product) [20] Alternatively, the same tuck-in complex $Zr(MeCp)(C_5H_4CH_2)Me$ could be formed by intramolecular H-transfer within the alkylidene complex $Zr(MeCp)_2(CH_2)$ as described by Equation 3:

$$Zr(MeCp)_2CH_2 \rightarrow Zr(MeCp)(C_5H_4CH_2)Me \qquad \text{Equation 3}$$

The reaction is highly exothermic and ΔE = -86 kJ/mol is calculated. Equation 3 is thus a possible second step of the decomposition of $Zr(MeCp)_2Me_2$, analogous to that reported for $TiCp^*_2Me_2$ [20] .

6.4 Discussion

The aim of our work is to investigate and understand the mechanism of α-hydrogen abstraction in cyclopentadienyl dimethyl precursor molecules of Ti, Zr and Hf complexes, which possibly is the first step reaction in their unimolecular decomposition. Our study can be then helpful in understanding the decomposition of those complexes and in proposing chemical modifications to enhance their thermal stability, thus increasing their utility as precursors for atomic layer deposition.

The decomposition mechanism of Cp complexes of group 4 metals, especially Ti, has been investigated for a long time [24, 25]. The $TiCp_2Me_2$ complex is the common Petasis reagent [11], which decomposes according to Equation 1 to afford a titanium alkylidene (Schrock carbene) [15] [13] that is used in the olefination of carbonyl compounds. This reaction, Equation 1, is also used to prepare alkylidene complexes of V^V, Nb^V, Ta^V, Cr^{VI}, Mo^{VI}, W^{VI} and Re^{VII} [13, 14]. $ZrCp_2Me_2$ with oxygen and water was used in MOCVD of ZrO_2 at 400-550°C. It is possible that the decomposition reaction we present here participated in this MOCVD process in a similar way to the reaction of carbenes with esters in the olefination reaction [12].

There are still many open questions concerning the critical point of α-hydrogen abstraction - the TS [13, 20]. For the first time, we have used DFT to compute the reactants, TS and products of Equation 1 for group 4 complexes MCp_2Me_2. We have calculated the energetics

of the decomposition reaction and, as expected, the results differ for Ti, Zr and Hf complexes. Analysing their geometrical and electronic structures, we are able to explain the differences in TS energetics and in rates of decomposition. The calculated trends in activation energies are in agreement with experimental findings on the thermal stability of Cp complexes [5, 25, 33]. The excellent agreement between our computed data for $TiCp_2Me_2$ (E_a = 114 kJ/mol, TS_a = -0.02 kJ/mol) and those measured for the related compound $TiCp^*_2Me_2$ (ΔH = 116 kJ/mol, $T\Delta S$ = -0.01 kJ/mol for) [20] may be fortuitous given the systematic inaccuracies of DFT. The decomposition reaction leads to a carbene product of high energy which is likely to be very reactive. We suggest that the carbene rapidly undergoes subsequent reactions with precursor molecules, ultimately aggregating into a solid residue and releasing considerable energy. Equation 1 is thus the rate-determining initial step. This explanation is in agreement with the experimental analysis of cyclopentadienyl precursor molecules of Ti, Zr and Hf complexes [5, 25].

We therefore suggest that α-H abstraction and decomposition to a methylene complex is not accessible for $Zr(MeCp)_2Me(OMe)$ because the elimination of CH_3OH is much less favored. Our calculations show an overall endothermicity of 299 kJ/mol for this reaction and, of course, the TS (not calculated here) would be at an even higher energy. This is a plausible explanation for the better thermal stability of $Zr(MeCp)_2Me(OMe)$ over $Zr(MeCp)_2Me_2$ [5]. Precursors can therefore be designed to be more thermally stable by avoiding strong hydrogen donors and acceptors in the same molecule.

Returning to ML_2Me_2, Mulliken population analysis reveals that the reactant has a three-centre σ C(Me)-M-C(Me) HOMO with slight M:*d* character Figure 4, except in the case of $ZrMe_4$, where for symmetry reasons the highest-lying occupied orbitals are five-centre σ M-C_4. The reactant LUMO is of predominantly M:*d* character. The frontier orbitals at the TS show mixing between HOMO and LUMO; specifically, there is a shift of electron density from one C(Me) to the other C(Me) via M:*d*. In this way, the σ C(CH_4)-M bond is broken and a two-centre π M=C(CH_2) bond is formed. At the TS, the geometry around C(CH_2) suggests sp^2 hybridisation, with no remnant of the broken C-H bond visible in the electron density. The product HOMO exhibits π overlap between M:*d* and C:*p*. It seems that transfer of this electron pair by mixing of HOMO and LUMO is the critical point of the reaction and the associated energy cost dictates the activation energy. We can see therefore that electron transfer will be facilitated if the LUMO is low in energy and the M:*d* orbitals are accessible.

The electrophilicity of M and the ionic character of the M-C bond are known to increase down group 4. Our computed charges on M in the complex agree with this trend (Table 3). The calculated HOMO-LUMO energy gaps also increase down the group and, despite the systematic error in DFT energy gaps, they are a quantitative measure of hardness [34] and, indirectly, of electrophilicity. Of the group 4 metals, the Ti complex has the most *d* character in the HOMO and the lowest-lying LUMO, and so for this complex we see the lowest activation energy and predict the most facile decomposition. Based on the computed differences in E_a, the Ti complex should decompose 10^5 times faster than the Zr complex at 298 K. Although the ground state properties of most Zr and Hf compounds are nearly identical, [26] the excited states of the reactant play a decisive role in this reaction and so the higher-lying LUMO of the Hf complex leads to a higher activation energy. Thus, the Hf complex should decompose 10^3 times more slowly than the Zr complex at 298 K. We thus provide evidence for Schrock's suggestion that activation energy increases with the electrophilicity of the metal [13] .

The identity of the ligands can also affect the electrophilicity of the metal, which opens up the possibility of tuning precursor stability via the electronic properties of the ligands. Our calculations show that, relative to L = Cp, alkoxide ligands L = OMe raise the energy of the M:*d*-dominated LUMO, increase the polar character of the M-L bond and increase the effective charge on M (Table 6). Our computed increase in activation energy correlates with this increase in electrophilicity of the metal. These ligands although do not gain/lose atoms in the reaction, are not inert spectators.

The symmetry of the molecule also has an impact on the HOMO-LUMO band gap and consequently on the activation energy of the reaction. The $ZrMe_4$ reactant is of tetrahedral symmetry and its HOMO is stabilised by delocalisation over four M-C bonds (Table 6). This lower-lying HOMO for L = Me means an increase in the energy gap relative to L = Cp, increased hardness, and increased activation energy. Despite this, the symmetry of the complex opens up more degenerate unimolecular and bimolecular channels for H transfer and CH_4 elimination, and MMe_4 complexes are known to be highly unstable [17].

Analysis of the geometry and the electronic structure suggests that substantial transfer of α-H from $C(CH_2)$ to $C(CH_4)$ has already occurred at the TS, consistent with activation of the C-H bond. Although it may be proposed that this is a Brønsted acid-base reaction (namely, $2\text{-}CH_3^- \rightarrow =CH_2^{2-} + CH_4$ by transfer of H^+), we find no evidence in our calculations for changes in

the charge on H as it is transferred from reactant to TS to products. We do see evidence for the transfer of the highest-lying electron pair (HOMO) towards $M=CH_2$, along with the transfer of α-H, as presented in Figure 5. We expect that there is further electron transfer in the cyclic transition state associated with the breaking and formation of C-H bonds, although this is not visible in high-lying orbitals.

Schrock has suggested that α-H is drawn towards a "semi-bridging" position between the reacting ligands [13] This raises the issue of steric effects on the decomposition reaction. The fact that ligands are more crowded around the smaller Ti centre than in the case of Zr and Hf may increase the probability of α-H moving to the semi-bridging position. Indeed, our data show the Me-M-Me angle closing to a consistent 131-133° at the TS, which involves less distortion of the reactant in the Ti case than in the cases of Zr and Hf (Table 2). For the same reason, the large Cp ligands have an important steric effect in achieving the TS geometry and promoting unimolecular α-H transfer, rather than the bimolecular reaction that predominates for small ligands such as L = Me (Table 5) [17]. We have briefly tested the possible TS of the bimolecular reaction described in Scheme 1, Equation 2 of ref. [17] for $ZrCp_2Me_2$ but have not been able to find such a TS. Even in the case that a bimolecular TS exists, the steric effect of the Cp ligands will encourage unimolecular decomposition over bimolecular.

In the TS, the distance between M and the transferring α-H is short (1.8-2.0 Å) but we find no evidence for electron density between M and H. This can therefore be described as an α-agostic geometry (as opposed to an "agostic bond"), which is a common feature of α-C-H activation by early transition metals [35]. It is thought that the close M-H approach facilitates the breaking or making of M-C bonds.

Our calculations show that Cp ligands play an important role in stabilizing the TS, but an even greater role in stabilizing the product (Table 4, Figure 6). The elimination of a methyl group as CH_4 empties a coordination seat on the metal centre and destabilizes it. Bulky L = Cp ligands are able to partially cover this seat, while smaller spectator ligands L = Me are not.

Substituents on the Cp ring can open up the possibility of β-hydrogen abstraction. In a case of $Zr(MeCp)_2Me_2$ we have found a TS for transfer of β-hydrogen to give a 'tuck-in' complex (Equation 2, Figure 7) that has a similar activation energy to that of α-hydrogen abstraction.

A complete study of the geometric factors affecting this reaction is beyond the current scope, but it is clear that in such complexes there is competition between abstraction of hydrogens at α and β positions. The situation is complicated by the possibility that the highly reactive carbene (the product of α-hydrogen abstraction, Equation 1) may react intramolecularly with substituents on the Cp ring (*e.g.* Equation 3). Contrasting L=MeCp with L = Cp however, these reactions (Equation 2 and Equation 3) are not possible for $ZrCp_2Me_2$, which may be the primary difference in the decomposition process of those molecules.

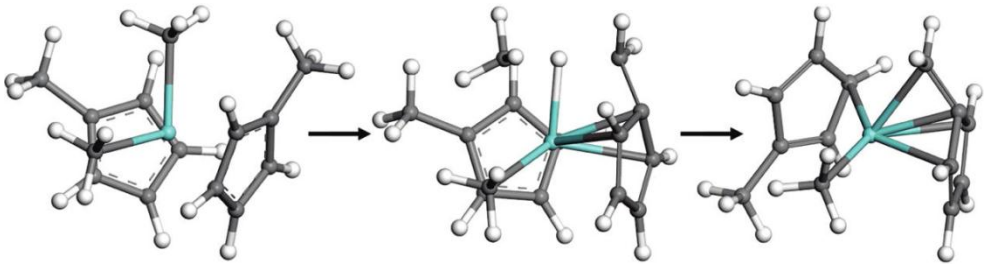


Figure 7 – Ball and stick representations of computed structures of precursor (reactant), TS and product along decomposition pathway (Equation 2) for L = MeCp, M = Zr; white = hydrogen, grey = carbon, blue = Zr.

6.5 Conclusion

The thermal stabilities of the complexes of $M(RCp)_2Me_2$ (R = H and Me) increase down the group of M = Ti, Zr and Hf. We have used density functional theory to probe a likely decomposition route (α-H abstraction) and characterize the reaction pathway. We find that the activation energy of this reaction increases with the HOMO-LUMO band gap of the reactants, which itself increases with the electrophilicity of the metal cation. The electrophilicity of the metal cation increases down group 4 and can be also influenced by spectator ligands. Examining HOMO and LUMO energies of the reactants ZrL_2Me_2 (L = Cp, OMe, Me) reveals a variety of causes for differences in electrophilicity of Zr and consequently the greater band gap when Cp is replaced by OMe and Me.

The steric effect of the Cp ligands is also visible. The bulky Cp ligands prevent a bimolecular reaction and promote the unimolecular decomposition pathway, as well stabilising the TS and the product by covering empty coordination seats. In the case of substituted Cp ligands, there may be competition with intramolecular β-H abstraction.

Our model of the decomposition pathway can be used to account for the thermal stability of molecules which undergo this reaction, such as catalysts for olefination reactions. These molecules are also used as ALD precursors, and here the model is helpful in proposing chemical modifications to enhance thermal stability, illustrating how the ALD process window can be widened by rational molecular design based on mechanistic understanding.

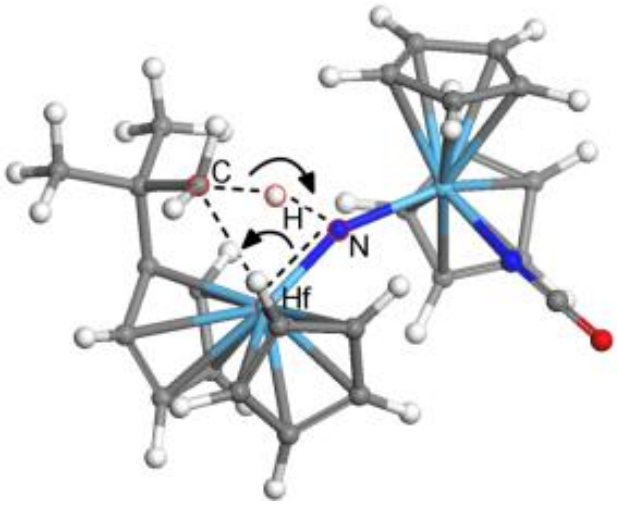
1. Wilk, G.D., R.M. Wallace, and J.M. Anthony, *High-kappa gate dielectrics: Current status and materials properties considerations.* Journal of Applied Physics, 2001. **89**(10): p. 5243-5275.
2. Suntola, T., *Atomic layer epitaxy.* Materials Science Reports, 1989. **4**(5): p. 261-312.
3. Hausmann, D.M., et al., *Atomic Layer Deposition of Hafnium and Zirconium Oxides Using Metal Amide Precursors.* Chemistry of Materials, 2002. **14**(10): p. 4350-4358.
4. Niinistö, J., et al., *Structural and dielectric properties of thin ZrO_2 films on silicon grown by atomic layer deposition from cyclopentadienyl precursor.* Journal of Applied Physics, 2004. **95**(1): p. 84-91.
5. Rushworth, S., et al., *Thermal stability studies for advanced Hafnium and Zirconium ALD precursors.* Surface and Coatings Technology, 2007. **201**(22-23): p. 9060-9065.
6. Elam, J.W., et al., *Mechanism for zirconium oxide atomic layer deposition using bis(methylcyclopentadienyl)methoxymethyl zirconium.* Applied Physics Letters, 2007. **91**(25): p. 253123.
7. Puurunen, R.L., *Surface chemistry of atomic layer deposition: A case study for the trimethylaluminum/water process.* Journal of Applied Physics, 2005. **97**(12): p. 121301.
8. Elliott, S.D. and J.C. Greer, *Simulating the atomic layer deposition of alumina from first principles.* Journal of Materials Chemistry, 2004. **14**: p. 3246-3250.
9. Ziegler, K., et al., *Das Mülheimer Normaldruck-Polyäthylen-Verfahren.* Angewandte Chemie, 1955. **67**(19-20): p. 541-547.
10. Tebbe, F.N., G.W. Parshall, and G.S. Reddy, *Olefin homologation with titanium methylene compounds.* Journal of the American Chemical Society, 1978. **100**(11): p. 3611-3613.
11. Petasis, N.A. and E.I. Bzowej, *Titanium-mediated carbonyl olefinations. 1. Methylenations of carbonyl compounds with dimethyltitanocene.* Journal of the American Chemical Society, 1990. **112**(17): p. 6392-6394.
12. Hughes, D.L., et al., *Mechanistic Study of Ester Olefinations Using Dimethyltitanocene.* Organometallics, 1996. **15**(2): p. 663-667.
13. Schrock, R.R., *Alkylidene complexes of niobium and tantalum.* Accounts of Chemical Research, 1979. **12**(3): p. 98-104.
14. de Frémont, P., N. Marion, and S.P. Nolan, *Carbenes: Synthesis, properties, and organometallic chemistry.* Coordination Chemistry Reviews, 2009. **253**(7-8): p. 862-892.
15. Schrock, R.R., *High Oxidation State Multiple Metal−Carbon Bonds.* Chemical Reviews, 2001. **102**(1): p. 145-180.
16. Davidson, P.J., M.F. Lappert, and R. Pearce, *Metal σ-hydrocarbyls, MRn. Stoichiometry, structures, stabilities, and thermal decomposition pathways.* Chemical Reviews, 1976. **76**(2): p. 219-242.
17. Wu, Y.-D., et al., *Computational and Experimental Studies on the Thermolysis Mechanism of Zirconium and Hafnium Tetraalkyl Complexes. Difference between Titanium and Zirconium Complexes.* Organometallics, 1999. **18**(11): p. 2081-2090.
18. Schrock, R.R., *On the trail of metathesis catalysts.* Journal of Organometallic Chemistry, 1986. **300**(1-2): p. 249-262.
19. Alt, H.G., et al., *Automated thermal degradation studies on solid σ-organotransition metal complexes: Dimethyl-titanocene, -zirconocene and -hafnocene.* Journal of Organometallic Chemistry, 1976. **107**(2): p. 257-263.
20. McDade, C., J.C. Green, and J.E. Bercaw, *A kinetic and mechanistic study of the thermolysis of bis(pentamethylcyclopentadienyl)dimethyltitanium(IV).* Organometallics, 1982. **1**(12): p. 1629-1634.
21. Bulls, A.R., et al., *Intramolecular carbon-hydrogen bond activation of benzyl ligands by metalated cyclopentadienyl derivatives of permethylhafnocene. Molecular structure of (η^5-C_5Me_5)(η^5,η^1-$C_5Me_4CH_2$)$HfCH_2C_6H_5$ and the mechanism of rearrangement to its*

hafnabenzocyclobutene tautomer cyclic (η^5-$C_5Me_5)_2Hf(o$-$CH_2C_6H_4)$. Organometallics, 1987. **6**(6): p. 1219-1226.
22. Schrock, R.R. and G.W. Parshall, *σ-Alkyl and -aryl complexes of the group 4-7 transition metals.* Chemical Reviews, 1976. **76**(2): p. 243-268.
23. Davidson, P.J., M.F. Lappert, and R. Pearce, *Silylmethyl and related complexes II. Preparation, spectra, and thermolysis of the tetraneopentyls of titanium, zirconium, and hafnium.* Journal of Organometallic Chemistry, 1973. **57**(2): p. 269-277.
24. Beckhaus, R. and C. Santamaría, *Carbene complexes of titanium group metals -- formation and reactivity.* Journal of Organometallic Chemistry, 2001. **617-618**: p. 81-97.
25. Mar'in, V.P., L.I. Vyshinskaya, and G.A. Razuvaev, *Thermal decomposition and photodecomposition of biscyclopentadienyl complexes of titanium, vanadium, and their analogues.* Russian Chemical Reviews, 1989. **58**: p. 494-506.
26. Zheng, W., et al., *Electronic Structure Differences in ZrO_2 vs HfO_2.* The Journal of Physical Chemistry A, 2005. **109**(50): p. 11521-11525.
27. Ahlrichs, R., et al., *Electronic-Structure Calculations On Workstation Computers - The Program System Turbomole.* Chemical Physics Letters, 1989. **162**(3): p. 165-169.
28. Eichkorn, K., et al., *Auxiliary basis sets to approximate Coulomb potentials (Chem. Phys. Letters 240 (1995) 283).* Chemical Physics Letters, 1995. **242**(6): p. 652-660.
29. Eichkorn, K., et al., *Auxiliary basis sets for main row atoms and transition metals and their use to approximate Coulomb potentials.* Theoretical Chemistry Accounts: Theory, Computation, and Modeling (Theoretica Chimica Acta), 1997. **97**(1): p. 119-124.
30. Sierka, M., A. Hogekamp, and R. Ahlrichs, *Fast evaluation of the Coulomb potential for electron densities using multipole accelerated resolution of identity approximation.* The Journal of Chemical Physics, 2003. **118**(20): p. 9136-9148.
31. Schafer, A., H. Horn, and R. Ahlrichs, *Fully optimized contracted Gaussian basis sets for atoms Li to Kr.* The Journal of Chemical Physics, 1992. **97**(4): p. 2571-2577.
32. Andrae, D., et al., *Energy-adjustedab initio pseudopotentials for the second and third row transition elements.* Theoretical Chemistry Accounts: Theory, Computation, and Modeling (Theoretica Chimica Acta), 1990. **77**(2): p. 123-141.
33. Piper, T.S. and G. Wilkinson, *Alkyl and aryl derivatives of π-cyclopentadienyl compounds of chromium, molybdenum, tungsten, and iron.* Journal of Inorganic and Nuclear Chemistry, 1956. **3**(2): p. 104-124.
34. Chattaraj, P.K., U. Sarkar, and D.R. Roy, *Electrophilicity Index.* Chemical Reviews, 2006. **106**(6): p. 2065-2091.
35. Berkaine, N., P. Reinhardt, and M.E. Alikhani, *Metal (Ti, Zr, Hf) insertion in the C-H bond of methane: Manifestation of an agostic interaction.* Chemical Physics, 2008. **343**(2-3): p. 241-249.

Chapter 7. C-H bond activation by rotational electron pair exchange in metallocene complexes.

This chapter has been prepared for submission.

For this chapter I did the calculations, the analysis and the writing with some assistance of Dr. Simon Elliott.



We used DFT to study the mechanism of C-H bond activation via 1,2 addition across a multiple metal-ligand bond in early transition metal metallocene complexes (M = Hf, Zr and X = N, C). The aim of this work is to understand orbital interactions, how bonds break and how new bonds form, and in what state hydrogen is transferred during the reaction. Calculations reveal two synchronous and concerted electron transfers within a four-membered cyclic transition state in the plane between the cyclopentadienyl rings, one π(M=X)-to-σ(M-C) involving metal *d* orbitals and the other σ(C-H)-to-σ(X-H) mediating the transfer of neutral H. The net effect of rotational electron pair exchange is cleavage of C-H and group transfer. These insights into C-H activation by transition metal complexes will help the rational design of hydrocarbon catalysts.

7.1 Introduction

The activation and functionalization of C‑H bonds is an active field of current chemical research, motivated by the desire to make more effective use of cheap and abundant simple hydrocarbons as feedstocks for chemical synthesis [1, 2]. Homogenous catalysis mediated by transition metal complexes is one of the most efficient ways to break the C-H bond. In this case, the main mechanisms identified are oxidative addition, electrophilic substitution, σ-bond metathesis and 1,2-addition, where the last two are relevant for early transition metals (M) and particularly their metallocene complexes. This paper looks at 1,2-addition, a reaction similar to group transfer within organometallic complexes [3] and to pericyclic group transfers such as the Ene reaction [4, 5].

In the 1,2-addition reaction the C-H bond is cleaved when it adds across a multiple metal-ligand bond (M = X, where X is imido or alkylidene), giving a net change in bond order of +1 and -1 for σ and π respectively [4, 5]. It was reported by Cummins [6] and Bergman [7] that Zr(IV) amido alkyl complexes could undergo 1,2 elimination of alkane to generate the corresponding transient imido complexes, which then underwent addition of CH bonds, including alkanes across the Zr-N linkage. Legzdins has developed a rich chemistry involving the formally analogous addition of C–H bonds of hydrocarbons, including alkanes, across Mo=C or W=N bonds [8]. This reaction has been described as an electrophilic addition where the M=X π-bonding electrons act as the base, accepting the proton of the adding C-H bond, [9] which presupposes that H is transferred as a proton.

C-H bond activation reaction has also been studied computationally [4, 10-12] Application of Density Functional Theory (DFT) has provided good insights into geometry and energy. C-H bond addition across the M=N bond of group 4 transition metals has been investigated theoretically by Cundari, Wolczanski and co-workers [11, 13]. They found significant bond breaking occurring within a constrained, unimolecular transition state (TS), supporting a planar geometry for C-M-N-H in the TS. A detailed theoretical study of C-H activation of methane by a titanium-imido complex [$(Me_3SiO)_2Ti(NSiMe_3)$] was presented by Noriaki *et al*., [14] focussing on total charge density, energetics of the reaction and orbital interactions, using different methods (MP2, MP3, MP4, CCSD and DFT).

The mechanism of C-H bond activation by M has been explained[14] as being governed by a general mechanism involving two synergistic transfers of electron density. The first is σ-donation from the bonding σ(C-H) molecular orbital (MO) into a symmetry adapted vacant MO on M. The second transfer is π-back-donation from an occupied M:d_π MO into an anti-bonding σ*(C-H) MO. Both of these electron transfers should weaken and eventually cleave the σ(C-H) bond [4, 10, 14]. In addition, a computed decrease in the charge on H has been interpreted as heterolytic cleavage. [10, 14, 15] The aim of this work is to understand orbital interactions in C-H activation, how bonds break and how new bonds form, and in what state hydrogen is transferred during the reaction. Furthermore, we examine to what extent C-H activation in Hf and Zr metallocenes follows the general mechanism of C-H bond activation described in the literature [4].

Experimentally, C-H bond activation was observed and documented by Chirik and co-workers where a hafnium dimer complex $((Me_2Si,\eta^5\text{-}C_5Me_4)(\eta^5\text{-}C_5H_3\text{-}3\text{-}^t\text{Bu})Hf)_2(\mu_2,\eta^2,\eta^2\text{-}N_2)(2\text{-}N_2)$, which we denote Hf_2N, was treated with a stoichiometric quantity of CO [16]. The solid-state structure confirms N-N cleavage with formation of an isocyanate (NCO) ligand and a bridging imido (μ-NH) in near–linear disposition between the two hafnium canters. The hydrogen atom of μ-NH comes from cyclometallation of the tert-butyl group, i.e. through breaking a C-H bond. Thus, N_2 cleavage is coupled with N-C bond formation and hydrocarbon C-H bond activation. This sequence of steps in the reaction pathway has been studied using DFT, [17] supporting and extending the mechanism proposed by Chirik and co-workers. It was shown that addition of CO to the Hf_2N complex ultimately facilitates intramolecular C-H bond activation in the ^{t}Bu substituent.

7.2 Computational Section

All the molecules in this analysis were modelled as isolated molecules in vacuum. The ground state electronic wavefunction of each molecule was calculated self-consistently within Kohn-Sham DFT using the TURBOMOLE suite of quantum chemical programs [18]. All species reported here were closed shell but open shell tests were also carried out. Unconstrained optimization of the molecular geometry was carried out on the DFT potential energy hypersurface. Vibrational analysis was performed at the transition state in order to characterize the nature of the stationary point. A good trade-off between accuracy and compu-

tational cost was obtained by using the B-P86 functional, the RI approximation, [19-21] and the atom-centered SV(P) basis set [22] with effective core potentials of 28 electrons on Zr and of 60 electrons on Hf [23].

7.3 Results and Discussions

The 1,2-addition of C-H to the Hf=N bond is presented in Figure 1. It appears to be similar to the α-hydrogen abstraction reaction that we have previously studied in $Zr(C_5H_5)_2Me_2$ [24] and which may be essentially the reverse of a 1,2-addition reaction. We are therefore interested to find out whether the same mechanism operates for 1,2 addition of the ^{t}Bu C-H across Hf=N in the Hf_2 complex as for 1,2-addition of methane C-H across Zr=C in the simpler Zr complex. Experimental characterisation of the TS is limited and computational modelling plays a central role in providing insight into these reactions, revealing directly the changes in atomic and electronic structure. We use DFT in this study to analyse the mechanism of C-H bond activation where the C-H bond undergoes 1,2-addition across an unsaturated M=X bond (where M = Hf and Zr; X = C and N).

In order to obtain insight into the mechanism, we computed the reactant, TS and product of the reaction and analysed their electronic structure by visualizing MOs and using Mulliken population analysis. We focus on those orbitals that are directly involved in the reaction and on the total charge on the C, M, X and H atoms forming the four-membered, planar cyclic TS, which we call the “active atoms”.

A detailed account of geometry and energy for Chirik’s complex along the C-H bond activation pathway has been given previously [17]. The calculated activation energy was E_a = 91.2 kJ/mol and the overall ΔE of the reaction was -37 kJ/mol [17]. It has also been shown that the solvent does not have important effect on calculated energies of this reaction.[17] Furthermore, a detailed analysis of geometry and energies along the reaction pathway for MCp_2Me_2, where M = Ti, Zr and Hf, as well as for $ZrMe_4$ and $ZrMe_2(OMe)_2$ has been presented previously [24] . In our model compounds we replace the ligands $L_{1,3}$ = (Me_2Si,η^5-C_5Me_4) and $L_{2,4}$ = (η^5-C_5H_3-3-^{t}Bu) from the Chirik complexes with L_1 = C_5H_4 ^{t}Bu and $L_{2\text{-}4}$ = C_5H_5, to facilitate calculations and analysis.

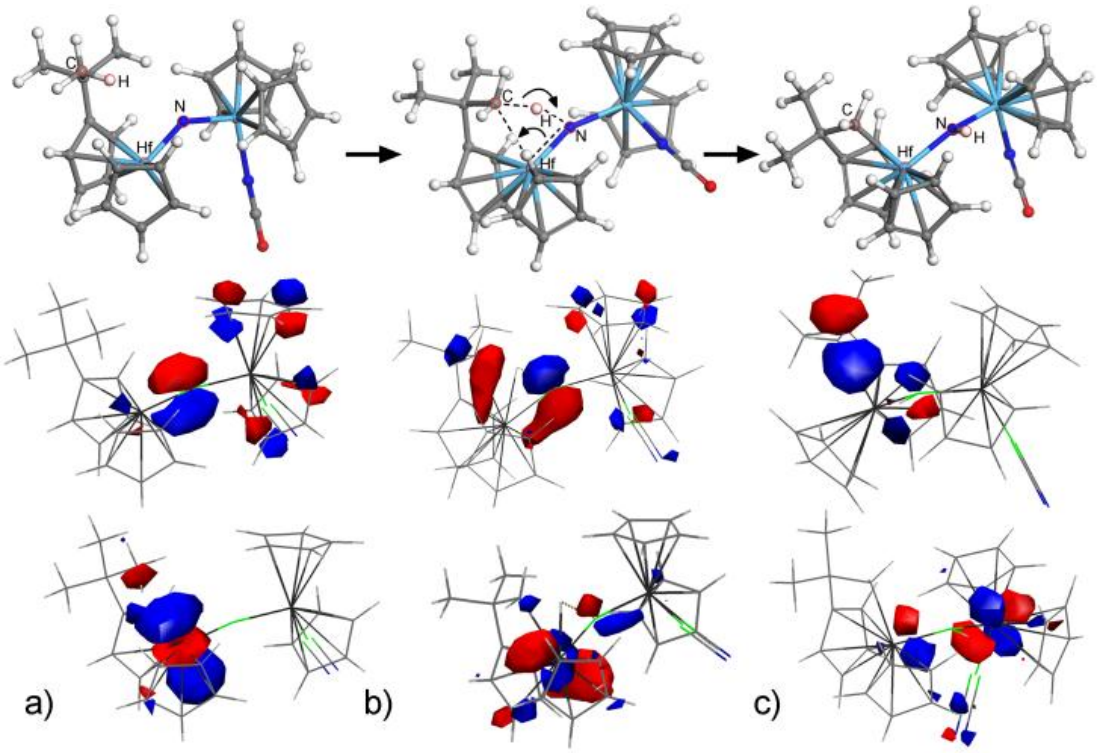


Figure 1 Computed atomic and electronic structure of (a) reactant, (b) TS and (c) product along the reaction pathway of C-H bond activation (1,2 addition of C-H bond to Hf=N bond) in model Hf_2N complexes ($L_1 = C_5H_4{}^tBu$, $L_{2\text{-}4} = C_5H_5$). First row presents structures with white = H, grey = C, pale blue = Hf, dark blue = N, red = O. The second row presents isosurface plots of high-lying M:*d*-derived orbitals: (a) HOMO-1 of reactant, (b) HOMO-1 of TS and (c) HOMO of product. The third row presents: (a) LUMO of reactant (b) LUMO of TS (c) LUMO of product along the same reaction pathway.

The electronic structure of $M(C_5H_5)_2$ metallocenes is well known. If the molecular axis is defined as z, then the lowest M-derived molecular orbital (MO) is a non-bonding degenerate pair with lobes in the x-y plane, e.g. $d_{xy}+d_{x2\text{-}y2}$. These MOs are vacant for d^0 cations such as M = Hf^{4+} and Zr^{4+} and available for bonding with nucleophilic ligands. Using x and y as the bonding axes, σ-donor ligands such as CH_3 cause occupation of d_{y2}, while π-donors, such as X = NH, donate density into d_{xy}. Either interaction breaks the symmetry of the metallocene and lifts the degeneracy of the x-y MOs.

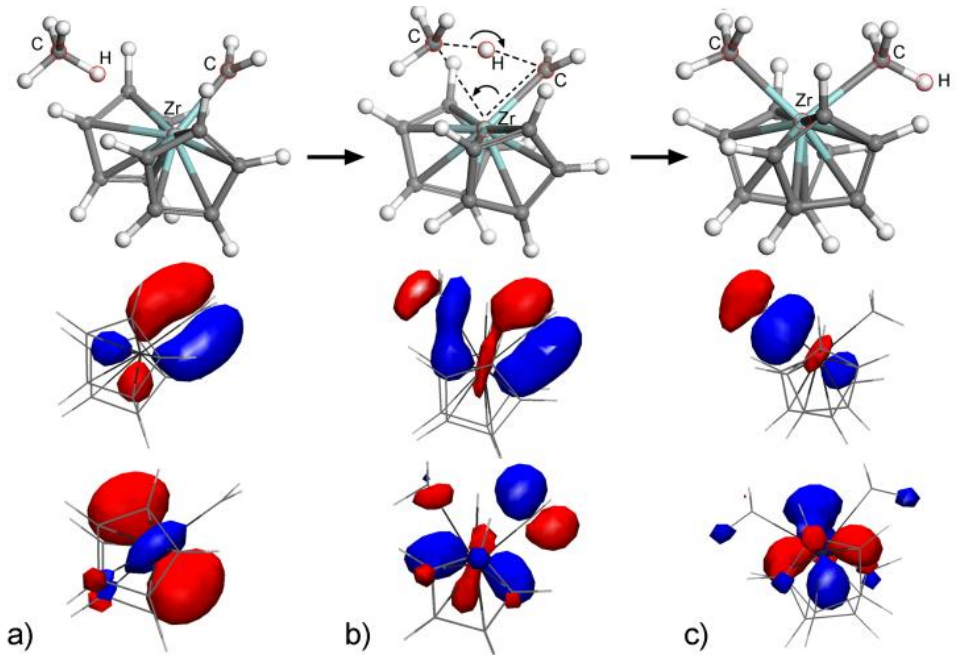


Figure 2 Computed atomic and electronic structures of (a) reactants, (b) TS and (c) product along the reaction pathway of C-H bond activation in Zr complex (1,2 addition of C-H bond to Zr=C bond). First row presents structures, where white = H, grey = C, pale blue = Zr. The second row presents isosurface plots of (a) HOMO of reactant, (b) HOMO of TS and (c) HOMO of product. The third row presents: (a) LUMO of reactant (b)LUMO of TS (c) LUMO of product along the same reaction pathway.

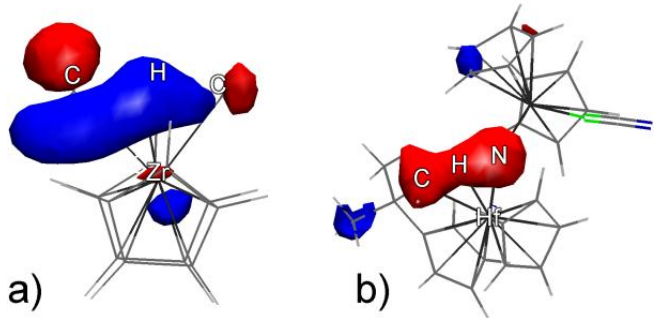


Figure 3 Isosurface plots of orbitals involved in hydrogen transfer in the computed transition state of C-H bond activation reaction in a) Zr complex and b) Hf_2N complex. See Figure 1b and Figure 2b for detailed atomic structures.

Computation of the reaction pathway for Hf_2N (Figure 1) yields similar results as previously obtained for the Zr complex (Figure 2). 1,2-addition proceeds via a four-membered TS. A CH_3 group of ^{t}Bu bends towards the Hf centre and the C-Hf-N angle becomes smaller. We see that at the TS, hydrogen is being transferred from CH_3 of ^{t}Bu group (|C-H| = 1.47 Å) to

the nitrogen (|N-H| = 1.41 Å) (Table 1), while the carbon of the CH_3 group moves to coordinate to Hf, leading to the product shown in Figure 1. The four atoms involved in the reaction – Hf, N, C of CH_3 and H of CH_3 – are co-planar in the TS. The C-Hf-N angle is 77° and the C-H-N angle is 160°. The calculated activation energy is E_a = 71 kJ/mol and the reaction leads to a more stable complex with an overall ΔE = -37 kJ/mol.

We analysed the electronic structure of the reactant, TS, and product by visualizing MOs. Figure 3 shows the orbitals involved in hydrogen transfer. At the TS, no substantial charge density is seen between Hf and H or between Hf and σ(C-H), and no σ-donation into an M-derived vacant orbital [4]. Indeed, we find no orbital spanning the entire four-membered cyclic TS. One set of orbitals shows an electron pair shifting from CH_3 of ^{t}Bu to N in tandem with the motion of H (Figure 3b). However this is not a heterolytic splitting of the C-H bond [14] because, at the TS, the wavefunction lobe is seen to be spread between C, H and N.

Table 1 Selected distances (Å) and angles (°) of the DFT optimized structures of Hf_2N (Reactant), TS and Product according to the reaction pathway shown in Figure 1.

Structural parameter	Reactant	TS	Product
Hf-N [Å]	1.95	1.98	2.11
Hf-C(CH_3) [Å]	3.86	2.52	2.34
Hf-H [Å]	3.30	1.98	2.49
C(CH_3)-H [Å]	1.10	1.47	3.75
H-N [Å]	3.15	1.41	1.03
C-Hf-N [°]	77.3	77.2	101.9
C-H-N [°]	127.7	160.4	65.6

Population analysis shows a slight increase in positive charge on H at TS (Table 2), but still within the range that can be attributed to neutral H. This small increase in positive charge at TS may reflect the ionic character of H-N in the product rather than heterolytic character of the reaction. Hydrogen is therefore neither transferred as a hydride (H^-) nor as a proton (H^+), but rather as neutral H. Nevertheless, no spin-unpaired radicals are produced: our cal-

culations show that the lowest energy structures are closed shell singlets, as the electron pair is transferred from σ(C-H) to σ(H-N).

We show in Figure 1 the orbitals which are directly involved in the synergistic transfer of the second electron pair. Mulliken population analysis of the reactant shows that the highest occupied molecular orbital (HOMO; not shown here) has only N:*p* character, while the HOMO-1 (Figure 1a) has significant Hf:d_{xy} character as well, consistent with π(Hf=N). The lowest unoccupied molecular orbital (LUMO) of the reactant is predominantly Hf:d_{y2} (Figure 1a). At the TS we see HOMO-1 and LUMO mixing (Figure 1b), so that the electron density shifts from N to C(CH_3), with negligible H character, retaining Hf character but rotating between d orbitals in the x-y plane. The product HOMO is of predominantly C(CH_3):*p* and Hf:*d* character as well as some N:*p* (Figure 1c). The symmetry of this change is consistent with donation of π(Hf=N) into a vacant σ*(C-H), as proposed, 4 but in fact there is little evidence for a contribution from σ*(C-H) in the reactant LUMO or product HOMO. Instead, the lower-lying Hf:*d* orbitals seem to play the central role. The initially vacant Hf:d_{y2} is at right angles to the occupied Hf:$d_{\pi xy}$, and this dictates the optimum angle of approach for C from the ^{t}Bu group relative to the weakening Hf=N (actually 77°). The activation energy presumably reflects the geometric strain in the TS which arises from mixing of HOMO-1 and LUMO along with contributions from the energetic and geometrical requirements for hydrogen transfer.

The 1,2 addition of C-H to Hf=X described above for X = N has the same characteristics as the α-hydrogen abstraction reaction in $Zr(C_5H_5)_2Me_2$ (Figure 2), albeit in reverse, where methane undergoes 1,2 addition across $Zr{=}CH_2$, i.e. X = C. The mechanism of α-hydrogen abstraction is described in more detail in our previous study including the effect of metal cation and spectator ligands [24]. Comparing Figure 1 with Figure 2, we see that at the TS in both cases there is a shift of electron density from an occupied orbital of M:$d_{\pi xy}$+X:p_{π} character to the LUMO with M:$d_{\sigma y2}$ character. This electron pair transfer happens via the metal and enforces an 81° C-Zr-X angle at the TS. At the same time another electron pair is transferred from C to X via H (C-H-C angle = 169°), although here there is some evidence of agostic donation into Zr:*d*, seen both in MO plots and population analyses. Electron density is spread across C-H-X, effecting "activation" of neutral H. The computed energetics for methane addition to the Zr complex are E_a = 27 kJ/mol and ΔE = -120 kJ/mol.

Table 2 Total Charge *q* of active atoms: M, C, H, X, where M = Ti, Zr, Hf and X = C, N from Mulliken Population Analysis.

		Reactant	TS	Product
$TiCp_2CH_2$	*q*[Ti]	0.35	-0.02	0.17
	q[C]	-0.50	-0.48	-0.50
X = C	*q*[X]	-0.53	-0.42	-0.50
	q[H]	0.13	0.18	0.11
$ZrCp_2CH_2$	*q*[Zr]	0.41	0.17	0.56
	q[C]	-0.50	-0.61	-0.67
X = C	*q*[X]	-0.46	-0.48	-0.67
	q[H]	0.13	0.15	0.14
$HfCp_2CH_2$	*q*[Hf]	0.49	0.25	0.62
	q[C]	-0.50	-0.67	-0.72
X = C	*q*[X]	-0.51	-0.54	-0.72
	q[H]	0.13	0.17	0.15
Hf_2N	*q*[Hf]	0.59	0.56	0.66
	q[C]	-0.40	-0.57	-0.51
X = N	*q*[X]	-0.66	-0.75	-0.81
	q[H]	0.15	0.27	0.37

Table 2 presents the total charge on "active atoms": C, M, X, H, where M = Ti, Zr, Hf and X = C, N along the C-H bond activation reaction. For $TiCp_2(CH_2)$, $ZrCp_2(CH_2)$ and $HfCp_2(CH_2)$ the electron density on the metal increases upon going to the TS, which means that the total charge on M becomes more negative. The biggest change between reactant and TS is seen for the Ti-carbene complex (Δq = -0.37), followed by the Zr and Hf-carbene complexes (Δq = -0.24) and the smallest for the Hf-imido complex (Δq = -0.03). We correlate these changes with electron pair transfer from the π(M=X) bond to the σ(M-C) bond via involvement of a metal d orbital (Figure 2a LUMO becomes Figure 2b HOMO). We think that the ionicity of the M-X interaction has an impact on how q[M] changes. The more ionic Hf cation shows less π character in Hf=N and thus less accumulation of charge on M at the TS, when compared to less ionic Ti. As the reaction proceeds from TS to product we again see that elec-

tron density on the metal decreases (q increases) due to formation of a new, single σ(M-C) bond from *dπ-pπ* of the M=X bond.

We observe an insignificant change in electron density on H at the TS for the Hf-imido complex (Δq = 0.12) and the M-carbene complexes (Δq ≤0.05). As we have mentioned above, the σ(C-H) bond is transferred to the σ(X-H) bond and this transfer is mediated by the H atom (Figure 3). At the TS the electron density is spread between C, H and X atoms. The bonding environment around H changes very little for M-carbene complexes (C-H to C-H) and in case of Hf_2N (C-H to N-H). In addition, we can expect some influence of the metal on the σ(C-H) bond character. Figure 3 shows a small contribution to this bond from Zr in the Zr-carbene complex, but very little from Hf in the Hf-imido complex. Mulliken Population Analysis shows an increase in charge density on C(CH_4) or C(CH_3) along the reaction in most of the cases, except in the Ti-carbene complex. At TS ligands exchange an electron pair via the metal centre. Electron density on the C at TS will depend on a balance between electron pair exchange. These results of charge distribution across the active atoms are consistent with our understanding of the mechanism from orbital plots.

In our work we investigated C-H activation within a hafnium-imido complex (Figure 1), using DFT methods. The changes in orbitals and atomic charge along the reaction pathway (Table 2), show similar trends to Noriaki's DFT result which was validated against more accurate methods and which indicates that our choice of method, model, and results is justified. Furthermore, different density functional (BP86, B3LYP, BLYP and PW91), RHF (restricted Hartree-Fock), and MP2 (Møller-Plesset second-order perturbation theory) methods yielded little difference in calculations for a reaction of CH bond activation by titanium imido complexes [11, 14].

The mechanism that we describe, however, differs in some respects from that described in the literature. We see no evidence for heterolytic cleavage of C-H. The primary observation is that σ(C-H) transforms into σ(H-X) as shown in Figure 3 which is also supported by the charge distribution (Table 2). The interaction of σ(C-H) with vacant metal-derived orbitals does not seem to be a necessary condition, being slight for Zr and absent for Hf (Figure 3), in contrast to one of the general characteristics proposed in the literature. Likewise, the involvement of σ*(C-H) appears to be slight. Instead, rotation between M:*d* orbitals in the

plane of the TS dominates the change from π(M=X) to σ(M-C). Our data show that the description of M=X π-bonding electrons as a base and C-H as an acid is not relevant for this reaction. Otherwise, however, there is a good agreement with previous works: a planar four-membered cyclic TS is formed as the two electron pairs are transferred in a synchronous and concerted manner.

7.4 Conclusion

We have examined the changes in the electronic structure underlying C-H cleavage via 1,2-addition across a multiple metal-ligand bond in early transition metal metallocene complexes (M = Hf, Zr and X = N, C). In a departure from previous reports, our calculations show the transfer of neutral H as σ(C-H) transforms into σ(H-X) without interacting substantially with M, and show no major role for σ^*(C-H). The reaction proceeds via a four-membered, planar cyclic TS, with internal C-M-X angle of slightly less than 90°, consistent with the change in orientation of the M:*d* contribution from π(Hf=X) to σ(Hf-C). The mechanism of C-H bond activation can be described as Rotational Electron Pair Exchange, where electrons originate as σ(C-H) and π(M=X) and end up as σ(H-X) and σ(M-C) respectively. These insights into C-H activation by transition metal complexes will help the rational design of hydrocarbon catalysts.

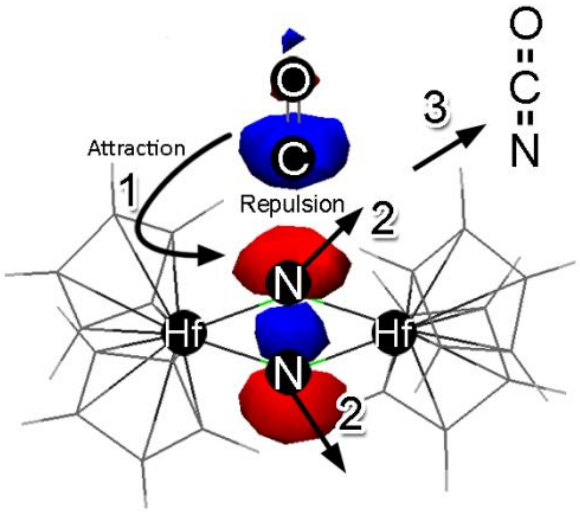
1. Bergman, R.G., *Organometallic chemistry: C-H activation.* Nature, 2007. **446**(7134): p. 391-393.
2. Labinger, J.A. and J.E. Bercaw, *Understanding and exploiting C-H bond activation.* Nature, 2002. **417**(6888): p. 507-514.
3. Mullins, S.M., R.G. Bergman, and J. Arnold, *Olefination and group transfer reactions of an electron deficient tantalum methylidene complex.* Dalton Transactions, 2006(1): p. 203-212.
4. Balcells, D., E. Clot, and O. Eisenstein, *C—H Bond Activation in Transition Metal Species from a Computational Perspective.* Chemical Reviews, 2010. **110**(2): p. 749-823.
5. Hoyt, H.M., F.E. Michael, and R.G. Bergman, *C−H Bond Activation of Hydrocarbons by an Imidozirconocene Complex.* Journal of the American Chemical Society, 2004. **126**(4): p. 1018-1019.
6. Cummins, C.C., S.M. Baxter, and P.T. Wolczanski, *Methane and benzene activation via transient (t-$Bu_3SiNH)_2Zr$=NSi-t-Bu_3.* Journal of the American Chemical Society, 1988. **110**(26): p. 8731-8733.
7. Walsh, P.J., F.J. Hollander, and R.G. Bergman, *Generation, alkyne cycloaddition, arene carbon-hydrogen activation, nitrogen-hydrogen activation and dative ligand trapping reactions of the first monomeric imidozirconocene (Cp_2Zr=NR) complexes.* Journal of the American Chemical Society, 1988. **110**(26): p. 8729-8731.
8. Wada, K., et al., *Intermolecular Activation of Hydrocarbon C−H Bonds under Ambient Conditions by 16-Electron Neopentylidene and Benzyne Complexes of Molybdenum.* Journal of the American Chemical Society, 2003. **125**(23): p. 7035-7048.
9. Goldberg, K.I. and A.S. Goldman, *Activation and Functionalization of C-H Bonds*, in *ACS Symposium Series 885*. 2004.
10. Boutadla, Y., et al., *Mechanisms of C-H bond activation: rich synergy between computation and experiment.* Dalton Transactions, 2009(30): p. 5820-5831.
11. Cundari, T.R., T.R. Klinckman, and P.T. Wolczanski, *Carbon-Hydrogen Bond Activation by Titanium Imido Complexes. Computational Evidence for the Role of Alkane Adducts in Selective C−H Activation.* Journal of the American Chemical Society, 2002. **124**(7): p. 1481-1487.
12. Fernandez, I. and F.M. Bickelhaupt, *Alder-ene reaction: aromaticity and activation-strain analysis.* J Comput Chem, 2012. **33**(5): p. 509-16.
13. Cundari, T.R., *Methane activation by Group IVB imido complexes.* Journal of the American Chemical Society, 1992. **114**(26): p. 10557-10563.
14. Ochi, N., et al., *Theoretical study of C-H and N-H sigma-bond activation reactions by titinium(IV)-imido complex. Good understanding based on orbital interaction and theoretical proposal for N-H sigma-bond activation of ammonia.* J Am Chem Soc, 2007. **129**(27): p. 8615-24.
15. Biswas, B., M. Sugimoto, and S. Sakaki, *C−H Bond Activation of Benzene and Methane by M(η^2-$O_2CH)_2$ (M = Pd or Pt). A Theoretical Study.* Organometallics, 2000. **19**(19): p. 3895-3908.
16. Knobloch, D.J., E. Lobkovsky, and P.J. Chirik, *Dinitrogen cleavage and functionalization by carbon monoxide promoted by a hafnium complex.* Nat Chem, 2010. **2**(1): p. 30-35.
17. Zhang, X., B. Butschke, and H. Schwarz, *N_2 Activation by a Hafnium Complex: A DFT Study on CO-Assisted Dinitrogen Cleavage and Functionalization.* Chemistry – A European Journal, 2010. **16**(42): p. 12564-12569.

18. Ahlrichs, R., et al., *Electronic structure calculations on workstation computers: The program system turbomole.* Chemical Physics Letters, 1989. **162**(3): p. 165-169.
19. Eichkorn, K., et al., *Auxiliary basis sets to approximate Coulomb potentials (Chem. Phys. Letters 240 (1995) 283).* Chemical Physics Letters, 1995. **242**(6): p. 652-660.
20. Eichkorn, K., et al., *Auxiliary basis sets for main row atoms and transition metals and their use to approximate Coulomb potentials.* Theoretical Chemistry Accounts: Theory, Computation, and Modeling (Theoretica Chimica Acta), 1997. **97**(1): p. 119-124.
21. Sierka, M., A. Hogekamp, and R. Ahlrichs, *Fast evaluation of the Coulomb potential for electron densities using multipole accelerated resolution of identity approximation.* The Journal of Chemical Physics, 2003. **118**(20): p. 9136-9148.
22. Schafer, A., H. Horn, and R. Ahlrichs, *Fully optimized contracted Gaussian basis sets for atoms Li to Kr.* The Journal of Chemical Physics, 1992. **97**(4): p. 2571-2577.
23. Andrae, D., et al., *Energy-adjusted ab initio pseudopotentials for the second and third row transition elements.* Theoretical Chemistry Accounts: Theory, Computation, and Modeling (Theoretica Chimica Acta), 1990. **77**(2): p. 123-141.
24. Zydor, A. and S.D. Elliott, *Thermal Stability of Precursors for Atomic Layer Deposition of TiO_2, ZrO_2, and HfO_2: An Ab Initio Study of alpha-Hydrogen Abstraction in Bis-cyclopentadienyl Dimethyl Complexes.* The Journal of Physical Chemistry A, 2010. **114**(4): p. 1879-1886.

Chapter 8. Understanding NN cleavage and NCO formation catalyzed by group 4 metallocene complexes.

The following chapter has been prepared for submission.

For this chapter I did the calculations, the analysis and the writing with some assistance of Dr. Simon Elliott. Figure 4-6 and related analysis were done by Dr. Simon Elliott.



Cleavage of the strong, triple bond in N_2 molecule has represented a major challenge to the development of N_2 fixation chemistry. One promising recent advance has been the reductive cleavage of N_2 and functionalization to N-C at ambient temperature and pressure by means of reaction of N_2 and CO with transition metal complexes, such as those based on Hf and Zr metallocenes. Although the product is NCO^-, the reaction happens via intermediates which involve coordination of CO to the metal center. Using DFT calculations we investigated the reason why CO must coordinate to the metal center and the reason why this shows a lower energetic barrier than the alternative pathway directly along the N-N axis of the metal complex. Analysis of orbital plots reveals repulsion between occupied orbitals on CO and NN unit of the complex when CO approaches the complex along the N-N axis. These repulsions are minimized when forming an asymmetrical intermediate in which CO coordinates to one Hf and thence to N. The mechanism can be described as donation of σ(CO) and π(CO) to NN and back-donation of $\pi^*(Hf_2N_2)$ to CO, which leads to σ(NN) bond cleavage and NCO^- formation. We expect that understanding the cleavage pathway and the mechanism of functionalization will help to design new processes for the stoichiometric and catalytic fixation of nitrogen.

8.1 Introduction

Molecular nitrogen, N_2, is the most abundant source of nitrogen and is the principal source from which all nitrogen compounds are derived. The N_2 molecule, however, is inert due to its non-polarized, strong triple bond. To produce other molecules from N_2, this strong triple bond must be broken, typically either biologically via nitrogenase enzymes or industrially via the Haber-Bosch process [1-3]. The latter process is especially important for the production of artificial fertilizers but is efficient only at high temperatures and pressures. Much research is therefore directed towards developing alternative, lower-energy chemical processes to obtain organonitrogen molecules from molecular N_2 [4].

CO like N_2 also has a very strong triple bond – the strongest known in chemistry. It is an industrial gas that has many applications in bulk chemicals manufacturing. For example, a large quantity of aldehydes is produced through the use of CO and H_2. Methanol is also produced by hydrogenation of carbon monoxide. The hydrogenation of CO is coupled to C-C bond formation, as in the Fischer-Tropsch process, where CO is hydrogenated so as to obtain valuable liquid fuels from coal and natural gas.

One promising recent advance has been the reductive cleavage of N_2 and functionalization to N-C at ambient temperature and pressure by means of a reaction with CO that is catalyzed by transition metal complexes [5-7]. In this Chirik experiment, a hafnium dimer complex $((Me_2Si,\eta^5\text{-}C_5Me_4)(\eta^5\text{-}C_5H_3\text{-}3\text{-}^t\!Bu)Hf)_2(\mu_2,\eta^2,\eta^2\text{-}N_2)(2\text{-}N_2)$ was treated with a stoichiometric quantity of CO [5]. The solid-state structure confirms N-N cleavage with formation of an isocyanate (NCO^-) ligand and a bridging imido (μ-NH) in near–linear disposition between the two hafnium centers. The hydrogen atom of μ-NH comes from cyclometallation of the *tert*-butyl group, i.e. through breaking a C-H bond. Thus, N_2 cleavage is coupled with N-C bond formation and hydrocarbon C-H bond activation.

In this study we focus only on the N-N bond cleavage and N-C bond formation. The last step of the reaction, C-H bond activation, is not included. Within the N-C bond formation step, Chirik and co-workers suggested [5] that an intermediate I2 is formed according to Equation 1 (see Figure 1 for structures).

R + CO⟶I2⟶ I4 Equation 1

The sequence of steps in the reaction mechanism has been studied using Density Functional Theory (DFT) by Zhang *et al.* [8] The calculations support and extend the mechanism proposed by Chirik and co-workers [5] in the way described by Equation 2.

R + CO⟶I ⟶I2⟶TS2/3⟶I4 Equation 2

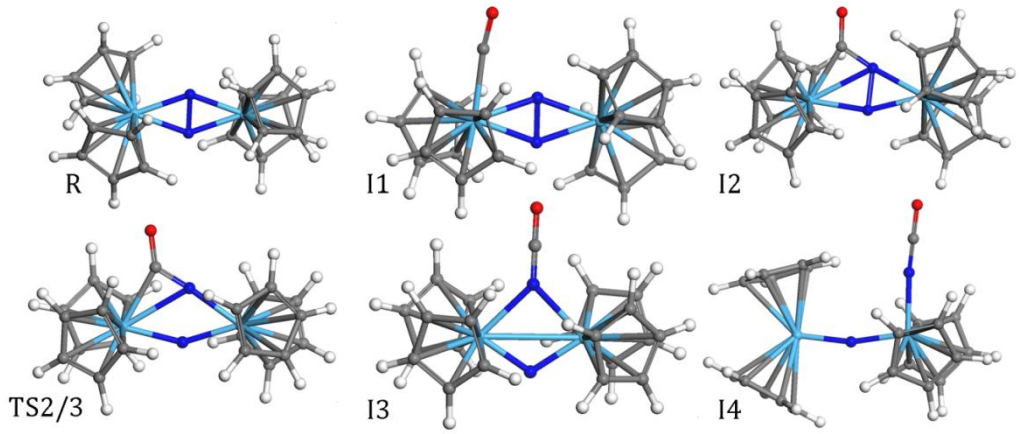


Figure 1 – Computed structures of model Hf complexes (L = Cp); white=hydrogen, grey=carbon, pale blue=hafnium, dark blue=nitrogen, red=oxygen.

The structures used here were originally proposed by Zhang *et al.* [8], where their structures (4), (5) and (9) correspond to our I1, I2 and I4 respectively (see Figure 1 and Figure 3 for L = Cp and Figure 2 for L = *ansa*Cp). The work by Zhang includes energy profiles of the N-N bond cleavage and N-C bond formation reactions as well as geometry details of the complexes. It was concluded that a large driving force for cleavage of the N-N bond comes from strain in the four membered Hf-C-N-N ring in the I2 intermediate, caused by the small Hf-C-N angle [8].

To better understand this reaction and to further develop this chemistry in order to design alternatives, it is important to know how the metal complex and CO co-reagent effect N-N cleavage at the molecular orbital (MO) level. Thus, the aim of this work is to understand the orbital interactions in this reaction so as to explain the role of the metal in facilitating N-N cleavage, and in particular why CO coordinates to the metal (intermediates I1 and I2) in order to break the last σ(NN) bond. We contrast this with the possible approach of CO along the N-N axis of the R complex to produce NCO^- directly.

We also compute and briefly explain the differences in the energy profile of the studied reaction for L = Cp and *ansa*Cp* as well as for M = Zr and Hf.

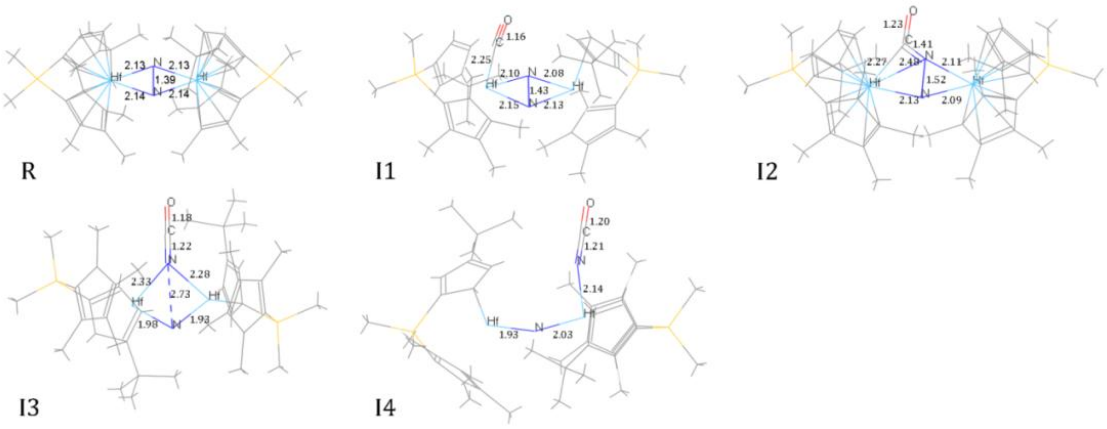


Figure 2 – Computed structures of Hf complexes for L = *ansa*Cp*

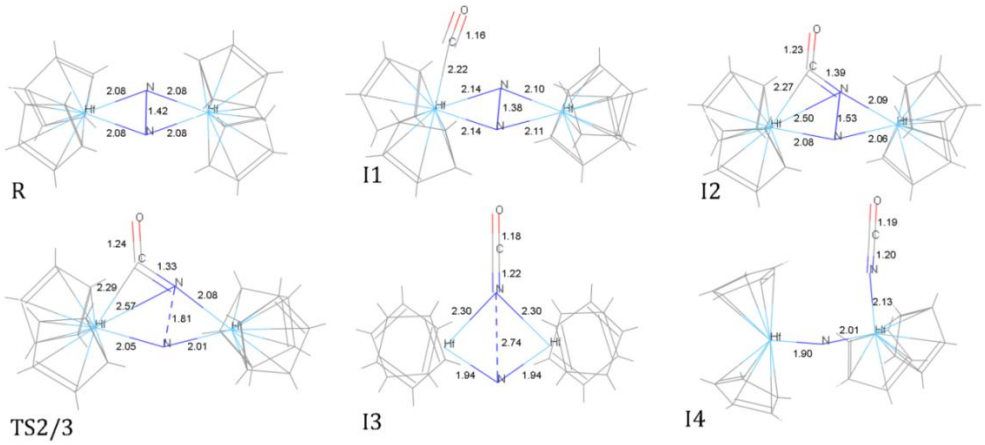


Figure 3 – Computed structures of Hf complexes for L = Cp

8.2 Computational Section

The DFT calculations were performed using the TURBOMOLE suite of quantum chemical programs [9]. All species were closed shell. Optimization of the molecular geometry was carried out on the DFT potential energy hypersurface with no constraints (except where stated). Vibrational analysis was performed for each considered structure in order to characterize the nature of the stationary point. A good trade-off between accuracy and computational cost was obtained by using the B-P86 functional, [10] the RI approximation [10-12] and

the atom-centered TZVP(P) basis set [13] with effective core potentials of 28 electrons on Zr and of 60 electrons on Hf [14]. Single point calculations with the smaller SV(P) basis set were used for population analysis. This is because SV(P) basis set yield better description of charge density. MD was carried out on the DFT hypersurface for 256 steps at 1.9 fs per step with no fixed atoms and no constraints (i.e. microcanonical ensemble). The starting geometry was the structure TS2/3 and random velocities were assigned corresponding to T = 500 K. Optimization of the final structure after 256 steps led to the new structure I3. We have not calculated the Gibbs free energy as it was done by Zhang *et al.* for L = *ansa*Cp* [8]. The corresponding potential energy surfaces were found to be similar concerning intramolecular transformations, but differ for those steps in which a CO molecule is added because of the entropic contribution. However, using Gibbs free energy did not affect the conclusions, which were based on the electronic energies. This work also included solvent effects for the crucial species I2, I4, TS2/4 for L = *ansa*Cp* and found that the energy differences were small between the gas phase and toluene solvent.

Experimental observation of the transition state (TS) is not possible due to its high instability and thus computational modeling is a valuable tool for providing insight into these reactions, directly revealing the changes in atomic and electronic structure. We used Density Functional Theory (DFT) to compute optimum structures of the reactant (R), the TS and the intermediates of the reaction (I1, I2, I3 and I4) and analyze their electronic structure through Mulliken population analysis and by visualizing MOs. To facilitate calculations and analysis we made model compounds from the Chirik complexes by replacing the two ligands $L_{1,3}$ = ((Me_2Si,η^5-C_5Me_4)(η^5-C_5H_3-3-^{t}Bu)), which we denote *ansa*Cp*, with $L_{1\text{-}4}$ = C_5H_5 = Cp. Structures were optimized separately for Zr and Hf with $L_{1\text{-}4}$ = Cp or $L_{1,3}$ = *ansa*Cp*. We also computed the experimental compound for *ansa*Cp* and carried out molecular dynamics (MD) on the transition state TS2/3. As a result, another possible intermediate was found (I3) that had not been reported previously. The updated equation of N-C bond formation is then given in Equation 3:

$$R + CO \rightarrow I1 \rightarrow I2 \rightarrow TS2/3 \rightarrow I3 \rightarrow I4 \qquad \text{Equation 3}$$

These structures and the reaction energies can be found in Figure 1, Figure 2, Figure 3, and Table 1 and are in good agreement with those computed previously [8]. Hf results for the model complex where L = Cp are discussed first.

Table 1 Δ*E* (kJ/mol) at *T* = 0 K computed with DFT for the reactions R + CO → products. The molecular structures of reactant, intermediates and products are shown in Figure 1 for L = Cp, and analogous structures can be obtained by replacing the ligands with L = *ansa*Cp* and metal (Zr or Hf).

		I1	I2	TS2/3	I3	I4
ansaCp*	Hf	-18	-49		-300	-286
ansaCp*	Zr	-11	-40		-281	-273
Cp	Hf	-55	-56	-47	-311	-256
Cp	Zr	-53	-43	-27	-303	-247

8.3 Results and Discussion

8.3.1 Hafnium dimer complex prior to reaction with CO

In the R complex with L = Cp the calculated N-N distance is 1.42 Å. Computing free N_2H_4 and N_2H_2 with the same method gives N-N distances of 1.44 Å and 1.24 Å respectively, which indicates marginally more double bond character in R than the [N_2^{4-}] single bond in free N_2H_4. Therefore, rather than being triply-bonded, N_2 has been reduced to an approximately singly-bonded state in this complex. Consistent with this, in R we can identify the filled MOs of $p\sigma$(NN), $p\pi$(NN) and $p\pi^*$(NN) character. The $p\sigma^*$(NN) MO is empty and this is the reason that the N-N single bond remains intact. The Hf-N interaction is not entirely ionic, as the Highest Occupied Molecular Orbital (HOMO) shows a significant contribution from *d*(Hf) overlapping with $p\pi^*$(NN), consistent with slight double bond character. However, as expected for Hf^{4+}, the Lowest Unoccupied Molecular Orbital (LUMO) is localised entirely on the Hf atoms. These MOs are illustrated in Figure 6 and in Figure 8 for the model compound R with L = Cp.

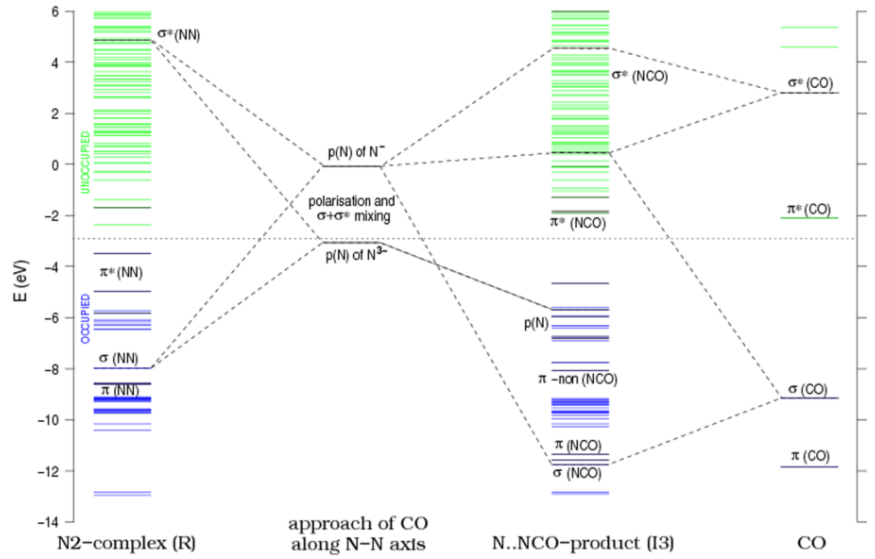


Figure 4 – MO energy level diagram for model compounds L = Cp in reaction R + CO → I3 via approach of CO along the N-N axis. Occupied and unoccupied MOs are coloured blue and green respectively, but those that are N:*p*-derived are coloured black with dashed lines showing correlation between those of *pσ* symmetry. Horizontal dots mark the Fermi level.

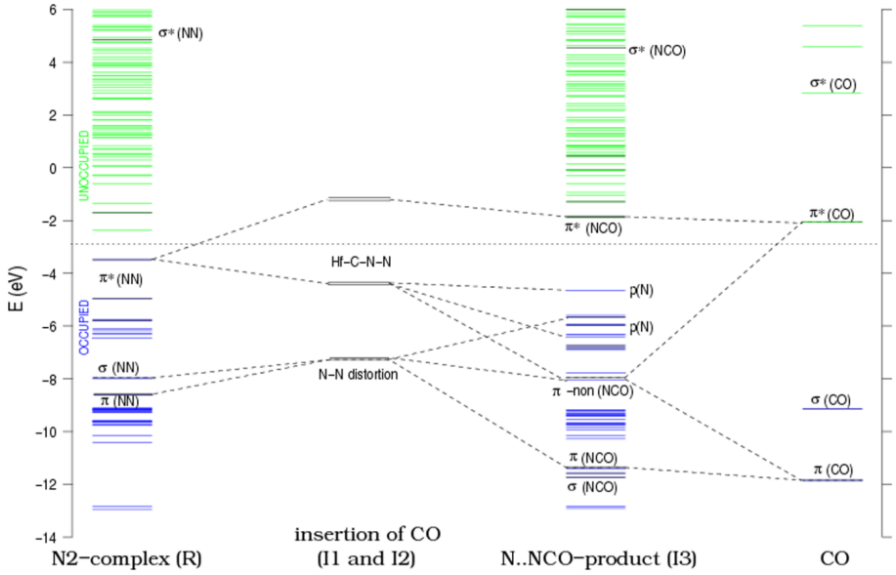


Figure 5 – MO energy level diagram for model compounds L = Cp in reaction R + CO → I1 → I2 → I3. Occupied and unoccupied MOs are coloured blue and green respectively, but those that are N:*p*-derived are coloured black with dashed lines showing pertinent correlations (σ interactions omitted for clarity – see Figure 6). Horizontal dots mark the Fermi level.

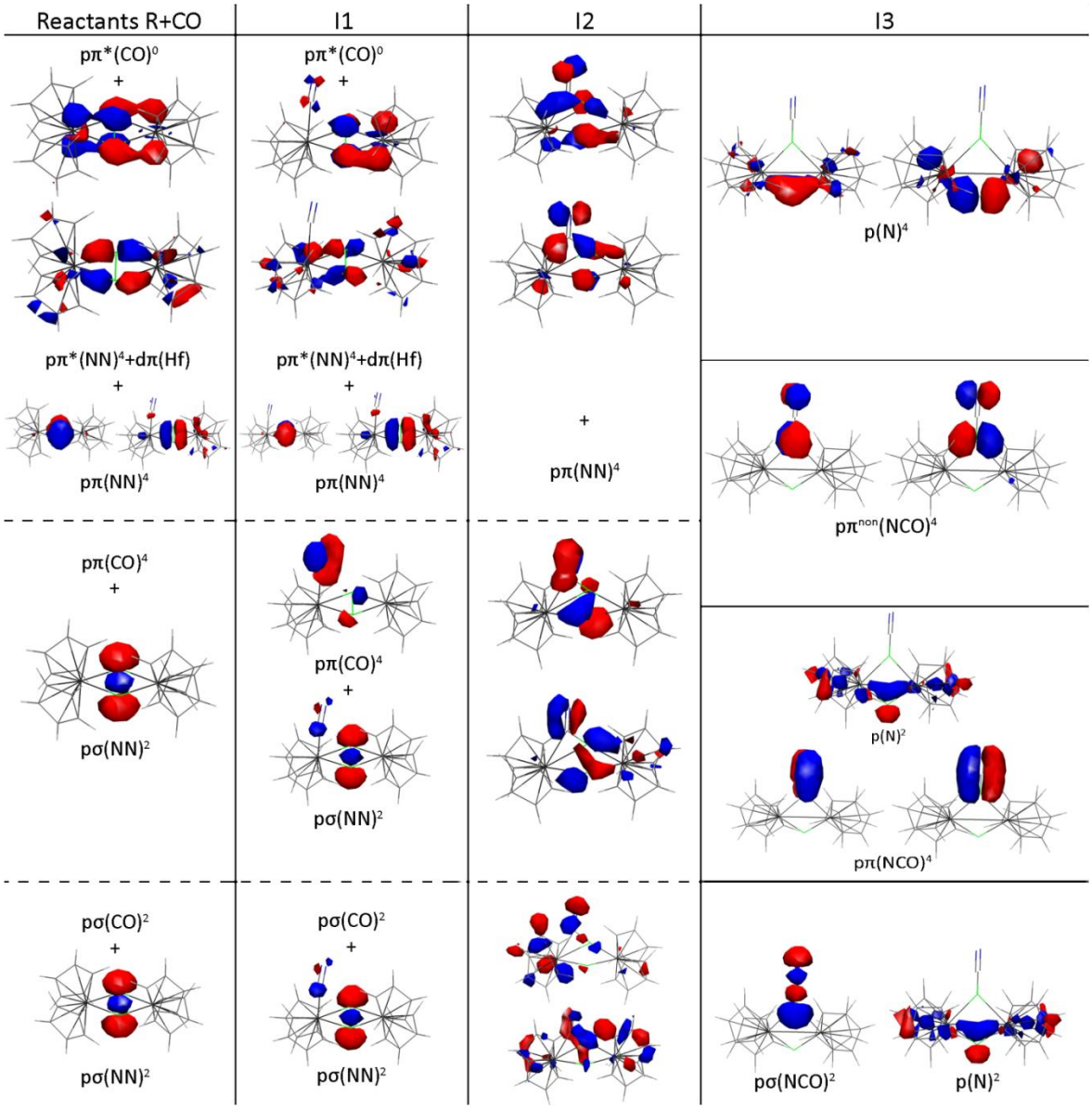
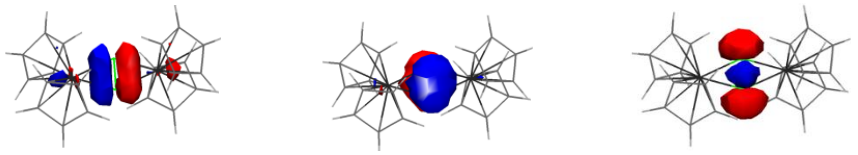


Figure 6 – How 14 of the *pσ* and *pπ* electrons from CO and N_2 undergo changes in bonding during the reaction. Selected orbitals are plotted, in some cases only one of each pair of *pπ* MOs.

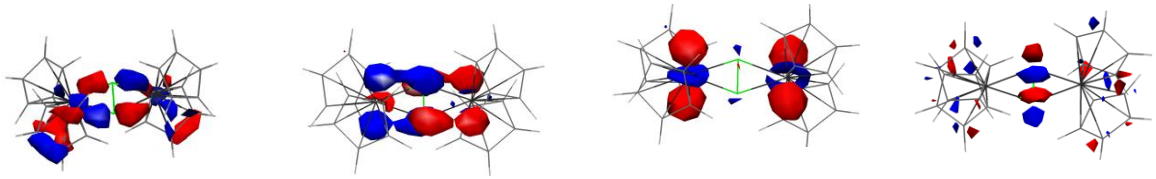


$p_y\pi^*(CO)^0$	$p_z\pi^*(CO)^0$	$p_x\sigma(CO)^2$	$p_z\pi(CO)^2$	$p_y\pi(CO)^2$
-2.0	-2.0	-9.0	-11.8	-11.8

Figure 7 – Selected MOs of CO. Orbital energies in eV.



$p_y\pi(NN)^2$	$p_z\pi(NN)^2$	$p_x\sigma(NN)^2$
-8.8	-8.7	-7.9



$p\pi^*(NN)^2+d\pi(Hf)$	$p\pi^*(NN)^2+d\pi(Hf)$	LUMO d(Hf)	virtual $p\sigma^*(NN)$
-6.3	-3.5	-2.4	+6.4

Figure 8 – Selected MOs of model compound R focusing on 10 electrons in p orbitals of $[N2]^{4-}$ and Hf (or equivalently $2N^{-} + p\sigma^2$). Orbital energies in eV.

8.3.2 Approach of CO along N-N axis

In this section we continue discussing the model Hf complexes with ligands L = Cp. CO is a neutral molecule that is both σ-donor and π-acceptor, since its HOMO is *pσ* and its LUMO is *pπ** [15]. We use constrained optimization at a series of fixed N-C distances to examine whether CO can approach along the N-N axis of model R and produce I3 directly. N-N cleavage is found to occur spontaneously at N-C distances < 1.9 Å. CO can then bond strongly with the N atom closest to it, since this can be described (for the purposes of electron counting) as a σ-acceptor and π-donor N^- anion, yielding the cyanate adduct [NCO^-] [15]. We therefore looked for a symmetric reaction pathway for CO to approach along the N-N axis of R at C-N distances > 1.9 Å. The approach of CO should cause *pσ*(NN) to be polarised,

mixing it with *p*σ*(NN), and leading ultimately to localisation of the electron pair onto an atomic *p* orbital of the more distant N atom, giving N^{3-} of I3. The interaction was found to be repulsive at C-N distances > 1.9 Å, which we suggest is associated with repulsion between the occupied *p*σ(CO) and occupied *p*σ(NN) orbitals [15] and with the high energy of the empty *p*σ*(CO) orbital. The correlation of MOs is illustrated on the MO energy diagram Figure 4. Indeed the calculations reveal an energy barrier of about 85 kJ/mol at an N-C distance of 1.9 Å.

Thus we have found that the reaction along N-N axis has an energetic barrier caused by σ repulsion. Repulsive interactions within carbonyl complexes are known to lead to structural distortion. The repulsive nature of σ-interactions was also found in high spin and electron rich transition metal monocarbonyls [16] and is the reason for the instability of the Group 1 and Group 2 monocarbonyls. This repulsion can be alleviated somewhat by decreasing the σ-overlap through bending along MCO. This suggests other possible reaction pathways of CO with Hf complexes. We now investigate whether CO faces a lower barrier when it approaches asymmetrically towards one of the Hf centers.

8.3.3 Reaction pathway for CO via metal cation

We tested the reaction pathway suggested by previous authors [8]. In the first step, CO coordinates to Hf to give I1 and the calculations yield ΔE(R + CO → I1) = -55 kJ/mol for L = Cp. From geometrical analysis (Figure 3) we see no significant change in bond length in the hafnium complex. Orbital plots indicate that the Hf-N bond is weakened but that σ(NN) is not affected (Figure 6 and Figure 9). The symmetry of the HOMO on Hf_2N_2 in R allows interaction with the π* virtual orbitals of CO and thus leads to CO coordination to Hf and N in I1. The essential change in N-N bonding happens when CO moves towards N in the I2 intermediate. In agreement with previous calculations, we find that insertion of CO into Hf-N causes the N-N bond to elongate but not to break (N-N = 1.53 Å), with a moderate release of energy (-56 kJ/mol for R + CO → I2 with L = Cp). It also significantly weakens Hf-N: the bond length increases from 2.1 Å to 2.5 Å and Mulliken population analysis shows that no electron density remains between those atoms. The bond analysis of the electronic structure for I2 is shown in Figure 6 and Figure 10. The position of CO in relation to N in I2 is such that the σ repulsion is minimized as the NCO angle is reduced to 125° with the N-C bond length of 1.4 Å. This acts in a similar way to the bending in MCO complexes that is mentioned above [16]. At the same time, we observe that electronic energy can be gained through mixing of

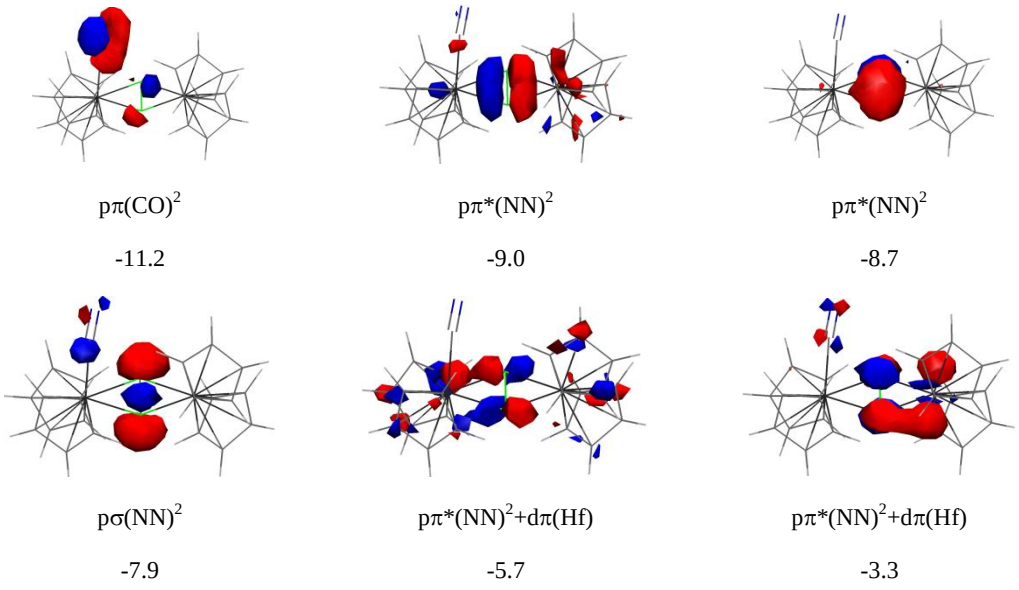


Figure 9 – Selected MOs of intermediate I1, where CO bonds directly to one Hf, breaking symmetry. This seems to weaken Hf-N bonding on that side of the complex. Orbital energies in eV.

the unoccupied low-lying $p\pi^*(CO)^0$ orbital with the occupied $\pi^*(NN)^4$ and $\pi(NN)^4$ (where for convenience we continue to use the labels σ and π, even though symmetry about the N-N axis has been lifted). This interaction was not possible along the N-N axis due to σ repulsion. This seems to reduce the energetic barrier on the way to the final NCO^- product. In addition, asymmetric attack by CO disrupts the symmetry of the Hf-NN-Hf unit, causing destabilization of the σ(NN) bond. Breaking of σ(NN) happens through mixing with $p\pi$(CO) and this leads to localisation of the electron pairs: σ(NN) and π(NN) onto an atomic *p* orbital of the more distant N atom, giving N^{3-}, while at the same time, an electron pair from σ(CO) can start to form a bond between CO and N. Zhang *et al.* propose [8] that N-N cleavage leads to the structure that we denote I4 with N^{3-} bridging two Hf and $[NCO]^-$ coordinated to one Hf (Figure 1). As well as I4, we have found a symmetrical structure I3 (Figure 1) that also has no N-N bond (2.73 Å) but has both anions bridging. Geometry optimization shows that this minimum is directly linked via TS2/3 to I2 as shown in Figure 11. I3 is computed to be -63 kJ/mol more stable than I4 (for L = Cp) and MD simulations at T = 500 K reveal that the two structures can interconvert. Zhang *et al.* report only a 16 kJ/mol barrier between I2 and I4 [8] and our calculated barrier for the simple L = Cp model at TS2/3 is E_a = 9.3 kJ/mol, which is much less than the barrier computed for symmetric approach of CO to R (see above). The reaction is highly exothermic; our value of ΔE(I2 → I4) = -237 kJ/mol is in reasonable agreement with Zhang's result ΔE(I2 → I4) = -260 kJ/mol.

.

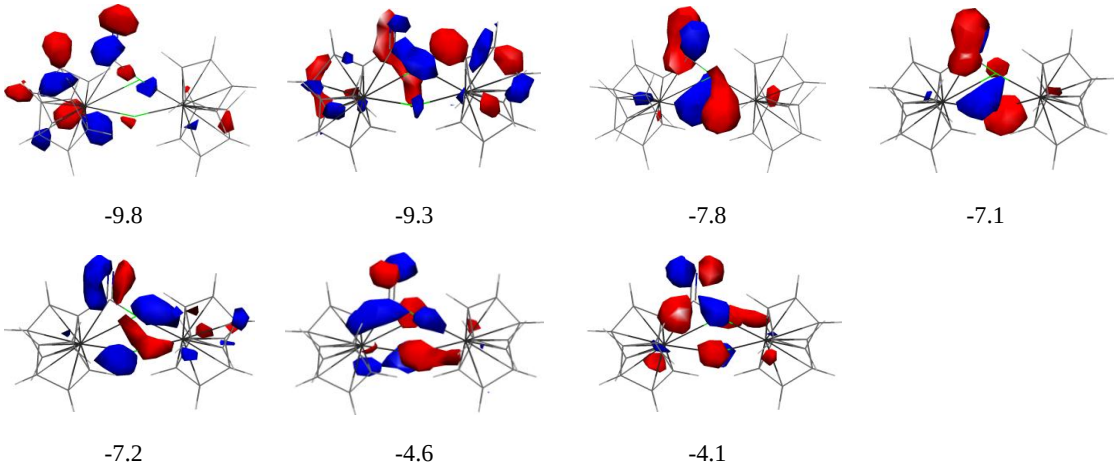


Figure 10 – CO inserts into one of the Hf-N bonds in intermediate I2. The two sets of orbitals reveal how the Hf-CO unit interacts with one N, weakening the N-N bond. Orbital energies in eV.

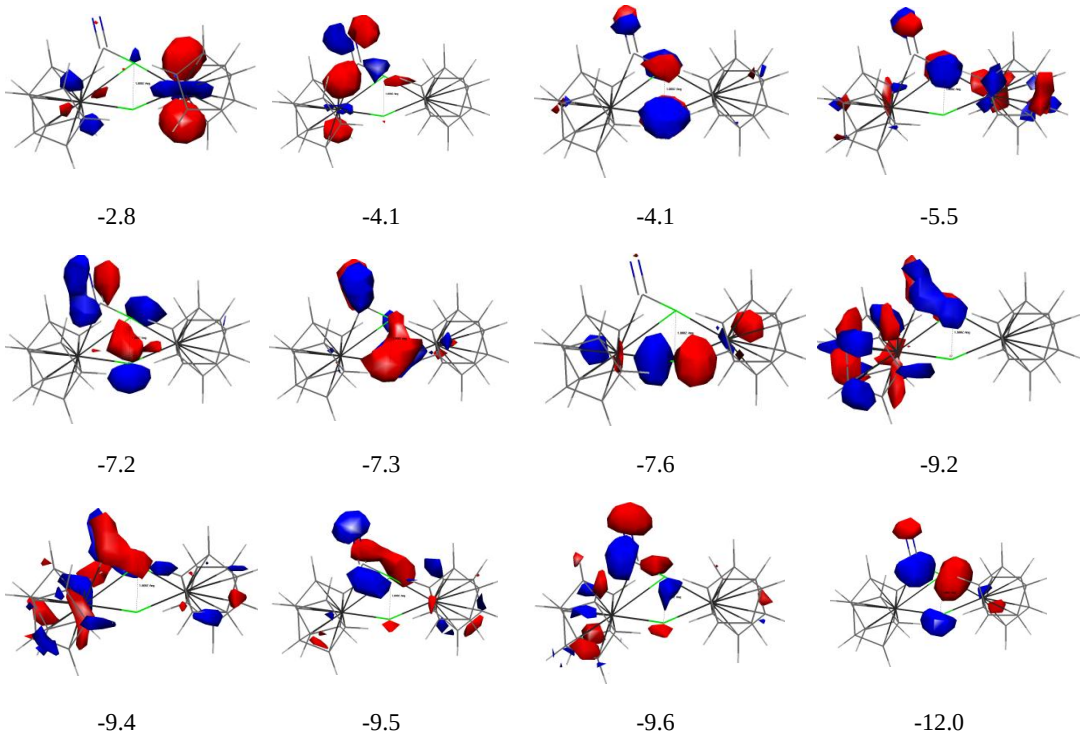


Figure 11 – Selected MOs of transition state TS2/3 linking two minima I2 and I3. We see progress in weakening of the N-N bond. Orbital energies in eV.

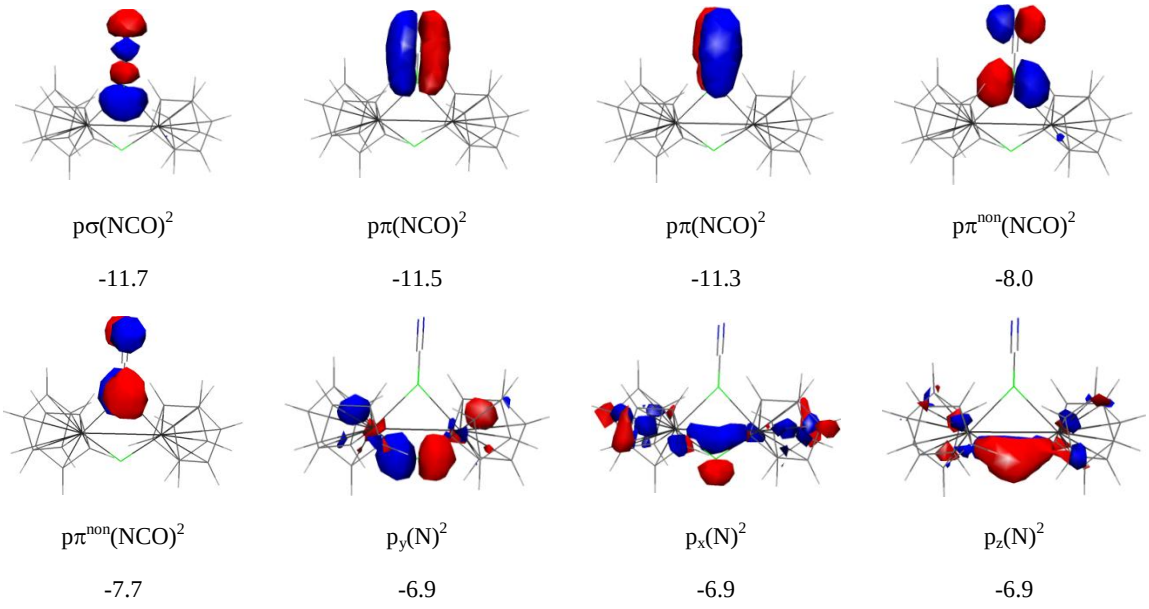


Figure 12 – Selected MOs of the product complex I3, $[Hf_2Cp_2(NCO)(N)]$. The mixing shown in I2 has allowed $p\sigma(NN)_2$ to be polarised into $p(N)_2$, yielding $[N]^{3-}$, a net gain of one electron by that N atom. Virtual orbitals not shown: $p\pi^*(NCO)$, $p\sigma^*(NCO)$. Orbital energies in eV.

Mulliken population analysis confirms the assignment of N^{3-} and $[NCO]^-$ to the anions in I3 and I4, so that the reaction may be written: $[N_2]^{4-} + CO \rightarrow N^{3-} + [NCO]^-$. The resulting molecular orbitals are shown in Figure 6 and Figure 12. As noted above, substantial energy is released in the N-N cleavage step which probably reflects the stability of the newly-formed cyanate anion. Population analysis shows no MO overlap between Hf and cyanate, so that it can bridge (I3) or coordinate to a single Hf (I4). In contrast, a substantial overlap is evident between *d*(Hf) and some of the atom-like MOs of the newly-formed N^{3-} ligand. The reaction steps that follow N-N cleavage have been discussed before [8]: N^{3-} can abstract protons intramolecularly from other ligands to give a bridging amide or can react with further CO to give a bridging oxamide.

We predict that, like CO, other neutral σ-donor and π-acceptor molecules will be able to cleave N_2 within the bis-hafnocene complex and thus become functionalized with N.

8.3.4 Effect of spectator ligands

We now investigate how the composition of the organometallic complex affects the N-N cleavage reaction. Looking first at how the reaction energies are affected by the size of the spectator ligands (L = *ansa*Cp* and L = Cp, Table 1), we see significant differences only when CO is bound to one metal center (I1). ΔE(R + CO → I1) = -18 kJ/mol for L = *ansa*Cp*, which

indicates little interaction with the complex, while for the simple L = Cp model ΔE(R + CO → I1) = –55 kJ/mol. This difference may be due to the bulk of the *ansa*Cp* ligands hindering coordination of CO to Hf. Consistent with this, I1 and I2 are roughly isoenergetic for L = Cp, but in the case of bulkier *ansa*Cp*, there is a driving force of about -30 kJ/mol towards I2, where CO is bonded to N as well as Hf. As shown above, this leads to the N-N cleavage reaction. We therefore see that bulky spectator ligands hinder bond formation with the metal cation but help direct the CO towards N.

Table 2 – Charge from Mulliken Population Analysis in units of the electronic charge for Hf and Zr dimer complexes with L = Cp. Hf1, Zr1 and N1 are the atoms in TS2/3 which are coordinated to C of CO. See Figure 1 or Figure S2 in Supporting Information for the detailed structures.

	R	TS2/3		R	TS2/3
Hf1	0.71	0.68	Zr1	0.54	0.48
Hf2	0.71	0.85	Zr2	0.54	0.70
N1	-0.44	-0.33	N1	-0.39	-0.31
N2	-0.44	-0.61	N2	-0.39	-0.55

8.3.5 Effect of the metal cation

We now consider the effect of the metal cation, where the calculations reveal small differences in reaction energies between Hf and Zr versions of the intermediate complexes (Table 1). Coordination of CO to the metal (R → I2) is less exothermic in Zr complexes than in Hf complexes, by 13 kJ/mol for L = Cp. Subsequent reaction steps including N-N cleavage are also slightly more favoured for the Hf complex, both thermodynamically and kinetically (E_a is 7 kJ/mol lower at TS2/3). It is known that Hf^{4+} and Zr^{4+} show very similar ionic size and charge distribution in their ground states and differ primarily in the energy of their valence *d* orbitals, [17] making Hf less electrophilic than Zr. At TS2/3, we observe a slight increase in the ionicity of M-N bonds and a reduction in electron density on M (Table **2**), which should cost less energy for the less electrophilic Hf cation. This is consistent with the lower computed value of E_a for the Hf complex relative to Zr. The differences are small but they still may have an influence on the reaction pathway and lead to the differences seen experimentally [18].

Since the TS2/3 barrier is quite low for both Zr and Hf, it is conceivable that a mixed complex of the sort $Cp_2Hf(N_2)ZrCp_2$ would also be active in this reaction. Such a complex would have in-built symmetry-breaking that might accelerate the N-N cleavage reaction with CO.

8.4 Conclusions

We studied the mechanism of the reaction of CO with an Hf_2N_2 complex in which the σ(NN) bond is cleaved and an N-C bond is formed, leading to the isocyanate anion (NCO^-). We have focused on orbital interactions to explain why CO must first coordinate to one metal center and insert into one Hf-N bond. This breaks the symmetry of the NN unit, and the resultant mixing of MOs allows σ(NN) to be polarized, localizing electrons on the more distant N and ultimately cleaving the N-N bond. The alternative reaction pathway, whereby CO approaches directly along the N-N axis, is found to show a high potential barrier due to repulsion between occupied orbitals on CO and NN. The repulsion is minimized when CO coordinates asymmetrically to one Hf and N. Designing asymmetric complexes or complexes with less bulky spectator ligands might therefore cause the reaction to proceed faster. Overall, the mechanism can be described as donation of σ(CO) and π(CO) to NN and back-donation of $\pi^*(Hf_2N_2)$ to CO, which leads to σ(NN) bond cleavage and NCO^- formation. We expect that an improved understanding of the cleavage pathway and the mechanism of functionalization will help design new processes for stoichiometric and catalytic nitrogen fixation.

1. Ertl, G., *Heterogeneous catalysis on the atomic scale.* The Chemical Record, 2001. **1**(1): p. 33-45.
2. Ertl, G., *Reactions at Surfaces: From Atoms to Complexity (Nobel Lecture).* Angewandte Chemie International Edition, 2008. **47**(19): p. 3524-3535.
3. Schlögl, R., *Catalytic Synthesis of Ammonia—A "Never-Ending Story"?* Angewandte Chemie International Edition, 2003. **42**(18): p. 2004-2008.
4. Mori, M., *Activation of nitrogen for organic synthesis.* Journal of Organometallic Chemistry, 2004. **689**(24): p. 4210-4227.
5. Knobloch, D.J., E. Lobkovsky, and P.J. Chirik, *Dinitrogen cleavage and functionalization by carbon monoxide promoted by a hafnium complex.* Nat Chem, 2010. **2**(1): p. 30-35.
6. Knobloch, D.J., E. Lobkovsky, and P.J. Chirik, *Carbon Monoxide-Induced Dinitrogen Cleavage with Group 4 Metallocenes: Reaction Scope and Coupling to N-H Bond Formation and CO Deoxygenation.* Journal of the American Chemical Society, 2010. **132**(30): p. 10553-10564.
7. Knobloch, D.J., E. Lobkovsky, and P.J. Chirik, *Functionalization of Hafnium Oxamidide Complexes Prepared from CO-Induced N_2 Cleavage.* Journal of the American Chemical Society, 2010. **132**(43): p. 15340-15350.
8. Zhang, X., B. Butschke, and H. Schwarz, *N_2 Activation by a Hafnium Complex: A DFT Study on CO-Assisted Dinitrogen Cleavage and Functionalization.* Chemistry – A European Journal, 2010. **16**(42): p. 12564-12569.
9. Ahlrichs, R., et al., *Electronic structure calculations on workstation computers: The program system turbomole.* Chemical Physics Letters, 1989. **162**(3): p. 165-169.
10. Sierka, M., A. Hogekamp, and R. Ahlrichs, *Fast evaluation of the Coulomb potential for electron densities using multipole accelerated resolution of identity approximation.* The Journal of Chemical Physics, 2003. **118**(20): p. 9136-9148.
11. Eichkorn, K., et al., *Auxiliary basis sets to approximate Coulomb potentials (Chem. Phys. Letters 240 (1995) 283).* Chemical Physics Letters, 1995. **242**(6): p. 652-660.
12. Eichkorn, K., et al., *Auxiliary basis sets for main row atoms and transition metals and their use to approximate Coulomb potentials.* Theoretical Chemistry Accounts: Theory, Computation, and Modeling (Theoretica Chimica Acta), 1997. **97**(1): p. 119-124.
13. Schafer, A., H. Horn, and R. Ahlrichs, *Fully optimized contracted Gaussian basis sets for atoms Li to Kr.* The Journal of Chemical Physics, 1992. **97**(4): p. 2571-2577.
14. Andrae, D., et al., *Energy-adjustedab initio pseudopotentials for the second and third row transition elements.* Theoretical Chemistry Accounts: Theory, Computation, and Modeling (Theoretica Chimica Acta), 1990. **77**(2): p. 123-141.
15. Bridgeman, A.J., *Main group monocarbonyls.* Inorganica Chimica Acta, 2001. **321**(1-2): p. 27-41.
16. Fournier, R., *Theoretical study of the monocarbonyls of first-row transition metal atoms.* The Journal of Chemical Physics, 1993. **99**(3): p. 1801-1815.
17. Zheng, W., et al., *Electronic Structure Differences in ZrO_2 vs HfO_2.* The Journal of Physical Chemistry A, 2005. **109**(50): p. 11521-11525.
18. Zydor, A. and S.D. Elliott, *Thermal Stability of Precursors for Atomic Layer Deposition of TiO_2, ZrO_2, and HfO_2: An Ab Initio Study of alpha-Hydrogen Abstraction in Bis-cyclopentadienyl Dimethyl Complexes.* The Journal of Physical Chemistry A, 2010. **114**(4): p. 1879-1886.

Chapter 9. Overall discussion and conclusions

The viability of the ALD process depends on the selection and use of suitable precursor molecules. Selecting precursors with all of the desired properties, however, has not been a straightforward process because relatively little data exist for the available precursors and ALD chemistry is not deeply understood. To understand why some precursor molecules are more successful in ALD than others, in this work an *ab initio* study was carried out of the thermochemistry that underlies precursor reactivity at surfaces and in the gas phase. The aim was to obtain insight into the reaction mechanism for heteroleptic precursors. Understanding the ALD mechanism is important because the exact reaction mechanism affects precursor stability and the growth rate and purity of the films. Additionally a mechanistic understanding can guide proper precursor selection for the experimental ALD process, which will help to save time and money in process development.

The following sections deal with the conclusions of the studies of the ALD reaction mechanism of Group 4 metallocene, the links between ALD and catalysis mechanisms via α-hydrogen abstraction, and a summary of the conclusions.

9.1 ALD Reaction Mechanism

9.1.1 Ligand elimination model

The dominant ALD reactions forming metal oxides appear to be the so-called ligand exchange reactions [1]. When water is used as the oxygen source, ligand exchange involves breaking the metal-ligand (M-L) bonds of the precursor and an O-H bond of the surface, and forming an M-O bond and a L-H bond. The strengths of the bonds that dissociate and form during the ALD reactions directly determine the thermodynamics of the reaction and, less directly, influence the rates of reaction. Precursors with strong L-H bonds and weak M-L bonds have strongly exothermic reactions, tending to make pure, thin films at low temperatures. Furthermore, unwanted side reactions will be less likely, and the process will usually be faster. However, the metal-ligand bond must be sufficiently strong for the precursor to be stable during storage and delivery.

This work therefore makes use of a simple model that describes reactivity with respect to this aspect of ALD. This model was applied to a range of heteroleptic metallocenes [$M(Cp)_{4-n}(L)_n$], M = Hf/Zr, L = Me and OMe (Chapter 3 and Chapter 4). The central mechanistic question for these heteroleptic complexes such as $Zr(CpMe)_2Me(OMe)$ was therefore in what order the ligands will be eliminated during ALD. The data revealed a clear thermodynamic preference for elimination of ligands in the following sequence: Me, followed by Cp, followed by OMe. Quadrupole Mass Spectrometry (QMS) measurements confirm this ligand release pattern [2] but another *in situ* experiment on this precursor does not show the same agreement with the calculations [3]. This second experiment instead showed that the ALD mechanism is much more complicated and it is not possible to describe the process with only a ligand elimination model. The simplified model does not include other important aspects of ALD surface reactions such as adsorption, diffusion, and desorption, as well as other mechanisms that have an influence on ALD growth. This simple model is nonetheless helpful in assessing the important precursor properties: the relative bond strength of Zr-L versus H-L. This model identified a strong affinity of Me^- for H^+, and a weaker bonding of Cp to metal (Zr and Hf) than of OMe to metal (Zr and Hf). As a result, recommendations based on this analysis may be made for improved precursor synthesis. For instance, in terms of ligand elimination alone it is better to use ligands whose Brønsted basicity (with H^+) is stronger than their Lewis basicity (with Zr^{4+}).

For future work in this topic it would be interesting to calculate the reaction of the precursor with $M(OH)_4$ instead of water to include some influence of metal on the O-H bond and consequently on the energetics of the reaction. The model could be useful to calculate the energetics of the reaction after exchange (elimination) of one, two or three ligands (Equation 1). In this way we could see the influence of OH groups on M-L bond strength.

$$ML_4 + M(OH)_4 \longrightarrow ML_3(OH) + HL \qquad \text{Equation 1}$$

9.1.2 Surface model

ALD precursors are expected to be volatile and stable in the gas-phase but reactive on the substrate and growing surface. Those requirements are difficult to achieve simultaneously and completely as the chemistry of the precursors is very complex. Some properties are

inversely related to others; improving volatility or thermal stability of a precursor, for example, can at the same time block the reactivity of the precursor with the surface. This was the case when designing a new Ti precursor. The aim was to improve the stability of the $Ti(OMe)_4$ precursor by replacing one ligand with a Cp*(i.e. C_5Me_5) ligand, which is known to confer improved thermal stability. Furthermore, as a sterically-demanding ligand, Cp^* covers vacant coordination sites in a precursor which helps increase precursor volatility. The ligand elimination model in Chapter 3 and 4 also suggests that Cp ligands are more reactive towards surface proton than alkoxide ligands are. When the ligand was replaced to give $Ti(OMe)_3Cp^*$, the stability and volatility improved as expected but the new precursor did not show any film growth in ALD with water.

We therefore launched a series of calculations to answer the question: "Why did the improved $TiCp^*(OMe)_3$ not show ALD growth while $Ti(OMe)_4$ did?" The calculations in Chapter 5 revealed that replacing one OMe ligand with a Cp* ligand causes steric crowding within the ligand sphere to such a degree that the precursor meets too high an energetic barrier on the way to coordinate to the oxygen atoms of the surface. Additionally, the use of Cp* rather than OMe ligands lowers the electrophilicity of the Ti center which in turn makes Ti less attracted to the oxygen surface. Surprisingly, if the metal center of the precursor does not coordinate directly to oxygen we find that there will be no ligand elimination. Blocking one step of the ALD reaction sequence blocks the whole growth process. In that case it is not ligand elimination which is the critical surface reaction but instead it is the formation of M-O bonds via chemisorption to the surface. The crowding is much less in monomeric $Ti(OMe)_4$ and so there is no impediment to the chemical bonding of Ti from that adsorbate to the surface.

Interestingly, other studies have shown that that ALD growth is possible with $Ti(OMe)_3Cp^*$ when O_3 was used instead of water [4]. In this case, we think that O_3 as a strong oxidiser removes the bulky Cp* ligand and that this allowed Ti-O coordination, ligand elimination reactions and consequently material growth.

In future, it would be valuable to verify the model with an experiment, such as *in situ* detection of ligands eliminated during the precursor pulse and water pulse. If possible, it would be also useful to experimentally check if precursors can stay on the surface without

being coordinated to the oxygen surface after gas purging. This may indicate the importance and strength of hydrogen bonds between a precursor and a surface.

Furthermore it would be interesting to model the surface reactions for analogue precursors $Zr(OMe)_3Cp^*$ and $Hf(OMe)_3Cp^*$ to see the influence of different ionic radii on the energetics of the reactions. It is possible that, due to larger ionic radius, Zr and Hf precursors would be able to coordinate to the surface and material growth would be possible, as seen for other cyclopentadienyl precursors of Zr and Hf [5].

9.1.3 α-hydrogen abstraction

The effect of Cp* in preventing the coordination of Ti to the surface seems to be both steric (full coordination sphere) and electronic (lower electrophilicity of Ti). It was also shown in Chapter 6 that electrophilicity has an effect on the thermal stability of metallocene complexes. Thermal stability is important because a commercially-useful precursor must be stable during storage and during evaporation/sublimation without CVD side-reactions. Bis-alkyl metallocene precursors, $ZrCp_2Me_2$, were found to be unstable. In particular, the experimental finding that $ZrCp_2Me_2$ is less stable than $HfCp_2Me_2$ is surprising because Zr and Hf elements show a similar chemistry due to their similar electronic ground state and ionic radius. The difference in stability despite similar electronic properties motivated the search for a decomposition reaction pathway that could explain why this is observed. As a result, it was found in Chapter 6 that the most likely reaction pathway was intramolecular hydrogen abstraction from one alkyl ligand to form a C-H bond on the other alkyl ligand. Electronic analysis of the computed transition state showed that during this reaction there is an electron pair transfer from the HOMO orbital to the LUMO orbital and that the transfer happens via the metal *d* orbital. In this way the $\sigma(M\text{-}C(CH_3))$ bond breaks and a two-center $\pi(M{=}C(CH_2))$ bond forms. The activation energy is observed to increase with the increasing HOMO-LUMO band gap and, specifically, with the energy of the empty *d* orbital. We know that both the HOMO-LUMO band gap and the electrophilicity increase going down the metal cations of group 4 and this sheds light on why $HfCp_2Me_2$ is more stable than $ZrCp_2Me_2$: the Zr complex has a smaller HOMO-LUMO band gap than the Hf complex and it therefore costs less energy to transfer an electron pair between those orbitals.

The influence of Cp ligands on the activation energy of this reaction was additionally studied in Chapter 6. It was found that the Cp ligands reduce the electrophilicity of the metal centre compared with the other studied "spectator" ligands, Me and OMe. In addition, the steric demand of the Cp ligands reduces the angle between the Me ligands in the molecule, encouraging the α-hydrogen abstraction reaction, since it is easier for hydrogen to be transferred to the neighboring Me ligand. Furthermore, the bulky Cp ligands prevent a bimolecular reaction and promote the unimolecular decomposition pathway, as well stabilizing the transition state (TS) and the product by covering empty coordination sites on the metal. The smallest HOMO-LUMO band gap exists for $TiCp_2Me_2$; having the smallest ionic size it also has the smallest angle between Me ligands. These characteristics make this complex the most unstable of the series of MCp_2Me_2 group 4 complexes where there is a possibility for α-hydrogen abstraction. The effect of the Cp ligands in this reaction is the same as the effect which has been described in previous studies for $TiCp^*(OMe)_3$ (Chapter 5): the electrophilicity of the metal centre is reduced. The presence, however, of the Cp ligand, due to both steric and electronic effects, make $TiCp^*(OMe)_3$ unreactive with the TiO_2 surface while, on the contrary, in the case of MCp_2Me_2 complexes the increased reactivity lies in their unimolecular decomposition pathway.

We conclude that there are advantages and disadvantages to including Cp ligands in the design of ALD precursors. Firstly, Cp ligands show the desired reactivity towards the proton of the ALD surface as has been shown in the ligand elimination model of Chapter 3. Secondly, their presence in the molecule prevents dimerization and bimolecular reactions in the gas phase, which increases volatility and stability respectively, both of which are desirable properties for ALD precursors. There are, however, cases where Cp ligands cause problems, such as promoting unimolecular decomposition pathways in the gas phase and preventing coordination of a precursor to the surface. This latter problem prevents further ligand elimination which inhibits the overall ALD growth as seen for Ti precursor.

The reverse path of an α-hydrogen abstraction reaction is a well-known carbon-hydrogen bond activation in which the C-H bond adds across a metal-ligand bond. Such bond activations are highly desirable in the context of functionalization of hydrocarbons. It was thus valuable to apply the knowledge gained in our studies of the thermal stability of $ZrCp_2Me_2$ (Chapter 5 and 6) to a catalytic system. One particular example is the catalytic

system where a C-H bond is activated within a hafnium dimer complex, specifically the reaction of $((Me_2Si,\eta^5\text{-}C_5Me_4)(\eta^5\text{-}C_5H_3\text{-}3\text{-}^tBu)Hf)_2(\mu_2,\eta^2,\eta^2\text{-}N_2)(2\text{-}N_2)$ with CO [6] where N_2 cleavage is coupled with N-C bond formation and hydrocarbon C-H bond activation. Here, C-H cleavage happens via 1,2-addition of a C-H bond of ^tBu across a multiple Hf=N bond. It was observed, interestingly, that the computation of the reaction pathway for the hafnium dimer complex (Chapter 7) yielded similar results as previously obtained in the case of $ZrCp_2Me_2$ (Chapter 6). The 1,2 addition of C-H or the reverse reaction (α-hydrogen abstraction) proceeds via a four-membered, planar cyclic TS. At the TS, it can be seen that there is mixing of HOMO-1 (π(Hf=N)) and LUMO (noting the Hf:*d* orbital character of both) so that the electron density shifts from N to $C(CH_3)$ to form a σ(Hf-$C(CH_2)$) bond in the product, just like in the case of C-H bond activation in CH_4 by $ZrCp_2CH_2$ (*i.e.* the reverse of α-hydrogen abstraction in $ZrCp_2Me_2$). From our studies on $ZrCp_2Me_2$, it can now be understood how the σ($C(CH_3)$-Zr) or σ($C(CH_2)$-Hf) bond is formed in the C-H bond activation reaction. The previous study in Chapter 6 on $ZrCp_2Me_2$, however, did not explain what happened with hydrogen, how it is transferred, and how the bond is formed between H and C or N in the product. We therefore carried out a detailed electronic analysis of the reaction in the case of the Hf dimer complex, which helped to answer those questions and to better understand the mechanism of C-H bond activation or, in reverse, α-hydrogen abstraction. The calculations revealed that during the C-H bond activation reaction, another electron pair is transferred from the C-H bond either to a new N-H bond (Hf dimer complex) or to a new C-H bond ($ZrCp_2Me_2$) in tandem with the motion of H. The best way to describe this is shown in Figure 3 in Chapter 7, shown again here as Figure 1.

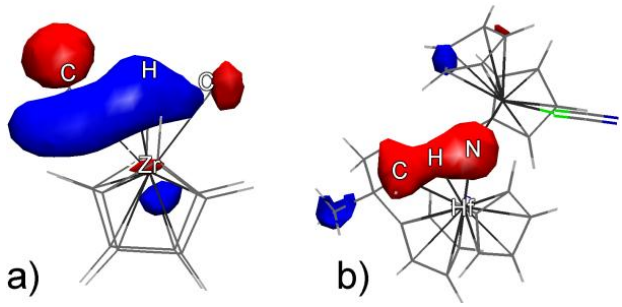


Figure 1 Isosurface plots of orbitals involved in hydrogen transfer in the computed transition state of C-H bond activation reaction in a) Zr complex and b) Hf_2N complex. See Chapter 7 for detailed atomic structures.

In Figure 1, the wavefunction lobe is seen to be spread between C, H and X, where X = C or N. Population analysis shows only a slight increase in the positive charge on H at the TS. This reveals that neutral H is transferred while σ(C-H) transforms into σ(H-X) without substantial interaction of H with M. The mechanism of C-H bond activation proposed in Chapter 7 is described as Rotational Electron Pair Exchange, where electrons originate as σ(C-H) and π(M=X) and end up as σ(H-X) and σ(M-C) respectively as shown in Figure 2. This description of the mechanism of C-H bond activation is different from that presented in the literature [7]. The difference lies in the interpretation of those results, which is what leads to the different conclusions. Hence Chapter 7 offers new insight into the mechanism of C-H bond activation which has not been previously identified. As well as increasing the understanding of the mechanism of C-H bond activation within a catalytic system, the study in Chapter 6 and 7 additionally can be used to improve knowledge of the thermal stability of ALD precursors of type MCp_2Me_2.

For future work, considering these results, other examples of σ-bond activation such as N-H, Si-H, C-C, H-H by a metal complex could be investigated. It would be interesting to see if the proposed reaction model can be applied to these and other catalytic systems.

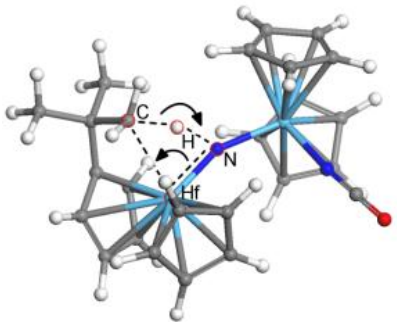


Figure 2 Computed structure of TS in the reaction pathway of C-H bond activation in model Hf_2 complexes (L_1 = $C_5H_4{}^tBu$, $L_{2\text{-}4}$ = C_5H_5). White = H, grey = C, pale blue = Hf, dark blue = N, red = O. The arrows indicate two electron pair transfers described as Rotational Electron Pair Exchange.

The reaction of the hafnium dimer complex with CO that was studied for the purpose of understanding C-H bond activation has another interesting application, namely the cleavage of an N-N bond and resulting N-C bond formation. Cleavage of the strong, triple bond in the

N_2 molecule has represented a major challenge to the development of N_2 fixation chemistry. The reaction proposed by Knobloch *et al.* [6] is a recent advance in the reductive cleavage of N_2 and functionalization to N-C at ambient temperature and pressure. This practical side of the reaction, combined with a desire to understand the mechanism, motivated further studies of this reaction in Chapter 8.

In the calculations of Zhang *et al*., [8] the N-N cleavage reaction was shown to happen via intermediates that involve coordination of CO to the metal center, even though the product of the reaction is NCO^-. Using DFT calculations, Chapter 8 investigated the reason why CO must coordinate first to the metal center and the reason why this shows a lower energetic barrier than, for example, the alternative pathway directly along the N-N axis of the metal complex. Analysis of the orbital plots of the complex where CO approaches along the N-N axis reveals repulsion between the occupied orbitals on CO and the N-N unit. This analysis helps us to see why CO has to coordinate to Hf rather than to the N-N unit directly. The repulsions along the N-N axis are minimized by instead forming an asymmetrical intermediate in which CO first coordinates to one Hf and then to N. This breaks the symmetry of the N-N unit and the resultant mixing of MOs allows σ(NN) to be polarized, localizing electrons on the more distant N. This allows σ(CO) and π(CO) donation to N and back-donation of $\pi^*(Hf_2N_2)$ to CO. As a result, the σ(NN) bond is cleaved and NCO^- is formed. The previous work [8] presented the computed energetics of this reaction pathway. Our work has added an additional degree of understanding as to why the reaction proceeds in the given way.

Comparing the effects of Cp and *ansa*Cp* in this reaction, the bulky spectator ligands of *ansa*Cp* hinder bond formation of CO with the metal cation, similarly to the way that bulky Cp* hinders coordination of the Ti precursors to the oxygen surface as shown in Chapter 5.

It would additionally be of interest to apply more accurate post-HF methods to compute the reaction pathway, as DFT is not reliable for locating transition states and computing activation energies. Furthermore, to verify the suggested mechanism, more analysis and comparison with existing or new experimental results can be done.

9.2 Conclusions

As this work illustrates, quantum chemical modeling is a powerful tool that gives insight into the reaction mechanism. Analysis of the computed systems reveals, for example, transition states, intermediates, and orbital interactions that are difficult or sometimes not possible to measure with experimental methods. Computational simulations sometimes provide a more detailed access to the world of molecules, atoms, electrons, nuclei, and their interactions. With the greater understanding gained we can predict future experimental outcomes. Simulation can be cheaper and faster than pure experimental methods, and so modelling-driven experiment can be more focused and efficient. Computational modelling is, however, ultimately a complementary process to experiment, as the accuracy of computational models can only be improved with a solid foundation based on experimental results. The combination of these two techniques can enable a much greater level of understanding into a process than either technique used alone.

In conclusion, we have seen that improved understanding of the chemistry of metal complexes can be gained from atomic-scale modelling and that this provides valuable information for the design of new chemistries. Our main focus was on new precursors for better performance in the ALD process. We found out why relatively small changes in the molecular make-up of the precursors can profoundly affect their performance. We also saw that the model decomposition pathway presented in this work can be used to analyze the utility of molecules either as ALD precursors or as catalysts for olefination reactions. As these molecules are frequently used as ALD precursors the model is therefore helpful in proposing chemical modifications to enhance thermal stability. Therefore, the ALD process window can be widened by rational molecular design based on a mechanistic understanding.

1. Widjaja, Y. and C.B. Musgrave, *Quantum chemical study of the elementary reactions in zirconium oxide atomic layer deposition.* Applied Physics Letters, 2002. **81**(2): p. 304-306.
2. Elam, J.W., et al., *Mechanism for zirconium oxide atomic layer deposition using bis(methylcyclopentadienyl)methoxymethyl zirconium.* Applied Physics Letters, 2007. **91**(25): p. 253123.
3. Niinisto, J., et al., *Novel mixed alkylamido-cyclopentadienyl precursors for ALD of ZrO_2 thin films.* Journal of Materials Chemistry, 2008. **18**(43): p. 5243-5247.
4. Rose, M., et al., *Atomic Layer Deposition of Titanium Dioxide Thin Films from $Cp^*Ti(OMe)_3$ and Ozone.* The Journal of Physical Chemistry C, 2009. **113**(52): p. 21825-21830.
5. Niinisto, J., et al., *Advanced cyclopentadienyl precursors for atomic layer deposition of ZrO2 thin films.* Journal of Materials Chemistry, 2008. **18**(28): p. 3385-3390.
6. Knobloch, D.J., E. Lobkovsky, and P.J. Chirik, *Dinitrogen cleavage and functionalization by carbon monoxide promoted by a hafnium complex.* Nat Chem, 2010. **2**(1): p. 30-35.
7. Ochi, N., et al., *Theoretical study of C-H and N-H sigma-bond activation reactions by titinium(IV)-imido complex. Good understanding based on orbital interaction and theoretical proposal for N-H sigma-bond activation of ammonia.* J Am Chem Soc, 2007. **129**(27): p. 8615-24.
8. Zhang, X., B. Butschke, and H. Schwarz, *N_2 Activation by a Hafnium Complex: A DFT Study on CO-Assisted Dinitrogen Cleavage and Functionalization.* Chemistry – A European Journal, 2010. **16**(42): p. 12564-12569.